uOttawa

L'Université canadienne
Canada's university

FACULTÉ DES ÉTUDES SUPÉRIEURES ET POSTOCTORALES

uOttawa

L'Université canadienne
Canada's university

FACULTY OF GRADUATE AND POSDOCTORAL STUDIES

E'qab Almajali
AUTEUR DE LA THÈSE / AUTHOR OF THESIS

M.A.Sc. (Electrical Engineering)
GRADE / DEGREE

School of Information Technology and Engineering
FACULTÉ, ÉCOLE, DÉPARTEMENT / FACULTY, SCHOOL, DEPARTMENT

Contributions to the Design of Sub-Reflectarrays
TITRE DE LA THÈSE / TITLE OF THESIS

Derek McNamara
DIRECTEUR (DIRECTRICE) DE LA THÈSE / THESIS SUPERVISOR

CO-DIRECTEUR (CO-DIRECTRICE) DE LA THÈSE / THESIS CO-SUPERVISOR

M. Yagoub

Jafar Shaker

Henry Schriemer

Gary W. Slater
Le Doyen de la Faculté des études supérieures et postdoctorales / Dean of the Faculty of Graduate and Postdoctoral Studies

Contributions to the Design of Sub-Reflectarrays

by

E'qab Almajali, B. A. Sc.

A thesis submitted to the
Faculty of Graduate and Postdoctoral Studies
as a partial fulfillment of the requirements for the degree of

Master of Applied Science
in Electrical and Computer Engineering

Ottawa-Carleton Institute for Electrical and Computer Engineering
School of Information Technology and Engineering
Faculty of Engineering
University of Ottawa

December 18th, 2009

Your file Votre référence
ISBN: 978-0-494-65480-4
Our file Notre référence
ISBN: 978-0-494-65480-4

Abstract

In this thesis we show how the ellipsoidal and hyperboloidal subreflectors, which are used in dual reflector antenna systems, can be emulated by reflectarrays (hereafter referred to as sub-reflectarrays). To achieve this we derive the basic design equations required to provide the proper phase correction at each element of the sub-reflectarray to end up with radiated amplitude and phase patterns that are indeed close to those of the emulated ellipsoidal or hyperboloidal subreflectors. To calculate and analyze the radiation patterns of sub-reflectarrays, which are designed based upon the above basic design equations; two analysis methods have been developed. One based on an array analysis approach which gives an approximate (yet reliable) analysis of sub-reflectarrays, with details that do not appear to have been given elsewhere. The second method is a two-dimensional (2D) full wave computational electromagnetic analysis that uses the method of moments (MoM) to solve a 2D integral equation formulation for a 2D reflectarray. It is a very rigorous method that accounts for many effects which are computationally very difficult to be include in any three-dimensional (3D) analysis methods that could be used for same purpose, like the finite ground plane effect and feed blockage effect. Both analysis methods have been validated by using them to calculate the radiation pattern of a parabolic-type reflectarray , which are frequently reported and very well known. Simulations are performed using the two analysis methods on examples of the ellipsoidal and hyperboloidal subreflectarrays described, showing the far field amplitude and phase patterns, in so doing validating the design equations and analyzing the radiation characteristics of the sub-reflectarrays. The 2D MoM analysis enables us in this thesis to study the effect of amplitude tapering upon the radiation characteristics of sub-reflectarrays. Moreover it is used to determine the location of the virtual focal point as a function of feed position and frequency, which enables us to perform a detailed study of the power focusing characteristics of an ellipsoidal sub-reflectarary. Lastly, a practical experimental validation has been done by implementing some sub-reflectarrys and measuring their radiation patterns' amplitude and phase.

Acknowledgements

First I would like to express my deep thanks and gratitude to my thesis supervisor, Dr. Derek McNamara, whose guidance, patience and support were very invaluable from day one of my masters degree work. For me, he is not only the supervisor but is also an example I wish to follow.

I would also like to thank the entire antenna research group at the Communication Research Center (CRC), especially Dr. Jafar Shaker and Dr. Reza Charharmir for always being available to give many helpful suggestions and to help with technical problems, their expertise was greatly appreciated. Many thanks to Mr.David Lee for his help with the hardware and measurement setup relating to this work. I thank the CRC antenna group manager, Mr. Michal Cuhaci , for making this collaboration possible and funding all the hardware used for this work.

The discussion with, and help in some coding problems from, my research colleague Jonathan Ethier are highly appreciated. He is always supportive, even when he is very busy.

Many thanks go to my beloved wife and my dear parents, who have always encouraged me to pursue my education and to never settle without doing something fruitful. Finally, and most importantly, I would like to magnify and praise God, the Almighty, who enabled me to finish this work successfully.

Contents

Chapter 1

INTRODUCTION

1.1 The Reflectarray Concept

In many antenna applications it is desired to achieve a directive antenna pattern such that the energy radiated or received by the antenna is concentrated in a specified angular region. Two of the most common techniques that have been employed to achieve this are reflectors and arrays. The reflector utilizes a primary feed to illuminate a reflecting surface. The energy from the primary feed is collimated by the reflector surface to form an antenna pattern with the desired side lobe level. In contrast the array utilizes discrete elements to form the desired antenna pattern. A feed network distributes the energy to each of the discrete elements to form the desired antenna pattern.

A reflectarray combines the features of both a reflector and an array. It utilizes a primary feed to illuminate an array of discrete elements which then receive and reradiate the incident feed energy. The discrete elements of the reflectarray are designed in such a way as to correct the phase of the incident wave, be it in transmit-mode or in the receive-mode, as is done by the traditional solid surface reflector.

The concept of a reflectarray antenna was initially reported in1963 [1]. The elements of that reflectarray were terminated waveguides of different lengths. By changing these lengths the correct phase transformation could be achieved to emulate the operation of a traditional parabolic reflector. This type of reflectarray was very cumbersome and the technology was apparently not pursued. However, with the rapid development of microstrip technology in the early 80's, and the need for high gain, low cost antennas, the microstrip reflectarray was conceived [2]. The microstrip reflectarray is made up of an array of microstrip patches on a grounded dielectric substrate, each element of the reflectarray being designed in such a way as to provide the proper phase correction upon reflection to achieve the same wave transformation as in traditional reflectors.

Until early 2007, all the research that had been done on reflectarrays involved those that emulate a parabolic reflector. More recently, several authors have described the replacement of sub-reflectors [3,4,5,6], or both reflectors [7], in dual-reflector antennas by reflectarrays. However, sub-reflectarray design equations analogous to the one used in parabolic-type reflectarray design have not been given, and sub-reflectarray performance not examined in detail. These shortcomings are dealt with this thesis. We will refer to all reflectararys we design as sub-reflectarrays since they emulate the subreflector of a dual reflector antennas rather than the main reflector. Moreover we will use the mictristrip patches as the element type for all sub-reflectarrays.

1.2 Overview of Thesis

It is necessary to understand most aspects of reflectarray and sub-reflectarray antennas through comprehensive review of the most important contributions that have been reported in literature thus far. This is the main subject of Chapter 2, which includes details of the calculation of sub-reflectarray radiation patterns using array theory. In Section 2.2 we discuss a general design procedure for reflectararys, with emphasis on the phasing and bandwidth characteristics of reflectarrays. A brief discussion of existing reflectarray analysis techniques is also presented in this section to show the novelty and importance of the 2D full wave MoM reflectarray analysis method we will develop in Chapter 3. In Section 2.3 we review the most recent reflectarray developments that have been reported. In Section 2.4 we review the design methodologies used for sub-reflectarray work reported thus far in literature; this will later facilitate appreciation of the fact that the sub-reflectarray design equations we derive in this thesis are new and not reported elsewhere. Lastly, in Section 2.5 we detail the calculation of the sub-reflectarray radiation patterns using array theory. Although not new, some refinements are provided, and the details do not appear to have been given elsewhere.

Chapters 3, 4 and 5 contain the principal contributions of the present work to the subject of sub-reflectarray antennas.

Throughout Chapter 3 two of the contributions of this thesis are presented. In Section 3.2 we derive the phase equations (also called the basic design equations) required to design sub-reflectarrays. Both the ellipsoidal and the hyperboloidal phase equations are derived, with a detailed discussion of all derivation steps. In Section 3.3 we present a complete two-dimensional (2D) TE_z moment method integral equation formulation, consisting of a magnetic line source that illuminates a structure consisting of conducting strips, dielectric material and conducting ground plane. In this way it is possible to model a 2D sub-reflectarray's feed-horn, the 2D sub-reflectarray proper, and its interaction with the feedhorn. Since this formulation is rigorous it accounts for many effects which are difficult to be included in any approximate 3D analysis methods that might be used for same purpose. It is effectively used to validate the derived design equations and to do some parametric studies as well.

Chapter 4 can be called the validation chapter. We validate the array analysis method and the 2D MoM integral equation formulations, as well as the derived phase equations. In Section 4.3 we validate the codes we developed based upon the above mentioned analysis methods through using them to calculate the radiation pattern of a parabolic type reflectarray . The scattered fields from ellipsoidal and hyperboloidal subreflectors are discussed in Section 4.4 to form a foundation that we will use to understand scattering from sub-reflectarrays. In Section 4.5 we discuss a special type of validation for the derived phase equations that is done by comparing the radiation patterns of sub-reflectarrays with their equivalent solid subreflectors. In Section 4.6 we consider the theoretical validation of the derived phase equations using both array analysis and 2D MoM codes. Both amplitude and phase patterns are presented using different horn-feeds illuminating the sub-reflectarrays to show the impact of changing edge taper upon the radiation characteristics. The study of sub-reflectarray amplitude and phase radiation patterns is another contribution of this thesis which has not been reported elsewhere in literature to date. Sub-reflectarray virtual focal point position determination is the subject of Section 4.7. We present two methods to determine the position of sub-reflectarray virtual focal points. Finally in Section 4.8 we consider the power focusing characteristics of an ellipsoidal sub-reflectarray , based upon the behavior of the virtual focal point as a

function of feed position and as function of frequency. A comparison with the power focusing characteristics of the equivalent ellipsoidal subreflector is also discussed as well in this section. Although not the major contribution of this thesis, a study of these focusing characteristics is not available elsewhere.

The theoretical validation of the phase equations we have derived is supported in Chapter 5 by appealing to experiments. In Section 5.2 we consider the experimental validation of the ellipsoidal phase design equation whereas in Section 5.3 we consider the experimental validation of the hyperboloidal phase design equation. In this chapter we also discuses the effect of feed pattern amplitude taper upon the measured amplitude and phase pattern for both types of sub-reflectarrays.

Finally, some general conclusions are reached in Chapter 6, and the research reported herein put into perspective.

1.3 References for Chapter 1

[1] D.G. Berry, RG. Malech and W.A. Kennedy, "The reflectarray antenna", *IEEE Transactions on Antennas and Propagation*, Vol.11, No.6, pp.645-651, November 1963.

[2] R.E. Munson, H. Haddad and J. Hanlen, "Microstrip reflectarray antenna for satellite communication and RCS enhancement or reduction", *U.S. Patent* 4 684 952, August 1987.

[3] X.Shenheng, H.Rajagopalan, Y.Rahmat-Samii and W.A.Imbriale, "A novel reflector surface distortion compensating technique using a sub-reflectarray", *IEEE International Symposium on Antenna and Propagation,* pp.5315-5318, June 2007.

[4] M.Arrebola, L. de Haro, J.A.Encinar & L.F. de la Fuente, "Contoured-beam gregorian antenna with a reflectarray as subreflector", *Proc. 2nd European Conf. Antennas Propagat. (EuCAP'2007)*, pp.1-6, Nov.2007.

[5] X.Shenheng and Y.Rahmat-Samii, "Sub-reflectarrays for spherical aberration compensation: concept and simulations", *IEEE International Symposium on Antenna and Propagation*, pp.1-4, July 2008.

[6] M. Arrebola, W. Hu, J.A.Encinar, R. Cahill, R. Dickie, V. Fusco, H. Gamble, Y. Álvarez and F. Las-Heras, "Experimental validation of a 94 GHz dual reflector antenna with a sub-reflectarray", *Proc. 30th ESA Antenna Workshop*, May 2009, Netherlands.

[7] C.Tienda, M.Arrebola, J.A.Encinar, G.Toso & C.Mangenot, "Analysis of a dual-reflectarray antenna", *Proc. 30th ESA Antenna Workshop*, May 2009, Netherlands.

Chapter 2

A REVIEW OF MICROSTRIP REFLECTARRAYS AND SUB-REFLECTARRAYS

2.1 Introduction

In this chapter we will discuss most aspects of reflectarray antennas through a comprehensive review of the most important contributions that have been reported during the last 15 years. We will start from the basic concepts, pass through detailed design procedures, analysis techniques, recent developments, and lastly end up with a definition and review of a newly reported significant development (which will be the main subject of this thesis), namely the microstrip sub-reflectarrays. Calculation of sub-reflectarray radiation patterns using array theory will presented at the end of this chapter as well. In Section 2.2 the reflectarray concept will be presented in detail and a general design procedure presented with an explanation of the phasing and bandwidth characteristics of reflectarrays. A brief account of existing reflectarray analysis techniques will also be presented in this section to show the novelty and importance of the two-dimensional full wave reflectarray analysis method we will develop in Chapter 3. In Section 2.3 we will review the most recent developments that have been reported with some emphasis on those which have potential advantages and promising applications like the beam scaning, beam shaping and element reconfigurability. In Section 2.4 the sub-reflectarray concept will be introduced, its advantages over the electrically large reflectarrays will be mentioned, and a discussion given of its recent and future applications. All design equations and methodologies used to design sub-reflectarrays reported thus far in literature will be discussed to show that the sub-reflectarray design equations we will derive in this thesis are new, having not been reported elsewhere yet. Lastly, in Section 2.5 we will detail the calculation of sub-reflectarray radiation patterns using array theory. Although not new, some refinements are provided, as well as details do not appear to have been given elsewhere.

2.2 Reflectarrays

2.2.1 Preliminary Remarks

A reflectarray is basically either a flat or slightly curved reflecting surface that is formed by an array of reflecting elements which are printed on grounded dielectric substrate(s) with a feed antenna that spatially illuminates these elements. The elements are predesigned to radiate and scatter the incident field with a certain electrical phase. It represents a combination of a reflector antenna and a planar phased array antenna that uses a suitable phasing scheme of its elements to convert the incident wavefront to another wavefront with a prescribed phase. The elements are designed in such a way to correct the phase of the incident wave, either in the transmit-mode or in the receive mode, as is done in the traditional curved reflectors. The Element phases can be fixed to produce a fixed beam, or tunable in order to scan or reconfigure a beam. The most common feed type used to illuminate reflectarrays antenna is the feed-horn, either pyramidal or conical (e.g. corrugated) horns, although other less conventional feed types have been reported in the literature [1]. A cross-section of a single layer reflectarray with feed-horn is shown in Figure 2.1.

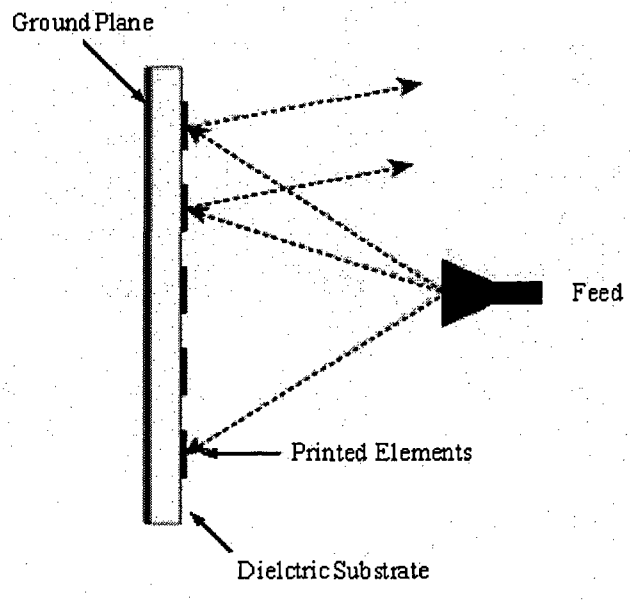

Figure 2.1-Side view of Single Layer Reflectarray Configuration

In addition to single layer reflectarrays, multilayer reflectarrays are another possible configuration where the reflectarray consists of two or more dielectric substrates as shown in Figure 2.2. The main purpose of complicating the reflectarray structure to be multilayered is to improve the bandwidth characteristics, achieved in 1995 by Huang [2], with more detailed studies on two and three-layer reflectarrays given by Encinar [3, 4]. In spite of the big advantages of multilayer reflectarrays, the majority of reflectarray antennas described in the literature have been single-layer due to ease of fabrication and hence their reasonable cost.

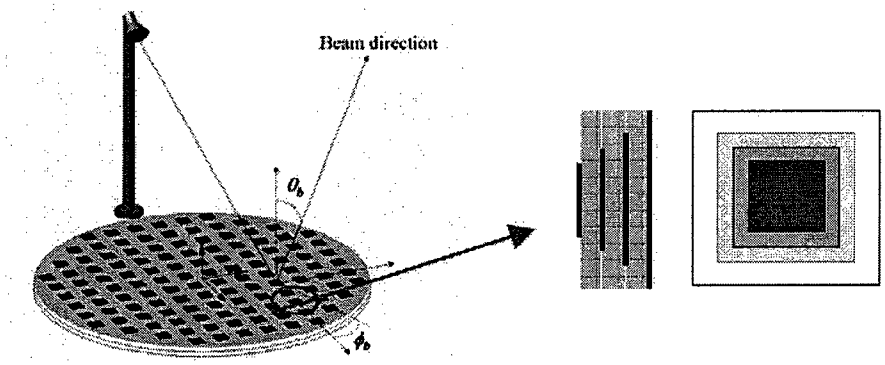

Figure 2.2- Multi-Layer Reflectarray Configuration. (After [13])

As with conventional curved reflector antennas, it is possible with proper design to the reflectarrays with offset feeds to eliminate the blockage effects [5, 6]. Reference [7] shows that the aperture efficiency can be improved slightly using the offset feed configuration. Although the usage of offset configurations is desirable due to the mentioned reasons, the on-axis configuration is still frequently used especially in the dual reflector antenna systems, for some reasons which will be discussed in Section 2.2.2.

There are several advantages of a reflectarray over an array or a conventional reflector. Firstly, unlike the array, there is no complex feeding network which introduces a high loss, unwanted phase shifts of the transmitted or received signal as frequency changes, and spurious radiation.

A reflectarray can exhibit higher efficiency. Secondly, reflectarrays are easier to manufacture than the classical curved reflectors. Offset reflectors are difficult to manufacture in many cases due to the particular surface shape, especially at higher microwave frequencies. Thirdly, for the most part, the reflectarray can be conformed to a given surface shape, reducing the bulk and mechanical complexity of the traditional reflector antennas; this advantage is of importance for new space applications because the large surface of reflectarray can be folded or rolled as part of the spacecraft payload before being deployed. Fourthly, beam scanning and beam shaping are easier and more efficient when performed using reflectarrays than conventional phased arrays. Since the element phase needs not to be quantized. Linear, dual, or circular polarization can be obtained, an advantage that will be discussed later. It is worth mentioning that the main disadvantage of a reflectarray antenna is its inherent narrow bandwidth which generally cannot much exceed 10% depending on the element design, aperture size, focal length, and so on.

2.2.2 Single-Layer Reflectarray Design

The design procedure of a single-layer microstrip reflectarray was described by Pozar in [9] and detailed by Arpin in [10]. In both references the radiating elements were variable size rectangular patches. In this thesis we will use this element type. The following steps outline the design procedure.

1- Design Parameter Selection

There are several design parameters that must be selected in the design of a reflectarray, and these depend on the frequency, bandwidth, polarization, loss and cost. The first of these parameters is the aperture shape and size. The aperture shape could be rectangular, circular, elliptical or any shape that suits the given application. In this thesis the shape of the prototype is always square with dimension D as shown in Figure 2.3. The main factor that governs the size is the type of the classical curved reflector that we want to emulate using the reflectarray. If the reflectarray emulates a parabolic reflector, the size depends mainly on the required gain and bandwidth. If the reflectarray emulates the

subreflector of a dual reflector antenna system it is called a sub-reflectarray. A subreflector does not have a fixed value of eccentricity as parabolic main reflector. The size of the sub-reflectarray depends on the eccentricity value of the subreflector it replaces and the focal length to size ratio (*F/D)* of the parabolic main reflector. The eccentricity and *F/D* control the angular range of interest over which we want the radiation power pattern to illuminate the main parabolic reflector. In the latter case we don't aim to get a pencil beam of power directed to a specific direction in space, but aim to illuminate the parent parabolic reflector or its equivalent reflectarray with a power pattern that is just wide enough to illuminate the whole surface of the main reflector efficiently. This tells us that we have more degrees of freedom when we select the size of the sub-reflectarray compared to that of a reflectarray (parabolic-type). More details about the eccentricity, *F/D* and the angular range of interest will be given in Chapter 4.

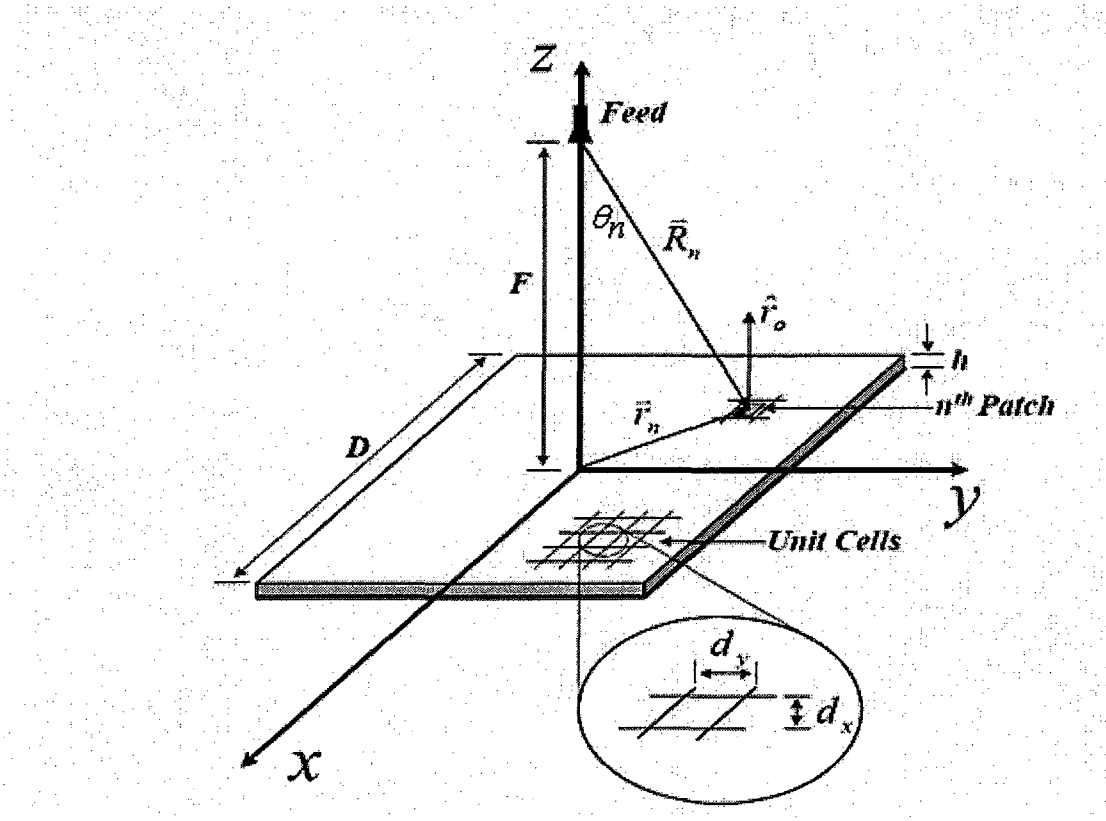

Figure 2.3- Reflectarray Design Parameters. (After [9])

The second parameter to be selected is the size of the unit cell d_x and d_y shown in Figure 2.3. The size of the unit cell determines the inter-element spacing and this spacing must be small enough to avoid grating lobes. The spacing is governed by the conventional array equation

$$\frac{d}{\lambda} \leq \frac{1}{1+\sin\theta} \tag{2-1}$$

where d is element spacing (the distance between the centers of adjacent unit cells), and θ is the main beam angle relative to the broadside direction or the incident angle from the feed at the outer most element. Based on (2-1), near broadside the element spacing could be relatively large (e.g. >0.9 λ_0) whereas for elements located toward the edge, the element spacing needs to be smaller since the wave's incident angles from the feed horn are large. Since it is practically difficult and pricy to design multi-spacing schemes, we use the smaller spacing between all elements in the reflectarray which represents the threshold to prevent grating lobes [11]. However if we want to enhance the bandwidth and minimize the phase error, the multi-spacing scheme would a good choice.

The third design parameter to consider is the feed location. The reflectarray could be center-fed or offset-fed. Each configuration has its pros and cons. Thus the designer should decide on this based on the required bandwidth and the impact of the feed blockage. For example, based on equation (2-1), it is evident that for a given reflectarray size the incident angle would be much larger if we shift the feed from its prime-focus location shown in Figure 2.3 to any position that decreases or eliminates its blockage effect. This shift then leads to bandwidth degradation since spatial path difference bcomes severe in this case as will be explained in detail later in this section. One must also select the height of the feed over the reflectarray, given by *F*. The spillover and taper efficiencies will be governed by the selection of the feed location. Typically the feed location is selected to have an edge taper of -10dB illumination, due to the feed pattern, at the edges of the reflectarray (parabolic-type) [9, 10] and about -18dB at the edge of the sub-reflectarray (ellipsoidal or hyperboloidal-type) [12, 13].

The fourth point in the selection process is to choose the shape of the radiating elements that form the reflectarray. This depends mainly on the required bandwidth and polarization, as well as the ease of fabrication and analysis. As shown in Figure 2.4, there are several shapes one can choose to achieve the required electrical phase conversion. One is to use variable-size patches, dipleos, rings or loops [14-18] so that the elements can have different scattering impedances and thus different phases to compensate for the different feed-path delay. Another is to use identical microstrip patches to which a variable length phase delay lines attached [19] so that they can compensate for the phase delays over the different paths from the illuminating feed. In a third approach, for circular polarization only, the reflectarray has all identical circularly polarized elements but with different angular rotations [20] to compensate for the feed path-length differences.

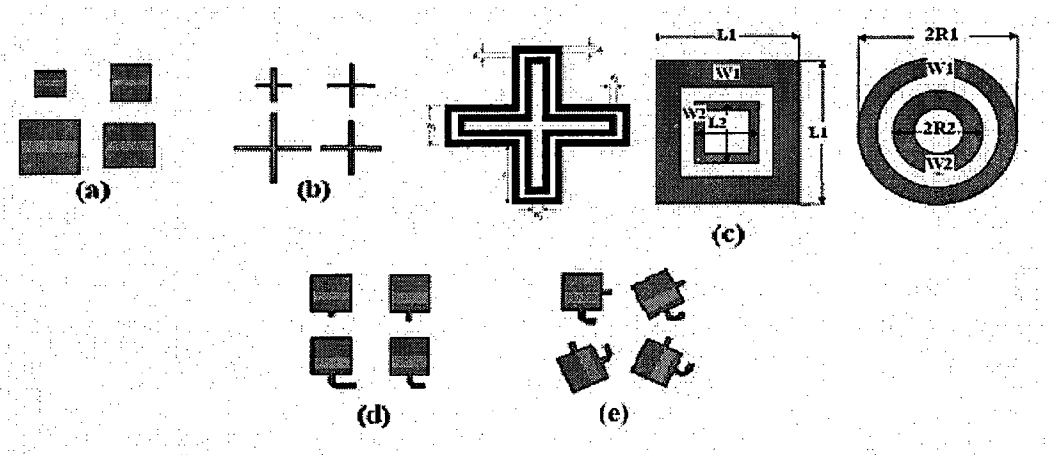

Figure 2.4- Various reflectarray elements, (a) variable-size patches, (b) variable-size cross dipoles, (c) variable-size double cross loops, double square rings and double circular rings, (d) identical patches with variable lengths phase delay lines, (e) variable angular rotation. (Adapted after [13, 18, 26]).

The type of radiating element we selected in this thesis is the variable-size rectangular patch with linear polarization. Using elements of variable size allows more freedom in laying out an array with better bandwidth and simpler analysis, as well as having the capability to use dual or circular polarizations. It is worth mentioning that the design procedure for reflectarrays with any other variable-size element shape matches that for variable size patch except as far as the radiation pattern calculation is concerned since each element shape has its own radiating characteristics and then its own pattern.

Finally one must select a substrate and its thickness. The selection of the substrate has an impact upon the bandwidth of the reflectarray and the manufacturing etching tolerance of the radiating elements, since it affects the slope of the reflected phase versus element size design curves and affects the range of the reflected phase change which will be discussed next. The cost plays an important rule in the substrate selection as well.

2-Design Database Generation and Patch Size Selection

The critical feature of the reflectarray implementation is how the individual elements are pre-designed to scatter the incident field with a required phase. As an example in a reflectarray that emulates a parabolic reflector the individual elements of the array are designed to scatter the incident field with the proper phase to form a planar uniform phase surface in front of the aperture. To get the required sizes of patches that reflect the prescribed phase, one should start by generating a set of data for the phase of the reflected field of a uniform infinite array of identical patches versus patch size. This infinite array approach [9-11], which assumes all surrounding elements are identical, only approximates the final situation where the elements are not all identical, but has been shown to be satisfactory. It at least approximately accounts for the mutual coupling effects due to surrounding elements. In this thesis the full wave analysis has been done using two commercial codes namely HFSS and EmPicasso [21, 22]. EmPicasso is a moment method code. HFSS is based on the finite element technique, and simulates the infinite array approach by using appropriate periodic boundary conditions (a mathematical waveguide simulator). Its reliability has been proved practically in [23] through comparing mathematical waveguide simulator results with the results of an equivalent real waveguide simulator using the same patch dimensions. Figure 2.5 shows an example of the phase of the reflected field versus patch size obtained using HFSS. It is known as the "S curve" (even though it does not always look like letter S). It should be noted (with reference to Figure 2.3) that if the E-field is x-directed then the dimension of the patch along the y-axis (width) is selected and remains fixed and the dimension of the patch along the x-axis (length) is varied, and vice versa depending upon the feed polarization.

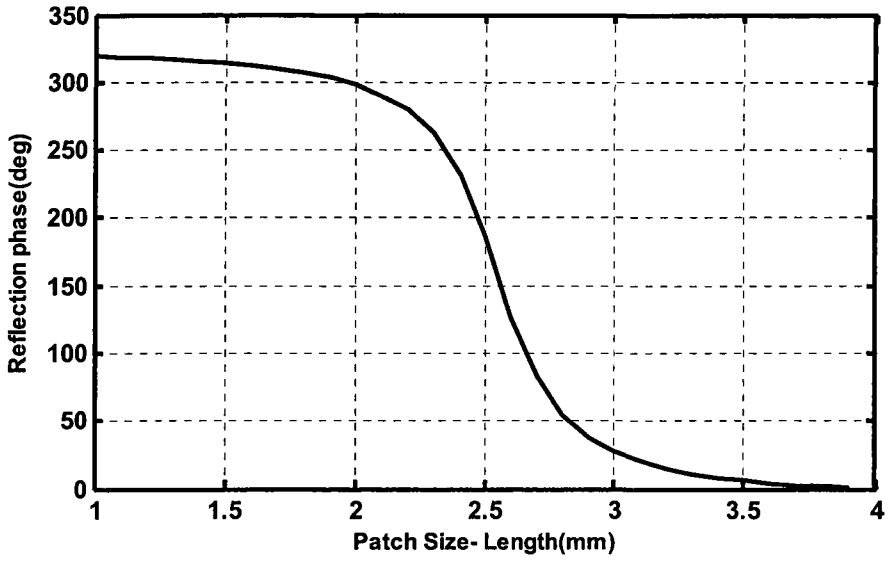

Figure 2.5-Reflected phase versus element length from an infinite array of identical patch size using HFSS, frequency=30GHz, patch width=3mm, E-plane=H-plane spacing=5mm, substrate is Rogers 30030 with thickness=0.508mm, incidence angle is 0^{o}.

Once the desired reflection phases are known, the patch dimensions can be calculated to satisfy any phase correction ψ_n required, as will be discussed in Chapter 3. This is done using interpolation of points on the curves in Figures 2.5 and 2.6. In light of the phase curve generation and design parameter selection, it is very important to talk about the phasing and bandwidth characteristics of reflectarrays. We will talk generally, but with more emphasis on single-layer reflectarrays with variable-size patch as a radiating element.

A-Phasing Characteristics of Reflectarray

In Figure 2.5 varying the size of the patches can be viewed as technique for introducing a small shift in the resonant frequency of the element, which has the effect of changing the phase of the reflected field at off-resonance frequencies, as discussed in further detail in [24]. An array of metallic patches behaves as a resonant circuit, in which the phase of the reflected wave varies when the frequency changes. In figure 2.5 the

resonance occurs when the reflection phase is 180^{o}, which at 30GHz is far a length of 2.5mm. For element lengths much shorter than this, the reflection phase approaches 320^{o}, while for element lengths greater than this the reflection phase approaches a minimum value of approximate $2k_{0}d$, where k is the propagation constant of a plane wave in the substrate and d is the substrate thickness. Therefore, if it is possible to choose an element length to achieve almost a full 320^{o} range of reflection phases, elements requiring unattainable phases due to lengths either too long or too short were not included in the array layout [25].

Due to the narrow bandwidth behavior of microstrip patches, the reflection phase versus length in Figure 2.5 shows a high slope near resonance and a very slow variation near the edges. As such the reflectarray is very sensitive to etching tolerances, and the phase distribution on the surface of the reflectarray changes with frequency, which in turn limits the overall bandwidth. In Figure 2.5 the phase slope is about 130^{o}/mm, which means a tolerance error in patch dimension of 0.1mm will produce an error in phase of 13^{o}. Thus careful attention should be paid during the etching process of single-layer reflectarrays. . A smoother phase variation, and consequently broader band behavior can be obtained by increasing the width of the patch, the thickness of the dielectric substrate or by other ways that will be discussed in part B of this section. If the thickness of the dielectric substrate is increased the total phase range is reduced to less than 300^{o}, and then no practical designs can be achieved since the full range of phase values is required to get patches lengths that satisfy the phasing condition of interest. For a substrate thickness smaller than $\lambda_{o}/\sqrt{\varepsilon_{r}}10$ [3], a range larger than 300^{o} can be obtained, which allows practical designs. The impact, of a change in the patch width upon the slope of the S curve can be noticed from Figure 2.6. It is evident that as the width of the patch increases the slope of the S curve decreases and then the bandwidth characteristics are enhanced with more freedom in etching tolerance. The curve with the most gradual slope is the most desirable, in order to have more refinement when selecting the patch sizes and in order to enhance the bandwidth of the reflectarray as well.

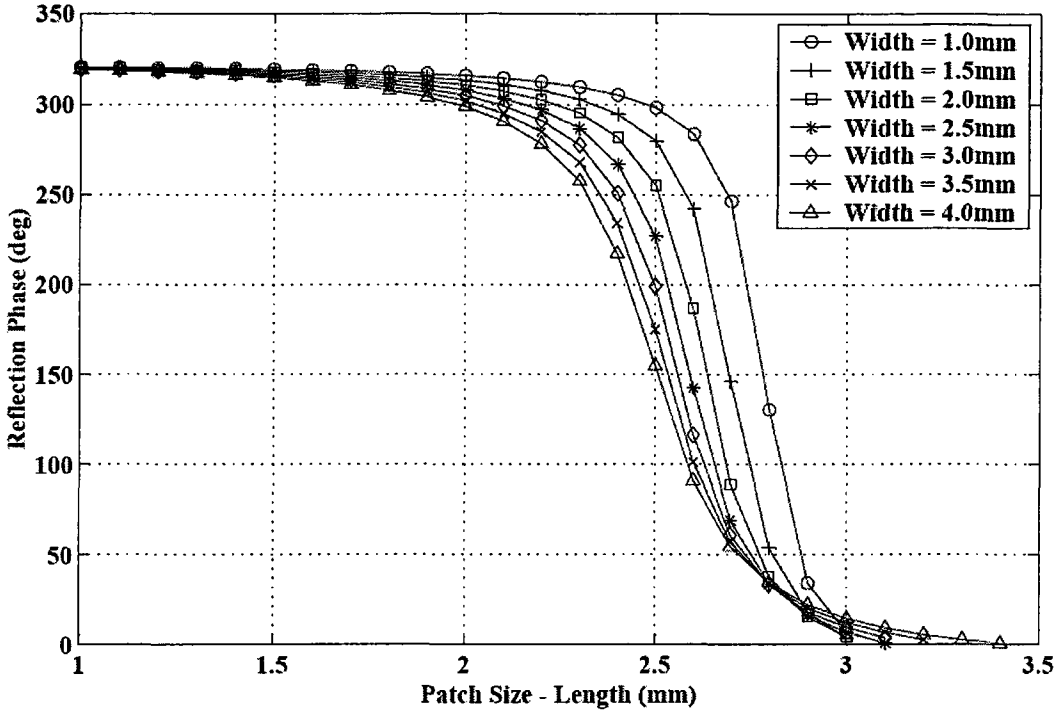

Figure 2.6-Reflected phase versus element length from an infinite array of identical patch size at different widths using EmPicasso. The inter-element spacing is 5mm along both axes.

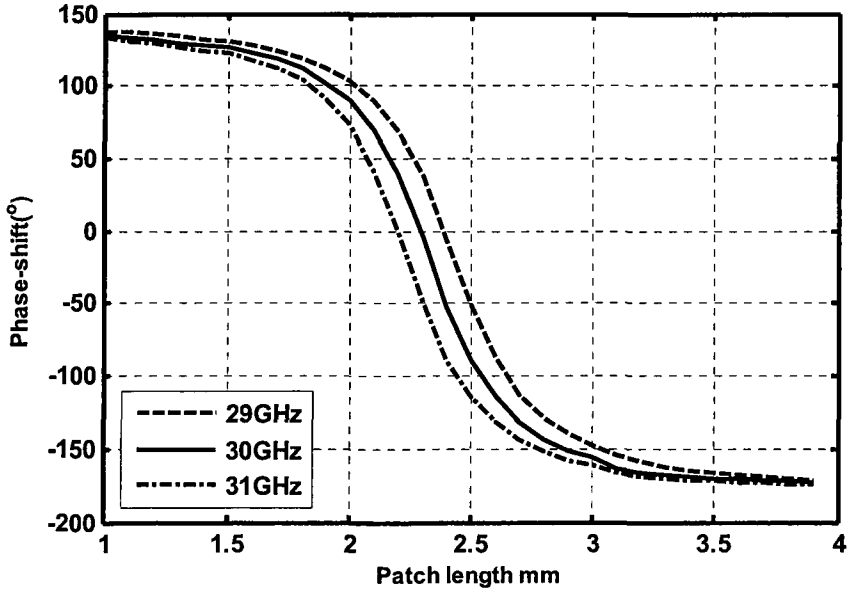

Figure 2.7- Phase shift at normal incidence for a periodic array of infinitely long strips on a grounded substrate versus the patch width at three frequencies, frequency=30GHz, E-plane spacing=5mm, substrate is Rogers 30030 with thickness=0.508mm

The reflection phase is most sensitive to frequency variations near resonance and less so near the edges of the S-shaped curve. Consequently the phase distribution on a reflectarray with patches of different sizes will change with frequency and the radiation patterns will be distorted, limiting the operational frequency band of the reflectarray. Figure 2.7 shows the phase curves for an array of infinitely long conducting patches at three frequencies. This data will be used in the 2D analysis in chapter 4 but is given here illustrate the fact that the reflection phase is frequency dependent.

B- Bandwidth Characteristics of Reflectarrays

The bandwidth performance of reflectarray using mictrostrip patch elements is limited mainly by two factors. One is the inherently narrow bandwidth of the microstrip patch element and the other is the differential spatial phase delay. The microstrip patch element has generally a bandwidth of 3-5%. To increase the inherent narrow bandwidth, techniques such as using a wide patch, thick substrate, stacking of multiple patches, using more elaborate broadband radiating elements, and using artificial impedance surfaces have been employed. Bandwidths of than 16% for microstrip patch reflectarrays have been reported. The slope of the phase versus length curve is a measure of the bandwidth of the reflectarray, as the curve with smaller slope leads to less phase error when the electrical size of the elements changes with frequency. Figure 2.6 shows that with an increase in patch width we have better bandwidth characteristics and then lower loss [10]. A more gradual phase variation can be obtained by increasing the dielectric thickness but as noted in part A, in that case the total phase change is reduced to less than 300^{o}. The reduction of the phase range comes from the phase delay produced by the wave traveling back and forth in the grounded substrate when the patch dimension is very small or when the patch is removed. This tells us that at same fixed frequency the maximum possible phase variation that can be achieved by changing the element size is up to 180^{o} on either side of the phase values obtained for the size that makes the element resonate at the given frequency.

Due to the limited phase range that comes with a thick single layer substrate, stacking of two or three varying-sized patches has been found to be a reasonable workaround [2-

4]. It allows gradual phase curves in a range larger than 360^{o}. Figure 2.8 shows a phase curve with high linearity and with large phase variation range that reaches 650^{o}.

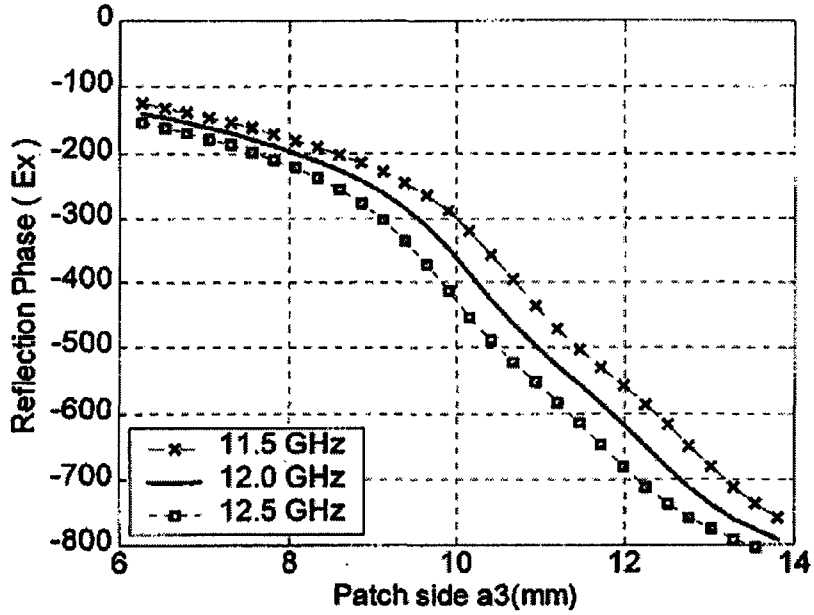

Figure 2.8-Reflected phase versus element length of three stacked variable-size patches layers. (After [3])

It is because an array of metallic patches behaves as a single-resonance circuit that the phase range limited to 360^{o} in best case scenario. By stacking several arrays, a multi resonant behavior is obtained and the phase range can be several times 360^{o}. Then, the dielectric thickness of each layer can be increased to obtain a more gradual and more linear phase variation. This is what describes exactly the phase curves in Figure 2.8. Stacking several arrays needs long and accurate manufacturing processes, however.

Many types of reflectarray elements have been proposed in recent years to improve the element bandwidth of single-layer reflectarray [14-18]. Figure 2.4 (c) has already shown three element types. The double cross loops have been demonstrated by Chaharmir et aliter [18]. A single-layer reflectarray was manufactured and measured, which showed an aperture efficiency of 55% and a 1dB gain bandwidth of 10%. Figure 2.9 shows the phase versus cross loop length curve for a double cross loop reflectarray. It shows a large range

of phase variation but with less linearity compared to the multilayer case, which means more error and less aperture efficiency are expected. In [26] it has been demonstrated that by adding a layer of foam between the dielectric layer and the ground plane with the double cross loop as the radiating element, the linearity increased and the resulting phase curve is way better than double stacked patches phase curves developed using similar thickness foam layer. This is demonstrated in Figure 2.10.

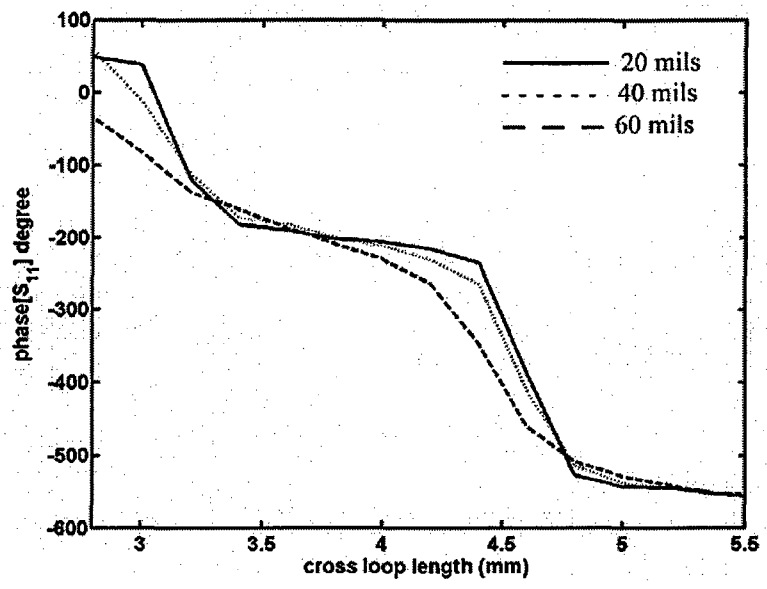

Figure 2.9-Reflected phase versus cross loop length for different substrate thickness. (After [18])

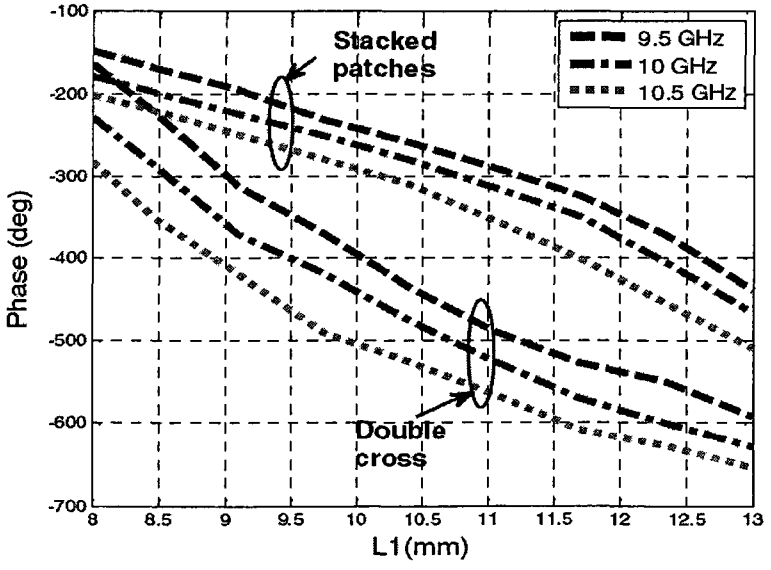

Figure 2.10-Reflected phase versus double cross loop length and stacked patches length at different frequencies. (After [26])

The largest reflectarray bandwidth that has been reported in literature thus far was achieved by Pozar [27]. The artificial impedance surface concept has been employed to achieve 22% bandwidth for a single thin layer of patch length elements with an aperture efficiency of 65%. The patch elements are significantly smaller than resonant size, and spaced on a grid having spacing significantly less than $\lambda/2$. The design is based on the variable surface reactance required to synthesis a holographic reference pattern formed by an incident field and the desired radiated field.

The second reflectarray bandwidth limiting factor is the spatial path delay. Figure 2.11 demonstrates the special path delay concept [28]. ΔS is the difference between the electrical paths S1 and S2. This difference may be several wavelengths at the center frequency for a large aperture reflectarray. Since the phase shift in reflectarray elements is limited to the 360^{o} range, and phase delay is only compensated at the central frequency. The phase error at different frequencies increases for large values of phase delay which in turn produce frequency excursion error in the radiated phase front [11].

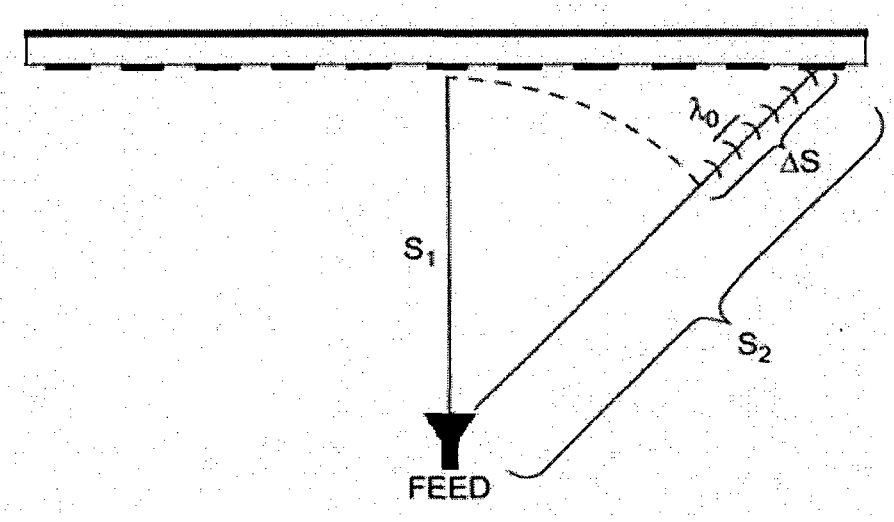

Figure 2.11- Differential spatial phase delay of reflectarray. (Adapted from [11])

The basic ways to reduce ΔS are either to design the reflectarray with a larger focal length (S1) and hence minimize the difference between S1 and S2, or to avoid the use of reflectarray with a large electrical diameter. More sophisticated solutions have been

presented in [11]. One method uses time delay lines or partial time delay lines instead of the phase delays. This method introduces an additional insertion loss and needs real estate for the lines, which makes it more complex and pricy. Another method, which is considered to be one of the more recent developments in the reflectarray field is to use, instead of a complete flat reflectarray surface, a concavely curved reflectarray with piecewise flat surfaces [29]. A reflectarray with piecewise flat surfaces is called the multifacet reflectarray, and is shown in Figure 2.12.

3- Calculating the reflectarray pattern using the available analysis method.

Some electromagnetic simulators, such as HFSS and CST [21, 64], have the possibility of implementing periodicity conditions in their recent versions. Hence we can use them to obtain the curves of reflection phase for a reflectrarray element in an infinite array environment. However, with these simulators it is impractical to analyze and calculate the radiation pattern of a complete reflectarray of a large number of elements. Fortunately reliable approximate analysis techniques have been deployed recently to calculate the radiation patterns of reflectarray exist; these are briefed in Section 2.2.3.

2.2.3 Overview of Some Reflectarray Radiation Pattern Prediction Techniques

Fortunately, the computationally impractical analysis of an array with a large number of elements of unequal size is not essential for a successful reflectarray design. One can use elementary array theory to develop a code that calculates the radiation patterns of a reflectarray based on the calculated phase corrections and approximate closed-form expressions for the pattern of microstrip element, as will be presented in Section 2.5. More complex methods than this have been deployed to calculate the radiation pattern of the reflectarray but until now each such method deployed has its own shortcoming(s), like the inability to include the finite ground plane effects, coupling effects, or the blockage effect in the calculation of the radiation patterns. Moreover none of these methods has been used to do a detailed parametric study or near field calculations. In this thesis we therefore developed a two dimensional moment method code that can perform

an electromagnetic analysis for both reflectarrays and sub-reflectarrays to be able to study all these aspects. It accounts for all effects that might change the phase or amplitude patterns of the reflectarray, like the finite ground plane effects (diffraction effects), coupling effects and the feed blockage effects. A full wave code that can do this in 3D would be prohibitively computationally taxing since even a sub-reflectarray is electrically large and dielectrically inhomogeneous.

It has been reported in [9, 11] that when analyzing reflectarry elements using full-wave techniques it must be remembered that the radiated field is the sum of two components: the field radiated by the patches and the field reflected from the ground plane. Pozar in [9] considered the two components, the specular reflected field from the dielectric substrate and the ground plane (in the absence of microstrip patches) and the scattered field from the patches. The scattering reflection coefficients have been calculated using full-wave moment-method solution then the total field of the reflectarray has been calculated by summing up the individual fields of all elements as given in (2-2) to (2-4) below.

$$\bar{E}^t(\theta,\phi) = \frac{e^{-jkr}}{r} \sum_{i=1}^{N} \bar{\bar{Q}}(\theta,\phi;\theta_i,\phi_i).\left[\bar{E}^r + \bar{E}^s\right] \tag{2-2}$$

$$\bar{E}^r = \begin{bmatrix} R_{\theta\theta} & 0 \\ 0 & R_{\phi\phi} \end{bmatrix} \bullet \bar{E}_f(\theta_i,\phi_i) e^{jk_o\left(x_i \sin\theta\cos\phi + y_i \sin\theta\sin\phi\right)} \tag{2-3}$$

$$\bar{E}^s = \begin{bmatrix} S_{\theta\theta} & S_{\theta\phi} \\ S_{\phi\theta} & S_{\phi\phi} \end{bmatrix} \bullet \bar{E}_f(\theta_i,\phi_i) e^{jk_O\left(x_i \sin\theta\cos\phi + y_i \sin\theta\sin\phi\right)} \tag{2-4}$$

where $\bar{E}^t$ is the total field of the reflectarray, $\bar{E}^r$ is the reflected component of the field, $\bar{E}^s$ is the scattered component of the field for each patch in the reflectarray, $R_{\theta\theta}$ and $R_{\phi\phi}$ are the reflection coefficient, they are function of the incident angles from the feed

plus the dielectric substrate characteristics with an expressions given in [9], $S_{\theta\theta}$ and $S_{\phi\phi}$ are the co-pole scattering coefficients whereas $S_{\theta\phi}$ and $S_{\phi\theta}$ are the cross-pole scattering coefficients, $\vec{E}_f$ is the feed field which is incident upon the ith patch, and finally Q accounts for the transformation from plane wave to a spherical wave and is related to the radar cross section of a square plate. The above method accounts for the finite size of the reflectarray and the cross polarization components but not for inter-element coupling nor for the feed blockage effects.

Two other methods were presented in [1] for the analysis of reflectarrays. The first one is physical optics based. It has been built upon an idea presented in [9] which says that scattering from reflectarrays can be considered a "PO-like numerical integration", and then one may benefit from the general availability of the PO current in many reflector codes like GRASP [65] to estimate the reflected field of reflectarrays. However, PO current must be adjusted to include the phase compensation on the surface of the reflectarray elements by multiplying each element by voltage excitation coefficient that compensates for the phase change. Assuming we have a locally plane wave incident field on x-polarized patch elements, the complex valued excitation coefficient can be defined as

$$\tilde{V}_o^{po} = \frac{\vec{J}_{po}\eta}{2} \bullet \hat{x} = E^i{}_\theta \cos\phi - E^i{}_\phi \cos\theta \sin\phi \qquad (2\text{-}5)$$

where $E^i{}_\theta$, and $E^i{}_\phi$ are the (θ,ϕ) components of the incident field and η is the free space impedance. $\vec{J}_{po}$ is the PO current given as $\vec{J}_{po} = 2\hat{n} \times \vec{H}^i$, where $\hat{n}$ is the unit normal to the surface and $\vec{H}^i$ is the incident magnetic field.

Reflectarray phase compensation is applied to $\tilde{V}_o^{po}$ resulting in a modified coefficient that can be associated with the cosine-q model describing the radiation pattern of each element:

$$\tilde{V}_o^{po} = \tilde{V}_{o(m)}^{po} \frac{e^{-jkr}}{r} \left[\hat{\theta} \cos^{q_x}\theta \cos\phi - \hat{\phi} \cos^{q_y}\theta \sin\phi \right] \qquad (2\text{-}6)$$

where q_x and q_y are the raised cosine factors in x and y planes, r is the distance from the reflectarray to the observation point. The total field is the superposition of all element patterns.

The second method presented in [1] is a coupling based technique which models each element of the reflectarray as a small broad-beam antenna having its own TX/RX characteristics; each element is attached to a voltage source whose strength is dependent on the electromagnetic coupling of the incident field. Each element is assumed to be characterized by a radiation model such as a cosine-q model described above. An inner product of the incident field with the radiation of individual reflectarray elements can result in predicting the coupled incident field onto each array element. The two methods presented in [1] do not account for the contribution that comes from the polarization current induced in the dielectric substrate and do not account for the blockage effect as well. Other methods based on Finite Element Method (FEM) and Finite Difference Time Domain (FDTD) have been presented in [32, 33] respectively.

2.3 Recent Reflectarray Developments

Most of recent research work on reflectarrays concentrates on developing the bandwidth characteristics (other than those depended on the element properties only) of this type of antenna and adding features such as enhancing the pattern scanning capabilities, beam shaping , spatial power combining, power amplification and compacting the over all antenna size.

Starting from early 2000s, many endeavors mitigated the main disadvantage of reflectarrays, namely the narrow bandwidths mentioned earlier in this chapter. These endeavors have been crowned by designing a three-layer stacked patch structure, which extended the phase range of up to 650° by varying the dimensions of the stacked patches [4]. The multilayer structure has been used to design the largest reflectarray in the world, (3-m Ka-band circuraly polarized reflectarray with 200,000 element) [34]. Another important bandwidth related development was that using the multi-facet reflectarray [29].

It consists of many locally flat but globally parabolic reflectarray panels (faces) as shown in Figure 2.12. This configuration minimizes the spatial phase delay contribution that limits the reflectarray bandwidth. Multifacetting is considered to be a significant achievement since even when using multilayer structures, the bandwidth improvement obtained cannot satisfy large reflectarray structures.

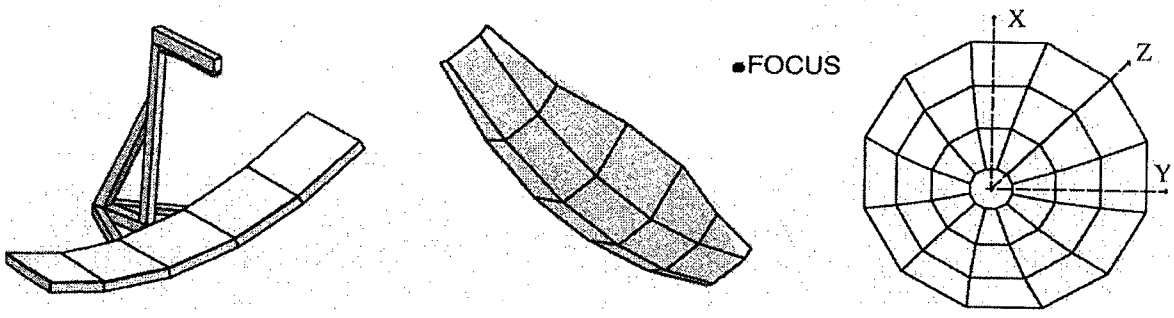

Figure 2.12- Multi-facet Configurations approximating parabolic surfaces. (After [11])

Another important achievement, which is important for spacecraft applications, was the ability to shape the radiation pattern of the reflectarray into a contoured beam [25, 35, 36, 37]. Shaped countered beams are used in satellite applications to provide a specified coverage area on the surface of the earth. This shaping of the beam was accomplished in most cases by using a numerical phase-only synthesis technique where a very large number of elements is used to get the desired countered shaped beams. Basically with this technique the required phase is obtained by changing the dimensions of the array patches, and then optimization is used as a second step to improve the design performance. Figure 2.13 shows an example of the photo etching mask of a reflectarray design that gives shaped contour beams [35]. Another useful recent development for spacecraft applications is the inflatable reflectarray [34, 38, 39]. All reflectarray elements are printed on a thin membrane substrate that is mechanically supported and tensioned at its perimeter by inflatable tubes that decrease the surface rms error. When deflated, this antenna can be rolled up to form a light cylinder that reduces the mass and volume

contribution of the antenna in the lunch vehicle. Figure 2.14 shows an example of inflatable reflectarray.

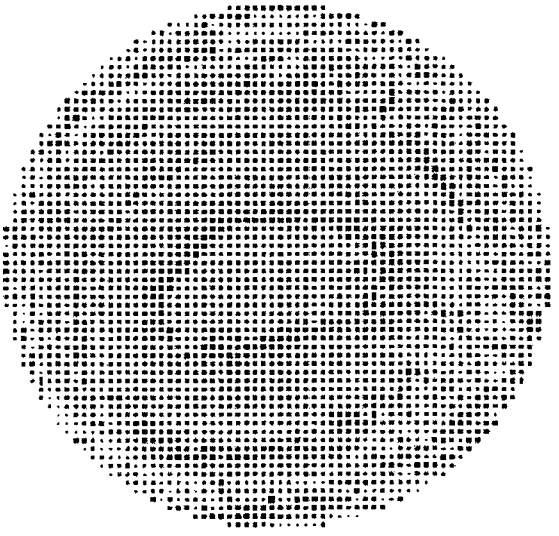

Figure 2.13- Photo-etching mask of the first layer of the shaped beam reflectarray. (After [35])

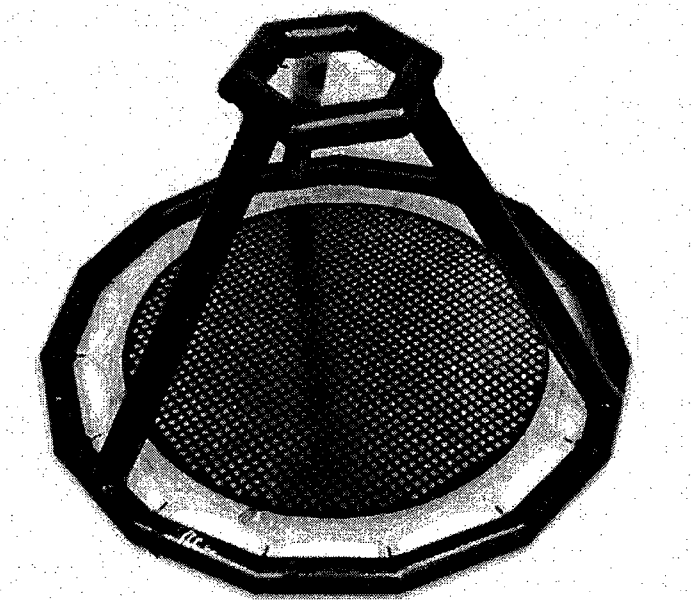

Figure 2.14- 1-m X-band inflatable microstrip reflectarray with circular polarization. (After [38])

A reflectarray that works as an antenna and spatial power combiner concurrently was described in [10, 40]. Unlike previous work on power combining using reflectarrays [41], this work did not include any active devices in its integration. The idea can be understood from Figure 2.15. Multiple feeds were used to illuminate the reflectarray to get a high gain single beam in the broadside direction. To achieve that the phase correction factor (ψ_n) presented in [9] must be selected in such a way that makes the total phase from all feeds constant for all patches to end up with a planar phase front.

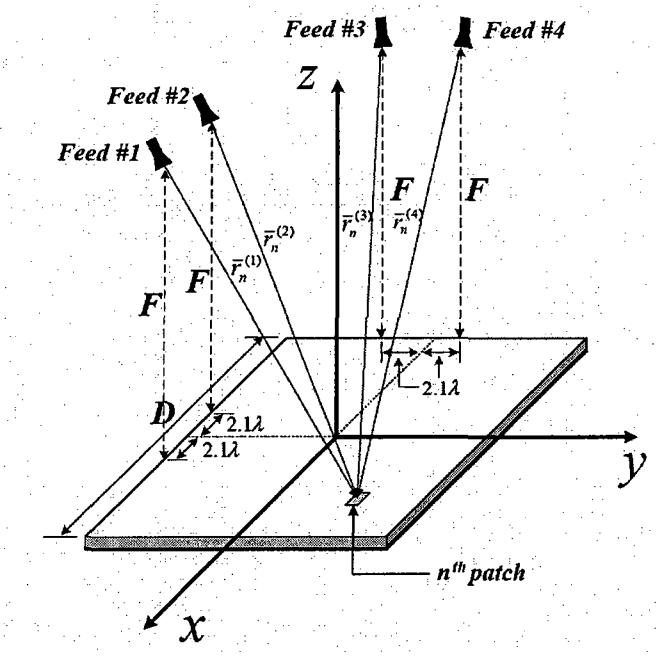

Figure 2.15- Geometry of Four feeds spatial power combining Reflectarray. (After [10])

Recently much has been done to benefit from the capability to achieve beam scanning using reflectarrays [42, 43, 44]. In [42] voltage-controlled varactor diodes were used to control the phase of equal size reflectarray patches as shown in Figure 2.16. Basically each rectangular element is split at the middle and connected at the edges by two varactor diodes. By varying the applied voltage across the diode terminals, their capacitances are changed and thus the patch electrical phases are changed. A beam scanning of $\pm 70^{\circ}$ has been achieved with a 70 element C-band reflectarray as shown in

Figure 2.16. To allow continuous tuning of the reflected signal phase over 360^{o} range, a special reflectarray element has been presented in [43]. It consists of a patch printed on a flexible membrane substrate, aperture-coupled to a transmission line loaded with two varactor diodes. At C-band the loss in the varactor diodes was low. It would be higher at millimeter wave frequencies. In order to overcome this Hum and Okoniewski [44] presented a new low-loss technique that uses low loss micro-electro mechanical devices. (MEMS).

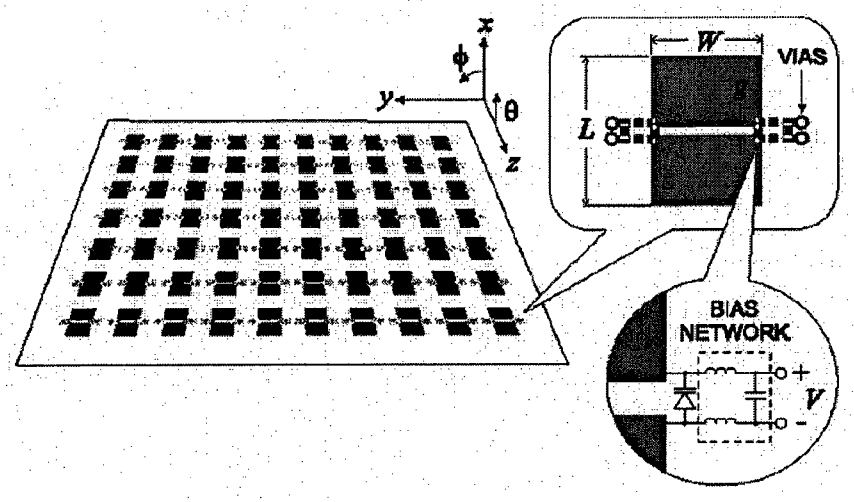

Figure 2.16- Geometry of the beam scanning reflectarray with tunable varactor diodes. (After [42])

One of the most recent innovations is the reconfigurable reflectarray. Re-configurability is generally used to change the antenna radiation pattern. Many ways have been used to embed the re-configurability into the antenna structure. One is typically accomplished by using solid state tuning devices (diodes, transistors) which are integrated within the radiating element of the reflectarray to modify the phase or/and the amplitude the of the signal transmitted or received by the radiating element. In [51], a reflecting element having a stub loaded with a single p-i-n diode that achieves single-bit quantized phase shift at 60 GHz has been used to configure the radiation patterns of a reflectarray. Re-configurability was obtained in [52, 53] by exploiting the voltage dependent dielectric properties of liquid crystal. In [54-56] various ways are proposed to

employ MEMS tuning devices for re-configuring a reflectarray. In the second type of tuning methods, the radiating elements are separated from the phase shifter (the tuning device), and electromagnetically coupled to it. An example of such approach is given in [43, 57]. In [57] whose reflectarray is shown in Figure 2.17, a novel aperture coupled method was used where the phases of the elements of the reflectarray (consisting of identical rectangular patches) are controlled by aperture coupling slots whose lengths are changed by using photo- induced plasma. The optical excitation (light) illuminates the slots through an optical mask. The plasma being illuminated by the light changes the slot length, which changes accordingly the phase distribution of the reflectarray elements.

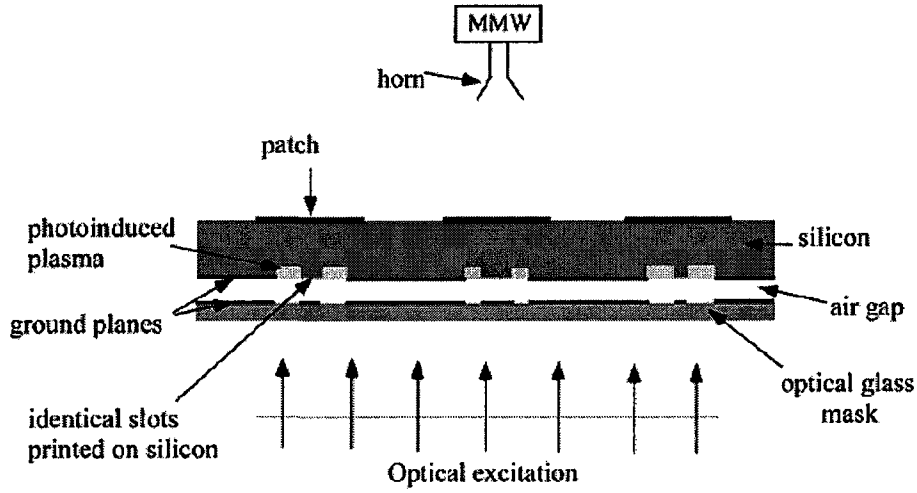

Figure 2.17- Schematic view of a single layer reflectarray with optically controlled slots on the ground plane. (After [57])

It has been reported recently [45] that by introducing a phase progression on the surface of the sub-reflectarray in a dual reflector system, the main beam of the parent reflectarray (or reflector) can be scanned by an angle proportional to the phase progression defined. This method would help in achieving beam scanning with lower loss, and is simpler to implement because sub-reflectarray are so much smaller.

An innovative development that entered the world of reflectarray design in1998 was the folded reflectarray [46]. The main target at first was to come up with a low profile reflectarray by using the configuration shown in figure 2.18. Two reflecting surfaces

were used to reduce the overall reflectarray profile. The feed radiates a linearly polarized wave which is reflected back by a polarizing mesh. The reflected field then illuminates the reflectarray elements which are designed to both realize the compensating phase and to transform the polarization to the orthogonal sense, thus leading to radiation of the wave through the polarizing mesh into space. Recently folded reflectarrays have been designed to perform beam shaping and multiple beam generation [47], as well as two-dimensional beam scanning [48]. Designs have been extended to dual mode folded reflectarray in the millimeter-wave band [49] and methods found for increasing the phase angle range with good linearity [50].

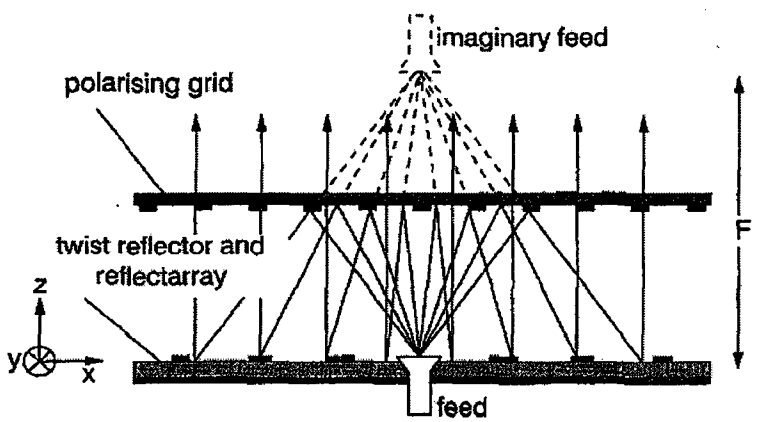

Figure 2.18- Principle of Folded Refelectarray antenna. (After [46])

Over the last five years there has been increasing interest in sub-reflectarrays. These are reflectarrays which emulates ellipsoidal and hyperbolic subreflectors used in the dual reflectarray systems. Sub-reflectarrays offer the promise of more flexibility in beam shaping and beam scanning as well as bandwidth improvements. Sub-reflectarrays will be discussed in Section 2.4.

2.4 Sub-Reflectarrays

2.4.1 Preliminary Remarks

As we mentioned earlier the sub-reflectarray basically is that type of reflectarray that emulate curved reflectors other than the parabolic reflector, such as the ellipsoidal and the hyperboloidal subreflectors of dual reflector systems. As such the reflected phase front scheme from the sub-reflectarray is not a uniform phase front (which generates a pencil beam) since it should retain the spherical phase front of the impinging wave from the feed after reflection to emulate the functionality of solid ellipsoidal or hyperboloidal subreflectors.

Due to its small electrical size compared with a reflectarray, the sub-reflectarray shows better bandwidth characteristics since the spatial path delay is much smaller. The ΔS of Figure 2.11 is small and does not influence the bandwidth significantly. Moreover the small electrical size of sub-reflectarray makes beam scanning capabilities more efficient via a sub-reflectarray, since the beam can be scanned or reconfigured by controlling the phase at the elements of the reduced-size reflectarray (that is sub-reflectarray) as reported in [25, 37]. In [45] a sub-reflectarray has been used to scan the main beam of the parent reflectarray by defining a progressive phase on the sub-reflectarray surface. Encinar in [37] has used the sub-reflectarray in a dual reflector configuration to shape the overall system beam to get a countered beam for satellite coverage application. Another advantage of the sub-reflectarray that has been reported recently is its usage to compensate for the surface distortion of the parent curved reflector which gives it much merit over the classical solid subreflector [58].

2.4.2 Review of Sub-Reflectarrays

A. Preliminary Comments

In recent years the design of sub-reflectarrays has attracted researchers' attention due to the potential advantages expected to be drawn from such electrically small planar microstrip array antenna, not the least of which the development of bandwidth characteristics, beam shaping and beam scanning capabilities. One should keep in mind that all the advantages of reflectarray mentioned in section 2.2.1 are advantages of sub-reflectarray since the sub-reflectarray is no more than a reflectarray that emulates a subreflector of any usable shape (mainly the ellipsoidal and hyperbolic subreflectors). As such the low profile, low cost and ease of manufacturing are still very desirable advantages that we need through the design of sub-reflectarrays. It is worth mentioning that the first endeavor to design a sub-reflectarray was reported [59] in 2007, which shows how recent the topic is. Sub-reflectarrays have been designed to replace the sub-reflectors in dual reflector antenna systems [37, 58, 59], both for conventional Casserain and Gregorian systems and for main reflector distortion compensation. In references [37, 59] the main reflector was a classical solid parabolic reflector. A more detailed study compared to [37, 59] has been reported in [12]. An experimental validation of the work presented in [12] was reported in [45]. In [60] an analysis of a dual reflectarray system has been presented in which both the main reflector and the subreflector were reflectarrays.

B. Sub-Reflectarrays for Main Reflector Distortion Compensation

Y.Rahmat-Samii [58] has shown that a sub-reflectarray can compensate for the surface distortion of the main reflector, and then showed in [61] that the sub-reflectarray can be used to compensate for the spherical aberration of a spherical main reflector. In [58] and [61] no simple phase equation is given, using which the required patch sizes can be set. Instead direct optimization is used to adjust the patches dimensions in such a way

that the sub-reflectarray compensates for the main reflector surface distortion or phase aberration.

In [58] the goal was to enhance the performance of the dual reflector antenna system by compensating for distortions that may be introduced during the manufacturing process of the surface of the main parabolic reflector. A sub-reflectarray has been used to achieve that compensation. By properly adjusting the element reflection phases, the phase errors caused by the main reflector surface distortion are compensated for, resulting in a better antenna performance. A set of patches with variable sizes are designed and measured using X-band waveguides, and a sub-reflectarray implemented with them was used to compensate for a distorted main reflector antenna. The results of the simulation and measurements that have been done shows the performance of the antenna was improved (gain, side lobe level), as was the symmetry of the far field pattern. In [61] the sub-reflectarray has been used for a similar reason, but this time the sub-reflectarray compensating technique is used to mitigate the spherical aberration of a spherical reflector. The reflection phase of each reflectarray element was adjusted (optimized) so that an equal phase distribution was achieved at the aperture of the spherical reflector, and the spherical phase aberration is thus corrected. The conjugate field matching (CFM) method was employed to achieve the desired phase shift of the sub-reflectarray. As stated in [59], the CFM "is based on the fact that the product of phase-distorted field and its complex conjugate results in a plane wave, and has been applied to various array feed designs".

C. Sub-Reflectarrays in Cassegrain and Gregorian Systems

In [37, 45, 59, 60] Encinar used Pozar's phase design equation [9] for a reflectarray that emulates a paraboloidal reflector in its general form

$$\psi_l = k\left\{d_l - \sin\theta_o\left(x_l\cos\varphi_o + y_l\sin\varphi_o\right)\right\} \tag{2-7}$$

to account for the offset configuration. The symbols are defined in Figure 2.19. Quantity ψ_l is the correction phase that must be provided by element l to maintain a planar phase

front at the surface of the sub-reflectarray. The (x_l, y_l) are the coordinates of the center of element l, k is the free space wave number. The θ_o and φ_o are the angles measured from the z- and x-axis in the z-x and x-y planes, respectively. The derivation of the general phase design equation will be detailed in Chapter 3.

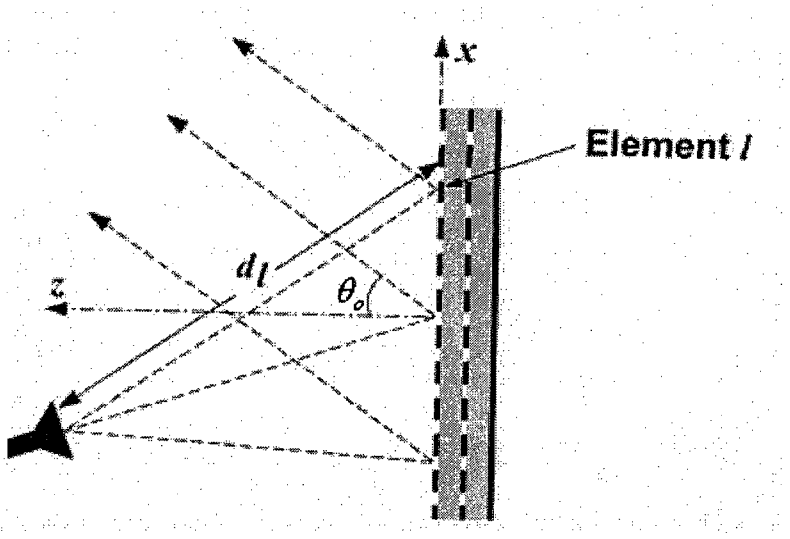

Figure 2.19- Phase equation (2-7) generation configuration. (After [3])

An iterative routine has been used to change patch dimensions in such a way that give same phase shift in every element has been used. Encinar's technique to change the dimensions of the sub-reflectarray patches is unusual. Nevertheless the overall system radiation pattern looks excellent in his papers. He aims to get the same phase at each element so that a plane wave is generated and propagates towards the main reflector, while theoretically it should be a spherical wave front (to achieve a uniform or semi-uniform phase in the main reflector or reflectarray aperture with the minimum phase error possible).

No details are given in [37, 45, 59, 60] about the amplitude and phase patterns from the sub-reflectarray. All we can deduce is that the patch dimensions have somehow been optimized to get the required overall system radiation patterns, and that is possible to do this using multilayer patch elements for the sub-reflectarray.

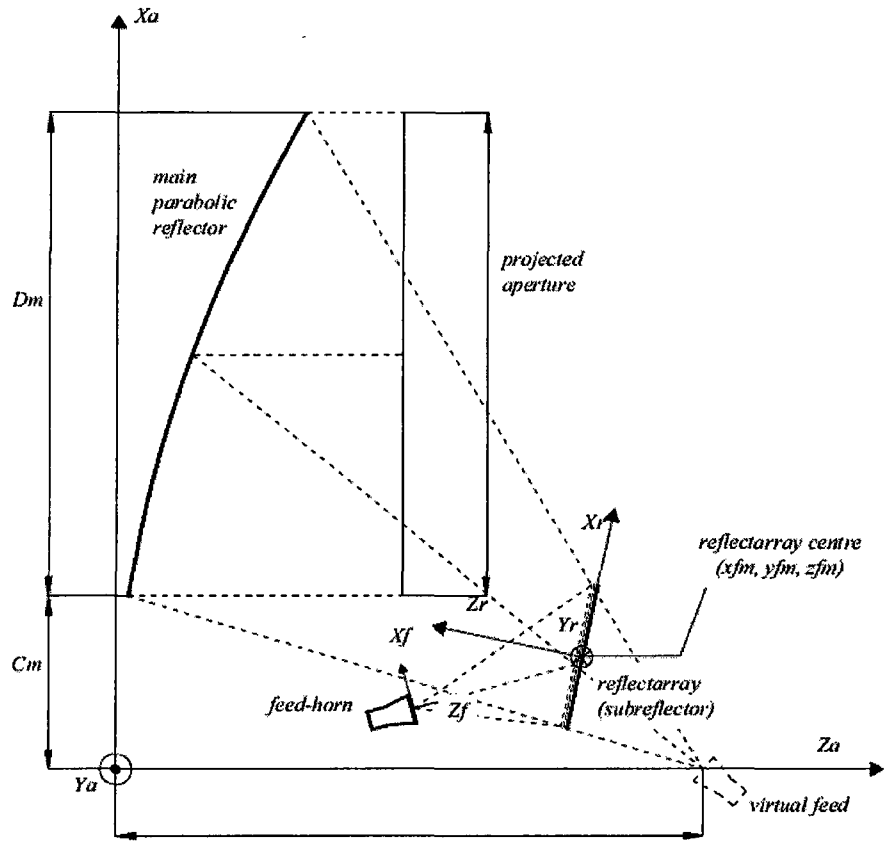

Figure 2.20- Cassegrain dual reflector antenna with sub-reflectarray as subreflector. (After [59])

The above-mentioned technique has been used in the emulation of a hyperboloidal subreflector of a Cassegrain as presented in [59] and shown in Figure 2.20, whereas in [37] a sub-reflectarray is used to replace a solid ellipsoidal subreflector. The effect introduced by the ellipsoid was emulated by introducing the suitable phase shift at each element of the sub-reflectarray using equation

$$\psi = 2k\,z_r \tag{2-8}$$

where ψ is the reflection phase at each element of the sub-reflectarray needed to compensate for the curvature of the ellipsoid and z_r is the perpendicular distance, measured in the (x_r, y_r, z_r) coordinate system, between each sub-reflectarray element in

the $X_r - Y_r$ plane and the solid ellipsoid. Equation (2-8) is "derived" using Figure 2.21. It is used to obtain starting values for the reflection phase distribution, after which optimization is used to obtain the final reflection phase values.

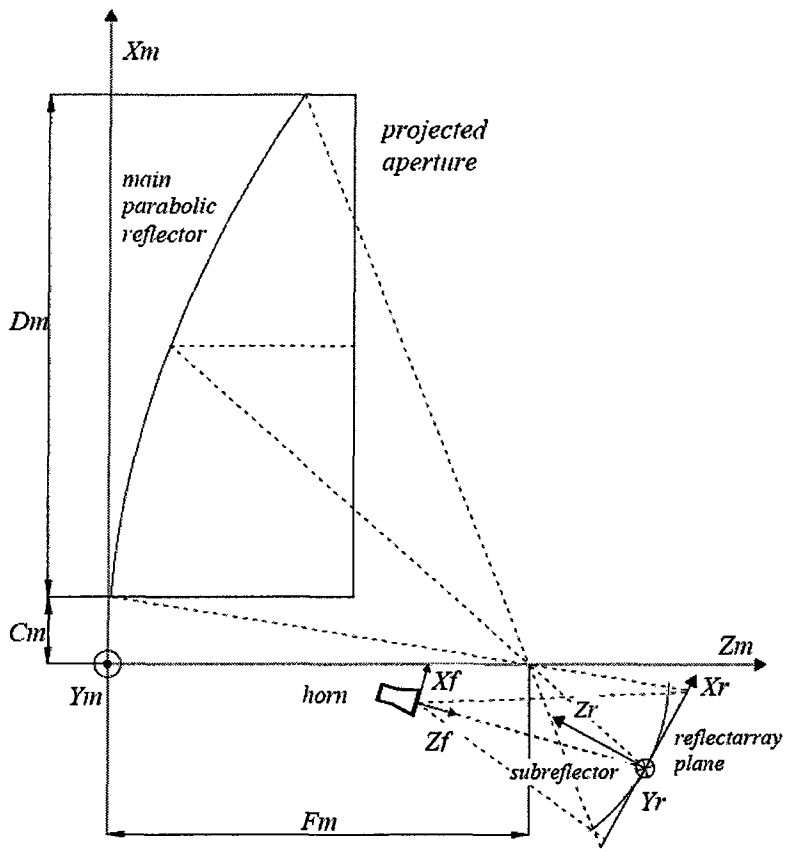

Figure 2.21- Gregorian dual reflector antenna with sub-reflectarray as subreflector. (After [37])

It is understood from [37] that Encinar used equation (2-8) to compensate for the effect of the ellipsoidal sub-reflector curvature and he compensated for phase delay differences of the feed rays using equation (2-7). It is clear from Figure 2.21 that equation (2-8) is an approximation since it is not an accurate way to compensate for the curvature of the ellipsoidal profile using vertical projections between the centers coordinates of the sub-reflectarray elements and the ellipsoid surface. It is known that the impinging waves are spherical and thus hit the subreflector at different incident angles which should be the

case of the reflected rays as well. Note that the reflected rays all pass through the virtual focal point of the ellipsoid.

The moment method has been used in [37, 45, 59, 60] to calculate the reflected field of the sub-reflectarray. The analysis is carried out element by element, and in the calculation of each component of the reflected field the cross polarization introduced by the patches is considered, so that the reflected field of each patch is (using the coordinate system of Figure 2.20)

$$\bar{E}_{ref}(x_r, y_r) = \bar{\bar{P}} \cdot E_{inc}(x_r, y_r)$$

$$\bar{\bar{P}} = \begin{bmatrix} p_{xx} & p_{xy} \\ p_{yx} & p_{yy} \end{bmatrix} \tag{2-9}$$

The components of the $\bar{\bar{P}}$ matrix are complex and they are calculated for each periodic cell by full-wave analysis based on the method of moments [30]. Local periodicity and the real angle of incidence of the wave coming from the feed are considered at each element. By "local periodicity" we mean that, when computing (using the method of moments) the reflected field of each patch, that patch is assumed to lie in an infinite periodic structure of identical patches, and an the incidence angle of the exciting plane wave assigned the actual angle between the real feed and the patch. Thus the moment method has to be re-executed for each of the patches in the sub-reflectarray. The actual complete sub-reflectarray is not being analysed using a full-wave analysis. In essence the full-wave anlaysis is being used to compute the exciation of each patch in turn under an infinite aray assumption. Niether the finite ground plane effect or any aperture blockage can feasibly be included in the analysis. This justifies the discrepancies between the simulated and the measured results in [12, 45].

D. Limitations of Existing Work on Sub-Reflectarrays

It is evident from all sub-reflectarray works that have been reported thus far that there are no key designs equations, analogous to that of the parabolic case [9], for sub-

reflectarrays that emulate the hyperboloidal and ellipsoidal sub-reflectors. We need such design equations to get a spherical phase front over the surface of the main reflector. In this thesis we have derived these equations and validated them by simulation and measurements, as will be demonstrated in Chapter 4. Moreover, nobody thus far has studied the details of the reflected fields of sub-reflectarrays in manner similar to that Rusch [66] has done for the scattered fields of solid hyperboloidal subreflectors. As such a detailed study of the sub-reflectarray scattered field (both the amplitude and phase patterns) has been done in this research work with a parametric study of all associated features like focal point locations, edge taper effects, eccentricity change, and so on. The analysis techniques that have been used to analyze the sub-reflectarray (and reviewed in Section 2.2.3) are difficult to be used to study all sub-reflectarray features since using 3d full wave code is electrically large and dielectrically inhomogeneous. Hence in this thesis we developed a two-dimensional moment method code that can perform an electromagnetic analysis for both reflectarray and sub-reflectarrays that is very accurate and accounts for border diffraction and feed blockage effects on the reflected field of sub-reflectarrays.

2.5 Radiation Pattern Calculation of Sub-Reflectarray Using Array Theory

Once we know the patch dimensions that generate the required compensating reflection phases determined using an appropriate phase design equation the far field radiation patterns can be calculated using the classical array theory. The calculation of reflectarray or sub-reflectarray radiation patterns using array theory has been reported in many references [9, 10, 11, 40]. Such an analysis is generally good enough to verify the phase equation and gives close results compared with measurements [40], at least for parabolic-type reflectarrays and for the far-zone amplitude patterns. In this thesis we are concerned about both amplitude and phase far-field radiation patterns of the sub-reflectarrays. Hence some adjustments have been added in the array analyses which were not reported elsewhere.

Consider the reflectarray shown in Figure 2.3 and assume it contains N reflecting elements (patches) that are uniformly illuminated by a feed located at the focal point of the reflectarray (prime focus). If all elements are located in the X-Y plane then the position vector $\overline{r_n}$ can be expressed as

$$\overline{r_n} = x_n\hat{x} + y_n\hat{y} \tag{2-10}$$

Based on that we can write the array factor of the planar reflectarray as

$$AF(\theta,\phi) = \sum_{n=1}^{N} a_n e^{jk_o(x_n \sin\theta\cos\phi + y_n \sin\theta\sin\phi)} \tag{2-11}$$

The term a_n in equation (2-11) is the relative complex current excited on the n^{th} patch. It can be be written as

$$a_n = M_n e^{jP_n} \tag{2-12}$$

Since a horn-feed is illuminating the individual patches of the reflectectarray we can consider that the excitation terms M_n and P_n to be proportional to the magnitude and phase of the reflected electric field at the n^{th} patch, respectively. If we assume the feed has a very wide beam (locally uniform on the reflectarray surface), Then typically the only factor that effects the reflected field at each patch is the distance between the feed phase center (R_n) and the n^{th} element phase center. Based on that, the complex excitation term a_n can be expressed in the (not yet complete) form

$$a_n = \frac{1}{|R_n|} e^{-jR_n} \tag{2-13}$$

In reality to optimize the reflectarray performance, the feed has to provide a certain angular taper over the reflectarray surface. This angular taper can be incorporated in the

reflectarray pattern analysis by multiply the relative complex excitation term by a raised cosine factor ($\cos\theta_n^q$) [62] which accounts for the taper effect by adjusting q to match the pattern of the actual feed. Including this angular taper, and multiplying the a_n by the compensating phase factor $e^{-jk\psi_n}$, with ψ_n obtained based upon the particular phase compensation equation of interest (parabolic, ellipsoidal or hyperbolic), we end up with

$$a_n = \frac{\cos\theta_n^q}{|R_n|} e^{-j(kR_n - \psi_n)} \tag{2-14}$$

Substitution of (2-14) into (2-11) gives the array factor

$$AF(\theta,\phi) = \sum_{n=1}^{N} \frac{\cos\theta_n^q}{|R_n|} e^{-jk\,(R_n + x_n\sin\theta\cos\phi + y_n\sin\theta\sin\phi) + j\psi_n} \tag{2-15}$$

Now that we have determined an expression for the array factor, we consider the pattern of each element of the reflectarray. To do this first let us consider a single microstrip patch described in Figure 2.22 The far field radiation pattern for this microstrip patch is given to a good approximation by [63] as

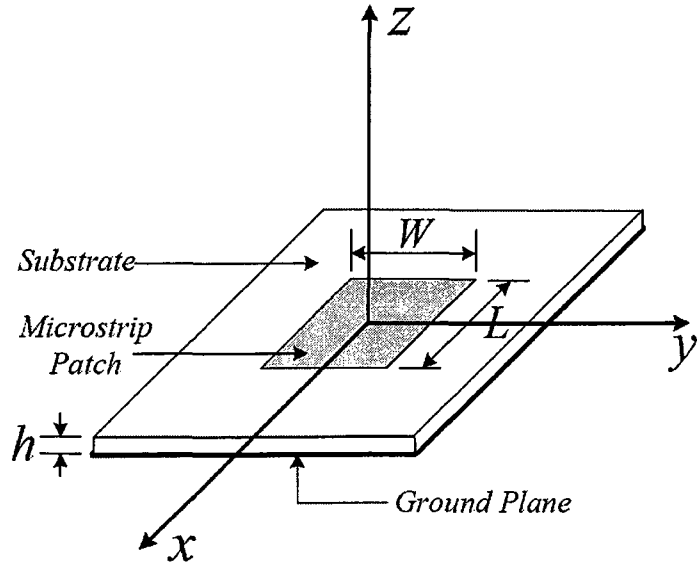

Figure 2.22- Microstrip Patch Geometry. (After [9])

$$E_{\theta}^{(n)}(\theta,\phi)=\frac{-\sin(W_n)\cos(L_n)\cos\phi\left(\varepsilon_{eff}-\sin^2\theta\right)}{W_k\left(\varepsilon_{eff}-\sin^2\theta\cos^2\phi\right)} \tag{2-16}$$

$$E_{\phi}^{(n)}(\theta,\phi)=\frac{\sin(W_n)\cos(L_n)\varepsilon_{eff}\cos\theta\sin\phi}{W_n\left(\varepsilon_{eff}-\sin^2\theta\cos^2\phi\right)} \tag{2-17}$$

where

$$\varepsilon_{eff}=\frac{\varepsilon_r+1}{2}+\frac{\varepsilon_r-1}{2}\left(1+12\frac{h}{w}\right)^{-\frac{1}{2}} \tag{2-18}$$

$$L_n=\frac{k\ (L+2\Delta L)}{2}\sin\theta\cos\phi \tag{2-19}$$

$$W_n=\frac{k\,w}{2}\sin\theta\sin\phi \tag{2-20}$$

and

$$\Delta L=\frac{0.412h\left(\varepsilon_{eff}+0.3\right)\left(\frac{w}{h}+0.264\right)}{\left(\varepsilon_{eff}-0.258\right)\left(\frac{w}{h}+0.8\right)} \tag{2-21}$$

Since the reflectarray is made up of patches of varying lengths L, the element pattern at each patch will be different and it will be a function of L_n (i.e. the length of the *n-th* patch). With this in mind we can write final form of the far-field pattern of the sub-reflectarray as

$$\begin{aligned}\overline{E}(\theta,\phi)=\hat{\theta}\sum_{n=1}^{N}\frac{\cos\theta_n^{\,q}}{|R_n|}E_{\theta}^{\,n}(\theta,\phi,L_n)e^{jk\,(R_n+x_n\sin\theta\cos\phi+y_n\sin\theta\sin\phi)-j\psi_n}\\ +\hat{\phi}\sum_{n=1}^{N}\frac{\cos\theta_n^{\,q}}{|R_n|}E_{\phi}^{\,n}(\theta,\phi,L_n)e^{jk\,(R_n+x_n\sin\theta\cos\phi+y_n\sin\theta\sin\phi)-j\psi_n}\end{aligned} \tag{2-22}$$

We have assumed that the element pattern has little effect on the coupling of the feed fields to the patch.

Equation (2-22) allows us to compute the reflectarray or sub-reflectarray amplitude and phase far-field patterns. The phase patterns of the sub-reflectarray obtained from (2-22) are referenced to the coordinate origin; this coordinate system will be defined in Chapter 3. We can determine the phase pattern with respect to any point z_{ref} on the z-axis by simply multiplying the expression given in (2-22) by the factor $e^{\pm k z_{ref} \cos\theta}$ depending upon the position our reference point with respect to the coordinate origin. This is important since we will want to know what the phase pattern is referenced to the virtual focal points of the ellipsoidal and the hyperbolic sub-reflectarrays.

It is worth mentioning here that the field patterns calculated by equation (2-22) are the reradiated fields from all elements plus the specular reflection from the ground plane /dielectric, since these effects are all incorporated in the element pattern expressions (2-16) and (2-17). The edge diffracted field from the edges of the ground plane is not included in this analysis.

2.6 Concluding Remarks

In Section 2.2 the reflectarray antenna concept was presented. We supported the discussion through a review of many reflectarry configurations (e.g. single layer and multilayer), analysis techniques, recent developments (e.g. beam shaping) and a design procedure for the single layer and multilayer configurations. The general design procedure for reflectarrays that use variable-size patches was outlined. This enabled us to consider the phasing and bandwidth, both of these being key aspects in the understanding of reflectarray operation and limitations. Section 2.3 briefly listed the most recent achievements and developments in reflectarray antennas. Many of these are fertile ground for future research, especially the sub-reflectarray, which can perform many desirable functions like beam scanning and beam shaping more efficiently than can reflectarrays. Section 2.4 introduced the sub-reflectarray concept, and mentioned some of its potential advantages over solid sub-reflectors. A review of sub-reflectarray work to date was given. We identified the fact that no basic phase design equations exist for sub-reflectarrays (that emulate hyperboloidal or ellipsoidal sub-reflectors) as exists for reflectarrays (that emulate parabolic main reflectors). The derivation of such equations and their validation both theoretically and experimentally, is the subject of Chapters 4 and 5 of this thesis. Finally, Section 2.5 outlined an aapproximate, yet reliable, method for the prediction of the radiation patterns of sub-reflectarrays based on elementary array analysis. Although not new, some refinements were provided, and the details (which do not appear to be given elsewhere) have been included here.

2.7 References for Chapter 2

[1] B. Khayatian, Y. Rahmat-Samii and J. Huang, "Radiation characteristics of reflectarray antennas: Methodology and applications to dual configurations", *Antennas and Propagation European Conference*, EuCAP, pp.1-12, November 2006.

[2] D.I. Wu, R.C. Hall, and J. Huang, "Dual-frequency microstrip reflectarray", *IEEE International Symposium on Antenna and Propagation*, Vol. 4, pp.2128-2131, June 1995.

[3] J.A. Encinar, "Design of two-layer printed reflectarrays using patches of variable size", *IEEE Transactions on Antenna and Propagation*, Vol. 49, No. 10, pp. 1403-1410, October 2001.

[4] J.A. Encinar and J.A. Zornoza, "Broadband design of three-layer printed reflectarrays", *IEEE Transactions on Antenna and Propagation*, Vol. 51, No. 7, pp. 1662-1664, July 2003.

[5] D.C. Chang and M.C. Huang, "Microstrip reflectarray antenna with offset feed", *Electronic Letters*, Vol. 28, No.16, pp. 1498-1491, July 1992.

[6] R.D. Javor, X.D. Wu and K. Chang, "Offset feed microstrip reflectarray antenna", *Electronic Letters*, Vol. 30, No.17, pp. 1363-1365, August 1994.

[7] H. Deguchi, N. Takagi, M. Tsuji, and H. Shigesawa, "Microstrip reflectarray with offset feed for improving effective aperture area", *IEEE International Symposium on Antenna and Propagation*, Vol. 3, pp.290-293, June 2003.

[8] S.D. Targonski and D.M. Pozar, "Minimization of beam squint in microstrip reflectarrays using an offset feed", *IEEE International Symposium on Antenna and Propagation*, Vol. 2, pp.1326-1329, July 1996.

[9] D.M. Pozar, S.D. Targonski and H.D. Syrigos, "Design of millimeter wave microstrip reflectarrays", *IEEE Transactions on Antenna and Propagation*, Vol. 45, No. 2, pp. 287-295, February 1997.

[10] F.N. Arpin, "Multi-feed spatial power combining reflectarrays", *Masters Thesis,* University of Ottawa, Ontario, Canada, pp. 18-23, September 2004.

[11] J. Huang and J.A. Encinar, *Reflectarray Antennas*, IEEE Press. New York: John Wiley & Sons, pp. 82-85, 2008.

[12] M. Arrebola, L. Haro and J.A. Encinar, "Analysis of dual-reflector antennas with a reflectarray as subreflector", *IEEE Transactions on Antenna and Propagation Magazine*, Vol. 50, pp. 39-51, December 2008.

[13] C. Tienda, M. Arrebola, J.A. Encinar , G. Toso and C. Mangenot, " Analysis of dual- reflectarray antenna", *ESA antenna workshop* , Netherlands, May 2009.

[14] S.D. Targonski and D.M. Pozar, "Analysis and design of a reflectarray using patches of variable size", *IEEE International Symposium on Antenna and Propagation*, Vol. 3, pp.1820-1823, June 1994.

[15] S. Dubois, J. Shaker and Y. Antar, "Circularly polarized reflectarray using microstrip dipoles", *ANTEM*, St. Hubert, Quebec, pp. 493-496, July 2002.

[16] C. Han and K. Chang, "Ka-band reflectarray using ring elements", *Electronic Letters*, Vol. 39, No.6, pp. 491-493, March 2003.

[17] M.R. Chaharmir, J. Shaker, M. Cuhaci, and A. Ittipiboon, "A broadband reflectarray antenna with double square rings", *Microwave and Optical Technology Letters*, Vol. 48, No. 7, pp. 1317-1320, July 2006.

[18] M.R. Chaharmir, J. Shaker, M. Cuhaci, and A. Ittipiboon, "Broadband reflectarray antenna with double cross loops", *Electronics Letters*, Vol. 42, No. 2, pp. 65-66, January 2006.

[19] J. Huang, " Microstrip reflectarray", *IEEE Antennas and Propagation Society International Symposium,* Vol. 2, pp. 612-615, June 1991.

[20] J. Huang and R.J. Pogorzelski, "A Ka-band microstrip reflectarray with elements having variable rotation angles", IEEE *Transactions on Antenna and Propagation* Vol. 46, pp. 650-656, May 1998.

[21] Ansoft Corporation, Four Station Square, Suite 200, Pittsburgh, PA 15219-1119, USA. HFSS, (High Frequency Structure Simulator).

[22] EMAG Technologies Inc., 1340 Eisenhower Place, Ann Arbor, Michigan 48108. EMPiCASSO.

[23] S. Xu, H. Rajagopalan, Y.Rahmat-Samii and W.A. Imbriale, "A novel reflector surface distortion compensating technique using a sub-reflectarray", *IEEE International Symposium on Antenna and Propagation*, pp.5315-5318, June 2007.

[24] D.M. Pozar and S.D. Targonski, "A microstrip reflectarray using cross dipoles", *IEEE International Symposium on Antenna and Propagation*, Atlanta, pp. 1008-1011, July 1998.

[25] D.M. Pozar, S.D. Targonski, and R. Pokuls "A shaped beam microstrip patch reflectarray", IEEE *Transactions on Antenna and Propagation*, Vol. 47, No.7, pp. 1167-1173, July 1999.

[26] M.E. Bialkowski, A.M. Abbosh and K.H. Sayidmarie, "Investigations into phasing characteristics of printed single and double cross elements for use in a single layer microstrip reflectarray", *IEEE Antennas and Propagation Society International Symposium,* pp. 1-4, July 2008.

[27] D.M. Pozar,"Wideband reflectarray using artificial impedance surface", *Electronic Letters*, Vol. 43, No.3, pp. 148-149, February 2007.

[28] J. Huang, "Bandwidth study of microstrip reflectarray and a novel phased reflectarray concept", *IEEE Antennas and Propagation Society International Symposium,* pp. 582-585, June 1995.

[29] R. Hodges and M. Zawadzki, "Design of large dual polarized Ku-band reflectarray for spaceborne radar altimeter", IEEE *Antennas and Propagation Society Symposium,* pp. 4356-4359, June 2005.

[30] C. Wan and J.A. Encinar, " Efficient computation of generalized scattering matrix for analyzing multilayered periodic structures", IEEE *Transactions on Antenna and Propagation*, Vol. 43, No. 7, pp. 1233-1242, October 1995.

[31] R. Mittra, C.H. Chan and T. Cwik, "Techniques for analyzing frequency selective surfaces a review", *Proceedings of the IEEE,* pp. 1593 – 1615, December 1988.

[32] I. Bardi, R. Remski, D. Perry and Z. Cendes, " Plane wave scattering from frequency selective surfaces by finite element method", *IEEE Transactions on Antenna and Propagation* , Vol. 38, No. 2, pp. 641-644, March 2002.

[33] P. Harms, R. Mittra and K. Wae, " Implementation of periodic boundary conditions in finite-difference time-domain algorithm for FSS structures", IEEE Transactions on Antenna and Propagation,Vol. 42, pp. 1317-1324, September 1994.

[34] J. Huang, V.A. Feria and H. Fang, " Improvement of the three-meter Ka-band inflatable reflectarray antenna", IEEE *Antennas and Propagation Society Symposium,* Vol. 1, pp. 122-125, July 2001.

[35] J.A. Encinar and J.A. Zornoza, " Three- Layer printed reflectarrays for contoured beam space applications", *IEEE Transactions on Antenna and Propagation*, Vol. 52, No. 5, pp. 1138-1148, May 2004.

[36] J.A. Encinar , L. Datashvili, J.A. Zornoza, M. Arrebola , M.Seerra, J.L Besada, H.Baier and H. Legacy, " Dual-Polarization dual-coverage reflectarray for space applications", *IEEE Transactions on Antenna and Propagation*, Vol. 54, pp. 2827-2837, October 2006.

[37] M. Arrebola, L. de Haro, J.A. Encinar, and L.F. de la Fuente, "Contoured- beam gregorian antenna with a reflectarray as a sub-reflector", *Proc. 2nd European Conf. Antennas Propagat. (EuCAP'2007)*, pp.1-6, Nov.2007.

[38] J. Huang and A. Feria, "A one –meter X-band inflatable reflectarray antenna", *Microwave and Optical Technology Letters*, Vol. 20, January 1999.

[39] Huang and A. Feria, "Inflatable microstrip reflectarray antennas at X and Ka-band frequencies", IEEE *Antennas and Propagation Symposium,* Vol. 3, pp. 1670-1673, July 1999.

[40] F. Arpin, J. Shaker and D.A. McNamara, "Multi-feed single-beam power-combining reflectarray antenna", *Electronics Letters*, Vol. 40, No. 17, pp. 1035-1037, August 2004.

[41] M.E. Bialkowski, A.W. Robinson and H.J. Song, "Design, development and testing of X-band amplifying reflectarrays", *IEEE Transactions on Antenna and Propagation*, Vol. 50, No. 8, pp. 1065-1076, May 2002.

[42] S.V Hum and M. Okoniewski, "An electronically tunable reflectarray using varactor-dodid-tuned elements", IEEE *Antennas and Propagation Society Symposium,* Vol. 2, pp. 1827-1830, June 2004.

[43] M. Riel and J.J Laurin, "Design of an electronically beam scanning reflectarray using aperture-coupled elements", *IEEE Transactions on Antenna and propagation*, Vol. 55, No. 5, May 2007

[44] S.V Hum, G. McFeetors and M. Okoniewski, "A reflectarray cell based on a tunable MEMES capacitor", IEEE *Antennas and Propagation Society Symposium/URSI,* Vol. 2, pp. 1827-1830, July 2006.

[45] M. Arrebola, W. Hu, J.A.Encinar, R. Cahill, R. Dickie, V. Fusco, H. Gamble, Y.Álvarez and F.Las-Heras, "Experimental validation of a 94 GHz dual reflector antenna with a sub-reflectarray", *ESA Antenna Workshop*, Netherlands, May 2009

[46] D. Pilz and W. Menzel, "Folded reflectarray antenna", *Electronics Letters*, Vol. 34, No. 17, pp. 832-833, April 1998.

[47] W. Menzel, R. Leberer, "Folded reflectarray antennas for shaped beam applications", *Proc. 1st European Conf. Antennas Propagat. (EuCAP'2006)*, cpp.1-6c, cNov.2006.

[48] Y. Tarn, Y.S. Wang, and S.J Chung, "A dual-mode millimeter-wave folded microstrip reflectarray antenna", *IEEE Transactions on Antenna and Propagation*, Vol. 56, No. 6, June 2008.

[49] W. Menzel, D. Kessler, "A folded reflectarray antenna for 2D scanning", *German Microwave Conference*, pp. 1-4, March 2009.

[50] W. Menzel, J. Li, S. Dieter, "Folded reflectarray antenna based on a single layer reflector with increased phase angle range", *Proc. 3rd European Conf. Antennas Propagat. (EuCAP'2009)*, pp.2757-2760, March 2009.

[51] H. Kamoda, T. Iwasaki, J. Tsumochi and T. Kuki, "60-GHz electrically reconfigurable reflectarray using p-i-n diode", *IEEE International Microwave Symposium*, pp. 1177-1180, June 2009.

[52] W. Hu, , M.Y. Ismail, R.Cahill, H.S. Gamble, R. Dickie, V.F. Fusco, D. Linton, S.P. Rea and N. Grant, N, "Tunable liquid crystal reflectarray patch element" *Electronics Letters*, Vol. 42, No. 7, pp. 509-511, April 2006.

[53] R. Marin, A. Moessinger, F. Goelden, S. Mueller, and R. Jakoby, "77 GHz reconfigurable reflectarray with nematic liquid crystal", *Proc. 2nd European Conf. Antennas Propag. (EuCAP'2007)*, pp. 1-5, UK, Nov 2007

[54] J.P. Gianvittorio and Y.Rahmat-Samii "Reconfigurable patch antennas for steerable reflectarray applications", *IEEE Transactions on Antenna and Propagation*, Vol. 54, No. 5, May 2006.

[55] H. Rajagopalan, Y.Rahmat-Samii, and W.A. Imbriale, "RF MEMS actuated reconfigurable reflectarray patch-slot element", *IEEE Transactions on Antenna and Propagation*, Vol. 56, No. 12, December 2008.

[56] H. Salti, E. Fourn, R. Gillard, H. Legay and H. Aubert, "MEMS breakdown effects on the radiation of a MEMS based reconfigurable reflectarray", *Proc. 3rd European Conf. Antennas Propagat. (EuCAP'2009)*, pp.2757-2760, March 2009.

[57] M. R. Chaharmir, J. Shaker, M. Cuhaci, and A.R. Sebak, "Novel photonically-controlled reflectarray antenna", *IEEE Transactions on Antenna and Propagation*, Vol. 54, No. 4, April 2006.

[58] X. Shenheng, H. Rajagopalan, Y.Rahmat-Samii and W.A. Imbriale, "A novel reflector surface distortion compensating technique using a sub-reflectarray", IEEE *Antennas and Propagation Symposium,* pp.5315-5318, June 2007.

[59] M. Arrebola, L. de Haro and J. A. Encinar, "Analysis of a cassegrain antenna with a reflectarray as subreflector", *29th ESA Antenna Workshop on Multiple Beams and Reconfigurable Antennas, ESA-ESTEC,* Netherlands, 18-20 April 2007

[60] C.Tienda, M.Arrebola, J.A.Encinar, G.Toso and C.Mangenot, "Analysis of a dual-reflectarray antenna", *ESA antenna workshop*, Netherlands, May 2009.

[61] X.Shenheng and Y.Rahmat-Samii, "Sub-reflectarrays for spherical aberration compensation: concept and simulations", IEEE *Antennas and Propagation Symposium,*pp.1-4, July 2008.

[62] Y.Rahmat-Samii and S.W.Lee, "Directivity of planar array feeds for satellite reflector applications", *IEEE Transactions on Antenna and Propagation*, Vol.31, No.3, pp.463-470, May 1983.

[63] K.Hirasawa and M.Haneishi, Analysis, Design and Measurement of Small and Low-Profile Antennas, Norwood, MA : Artech House, 1992.

[64] Code CST Microwave Studio, SONNET High Frequency Electromagnetic Software Company, USA (www.sonnetsoftware.com).

[65] Code GRASP9-SE, TICRA Engineering Consultants, Denmark (www.ticra.com).

[66] W .V. T. Rusch, "Scattering from a hyperboloidal reflector in a cassegrainian feed system", *IEEE Transactions on Antenna and Propagation*, Vol.11, No.4, pp.414-421, July 1963.

CHAPTER 3

Sub-Reflectarrays Phase Equations Derivation and Electromagnetic Modelling of a Two-Dimensional Sub-Reflectarray : Integral Equation-Moment Method Formulation

3.1 Preliminary Remarks

In this chapter new pieces of work will be presented; the derivation of the sub-reflectarray design equations and an electromagnetic model of a two dimensional (2D) sub-reflectarray using an integral equation moment method formulation.

In Section 3.2 the sub-reflectarray design equations will be derived and explained. Two design equations will be derived. One gives compensating correction phase factors to emulate a hyperbolic sub-reflector using sub-reflectarray, and another gives compensating correction phase factors to emulate an ellipsoidal sub-reflector using a sub-reflectarray. These two design equations have not been derived or described elsewhere in the literature. Section 3.2 will start by giving a brief description of the radiation characteristics of dual antenna system sub-reflectors. Both the hyperbolic sub-reflector and the ellipsoidal sub-reflector are considered, leading to the derivation of their equivalent sub-reflectarray design equations. This will facilitate the understanding of all functions to be achieved by emulating the sub-reflectors using sub-reflectarrays.

In Section 3.3 a computational electromagnetics approach is described that will be used to model 2D sub-reflectarrays. The required 2D integral equation formulation is described. Motivation for adopting this approach is presented as well. Coupled integral equations are obtained for the 2D equivalent currents that model the structure; this is done using the physical boundary conditions and the surface equivalence theorem. The method of moments with pulse expansion functions and Dirac delta weighting functions is used to solve these integral equations. Expressions for the elements of the moment method impedance and excitation matrix are provided. A FORTRAN code is developed to implement the moment method formulation, and to use the resulting equivalent currents to obtain the near- and far-zone fields.

3.2 Sub-Reflectarray Phase Equations Derivations

3.2.1 Ellipsoidal and Hyperbolic Subreflector Geometrical Properties

As we mentioned in Chapter 2, a dual reflector antenna configuration that uses a sub-reflectarray as a subreflector has a number of other advantages compared with a conventional dual reflector antenna. This includes the important possibility of beam shaping, reconfiguring and scanning by adjusting the phase on the sub-reflectarray. It will be worthwhile review ideas about the conventional subreflector characteristics before deriving the phase equations of the equivalent sub-reflectarrays. Figure 3.1 shows the two conventional dual reflector antenna systems, the Cassegrain and the Gregorian dual reflector antennas, respectively.

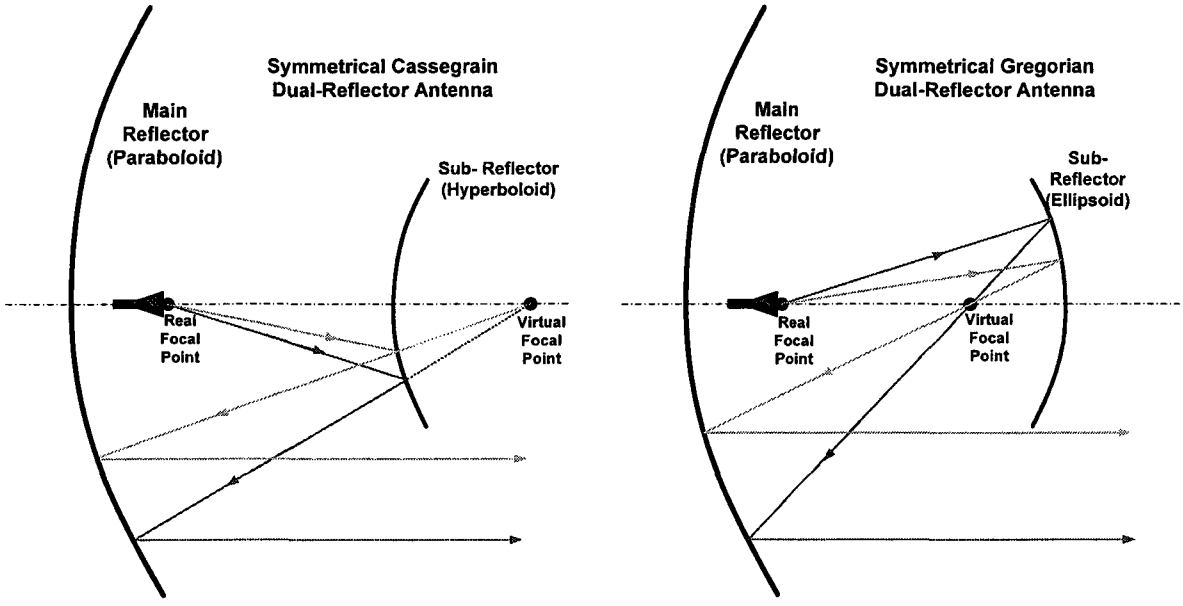

Figure 3.1- (a) Symmetrical Cassegrain Dual-Reflector, (b) Symmetrical Gregorian Dual-Reflector

In the Cassegrian dual reflector Fig.3.1(a) the sub-reflector is a hyperboloid whereas in the Gregorian case Fig.3.1(b) it is an ellipsoid. The feed-horn in both cases must be situated in a way that ensures coincidence between its phase center and the real focal

point of the subreflector. This is very important to avoid introducing phase error at the parabolic reflector surface, which degrades the over all system performance (e.g. directivity, side lobe level). Each subreflector has two foci, a real focal point and a virtual focal point. The virtual focal point is the phase center of all waves that are reflected from the subreflector to illuminate the parent parabolic reflector. Hence we see in the hyperboloid case the extensions of all rays (based on ray tracing) converge at the virtual focal point, and in the ellipsoidal subreflector all the scattered rays pass through its virtual focal point. Consequently in the calculation of any subreflector far-field phase pattern, all calculations must be referenced to the virtual focal point to be able to study the phase distribution over the parent reflector surface. Since the feed-horn radiates waves with spherical phase fronts, the scattered waves from the sub-reflectors have spherical wave fronts as long as the virtual focal point is taken to be the phase center of these scattered waves. Figure 3.2 shows how ellipsoidal and hyperbolic sub-reflectors preserve the spherical phase front property of the scattered waves.

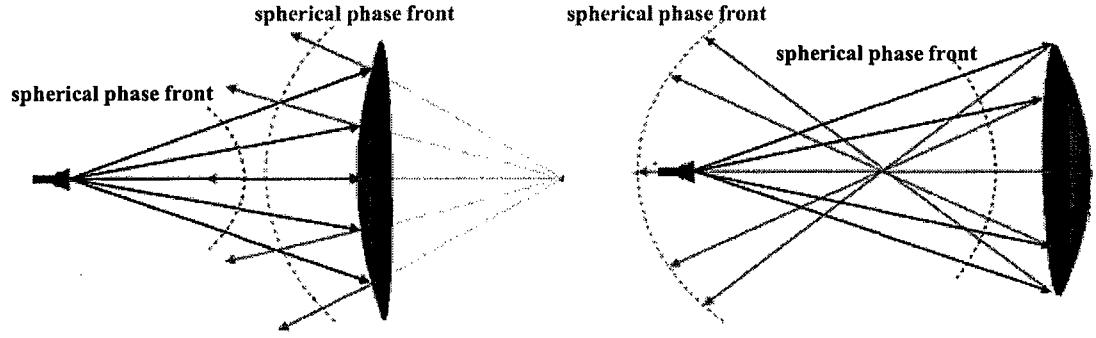

Figure 3.2- (a) Scattering from Hyperboloid, (b) Scattering from Ellipsoid

It is also evident from Figure 3.2 that any sub-reflectarray which must emulate either an ellipsoidal or a hyperboloidal subreflector should maintain such phase front conversion in order to provide the same radiation characteristics. It is worth mentioning that the subreflectors perform the same phase front conversion either in the transmit or in the receive mode; the phase fronts are always spherical in both the transmit and the receive modes. On the contrary, the parent parabolic reflector converts the spherical

phase front of the feed or the subreflector to a planar phase front (plane wave) in the transmit mode to form the desirable narrow main beam in a specific direction in space. It does the converse in the receive mode, as shown in Figure 3.3

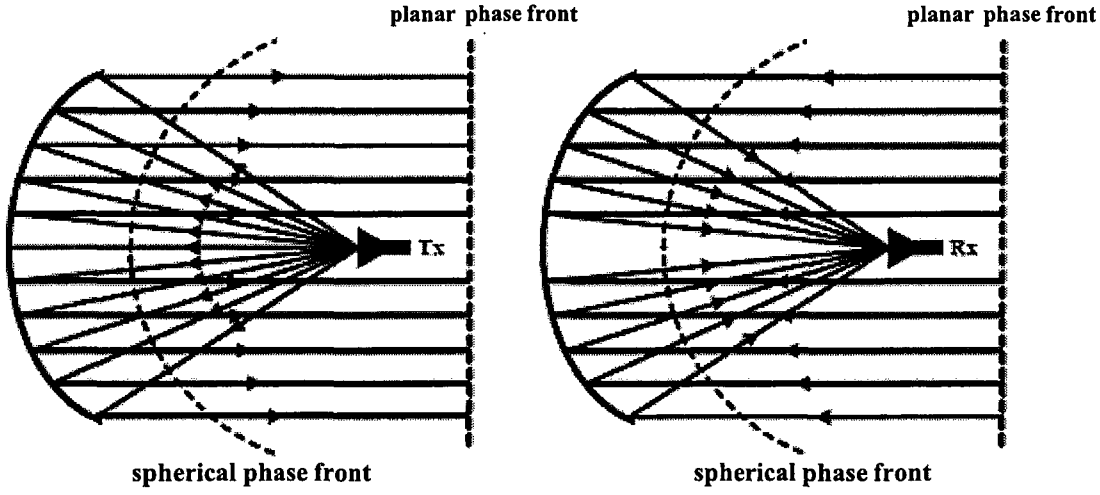

Figure 3.3- Scattering from parabolic reflector both transmit and receive mode. (After [1])

The radiation characteristics or the optical focusing characteristics of traditional curved reflectors differ based on their degree of curvature. They are generated by rotating or translating conic sections [2]. Analytically the degree of curvature of any reflecting surface that is generated from a conic section (e.g. spherical, parabolic, ellipsoidal hyperbolic) is related to a parameter that is called the eccentricity of the reflector. "It is a measure of the off-centeredness of the focal points for a given focal lengths" [2]. Thus for a spherical reflector it equals zero because the foci are at the center of the sphere. For a parabolic reflector the eccentricity equals 1 since the foci are infinitely far apart. For the hyperbolic and ellipsoidal reflectors we have a specific finite distance between the foci (the real and virtual focal points). This distance can be changed over a typical range to control the radiation characteristics of the subreflectors. A change of the distance between the foci means a change of eccentricity (e). The eccentricity value range for a hyperbolic reflector is $1 < e < \infty$, and for an ellipsoidal reflector is $0 < e < 1$ [2]. This gives a wide degree of freedom in designing subreflectors and consequently their equivalent sub-reflectarrays, since we can widen and narrow the angular range in space

(which is centered at the virtual focal point) over which we want to illuminate the parent reflector with a specified edge taper by changing the eccentricity of the sub-reflector. Another degree of freedom appears when we change the eccentricity and *F/D* ratio of the dual reflector system to compact the physical size or to optimize the performance of the antenna.

Figure 3.4 and Figure 3.5 show the design parameters of a hyperbolic sub-reflector (or its equivalent sub-reflectarray) and an ellipsoidal subreflector (or its equivalent sub-reflectarray) respectively. The eccentricity in both cases is the ratio *f/a*. For a hyperbolic profile *f* is the half distance between the foci. Quantity *a* is the half distance between the hyperboloid and its image surface. All distances in the figures are measured along the z axis. For the ellipsoid *f* is the half distance between the foci, and *a* is half the major axis length of the generating ellipse [2]. It is worth mentioning that *f* is always greater than *a* for a hyperboloid, and that the opposite is true for the ellipsoid. The eccentricity can be written in terms of the virtual and real focal lengths F_V and F_R, respectively, as indicated in Figures 3.4 and 3.5.

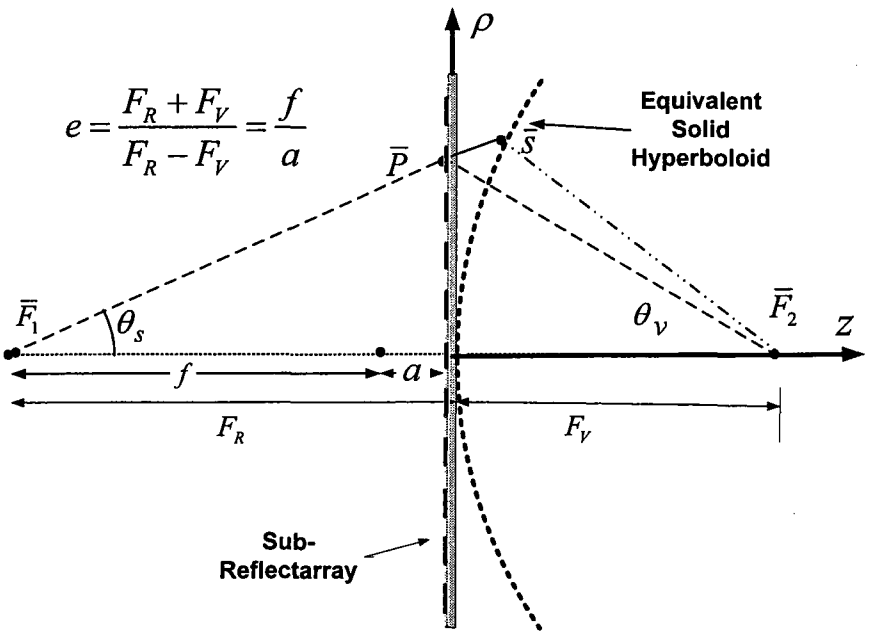

Figure 3.4- Hyperboloid and its equivalent sub-reflectarray design parameters

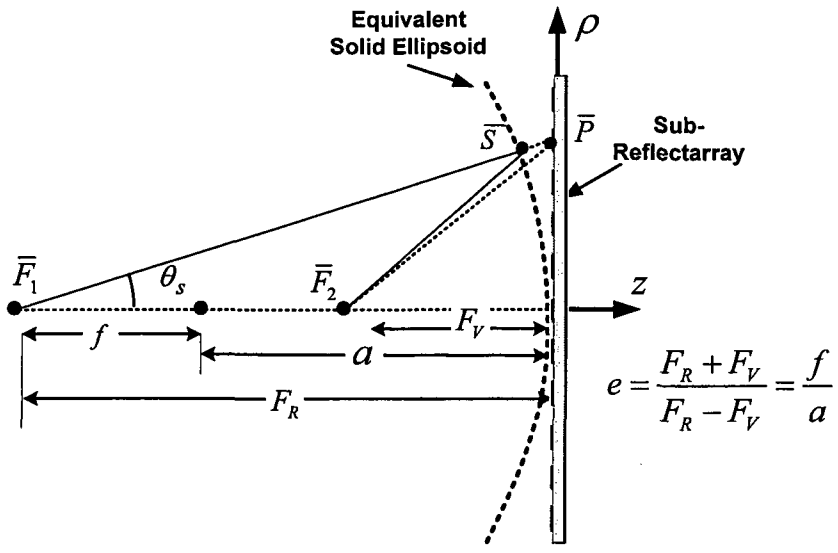

Figure 3.5- Ellipsoid and its equivalent sub-reflectarray design parameters

3.2.2 Derivation of Phase Design Equation for a Reflectarray that Emulates a Paraboloidal Reflector.

The phase-shift that must be defined at each element of a reflectarray to emulate a parabolic reflector is derived in this section. This design equation is given in [3] and elsewhere. We discuss the derivation here to explore the associated reasoning. Similar derivations (albeit with some novel reasoning being required) that are not available elsewhere will performed in Sections 3.2.3 and 3.2.4 for sub-reflectarrays. Figure 3.6 shows the coordinate used to derive the parabolic phase equation, where ρ is the radial coordinate in the xy-plane, $\bar{P}$ is the location of the n-th with $z_n = 0$, $\bar{S}$ is the reflection point of a ray emanating from the feed, on the parabolic reflector surface. Each element of the reflectarray must provide a correction phase ψ_n that makes the phase of the reflected rays from the reflectarray over a planar aperture equal to the phase of the reflected rays from parabolic reflector over the same aperture. As an example of that consider the rays reflected from the n-th patch and the parabolic reflector at points $\bar{P}$ and $\bar{S}$ respectively. To get same phase over aperture D the phase equation

$$-kR_n + \psi_n - kH = -kt_n - kh_n \tag{3-1}$$

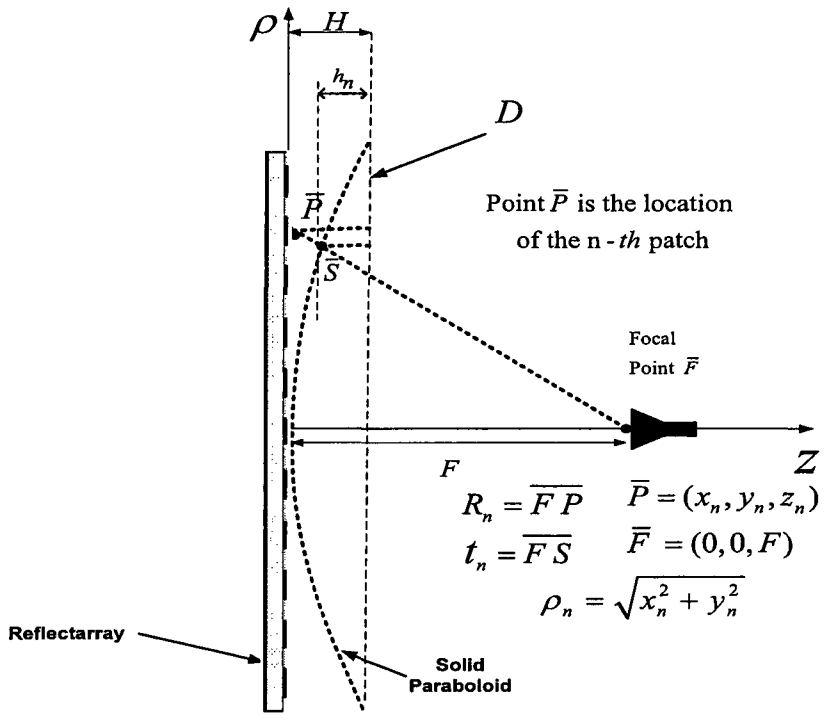

Figure 3.6- Replacement of parabolic reflector by an equivalent reflectarray.

must be satisfied. In expression (3-1) R_n is the distance between the phase center of the feed and the center of the n-th patch (point $\bar{P}$), t_n is the distance between the phase center of the feed and the reflection point $\bar{S}$ on the parabolic reflector surface, and $k = 2\pi / \lambda_0$ is the free space wavenumber. The correction phase at the n-th patch can be found from equation (3-1) to be

$$\psi_n = kR_n - \underbrace{k(t_n + h_n)}_{\substack{\text{This is a Constant for a Given Paraboloid}}} + \underbrace{kH}_{\substack{\text{This is an Arbitary Constant}}} \tag{3-2}$$

Since H is constant for all reflectarray elements, and $t_n + h_n$ is constant by definition of the paraboloid geometry, ψ_n can be rewritten as

$$\psi_n = kR_n \pm 2\pi N \tag{3-3}$$

Equation (3-3) is the design phase equation that has been presented by Pozar [3]. Quantity $\pm 2\pi N$ is a constant added to fix the phase delay contour to a realizable value. Phase equation (3-3) is a special case of phase equation (2-8) where the compensating phase of all patches produce a collimated beam in the broadside direction. To get the beam directed in any direction in space similar steps can be used to derive (2-8) using Figure 2.17.

3.2.3 Derivation of Phase Design Equation for a Sub-Reflectarray that Emulates a Hyperboloidal Subreflector

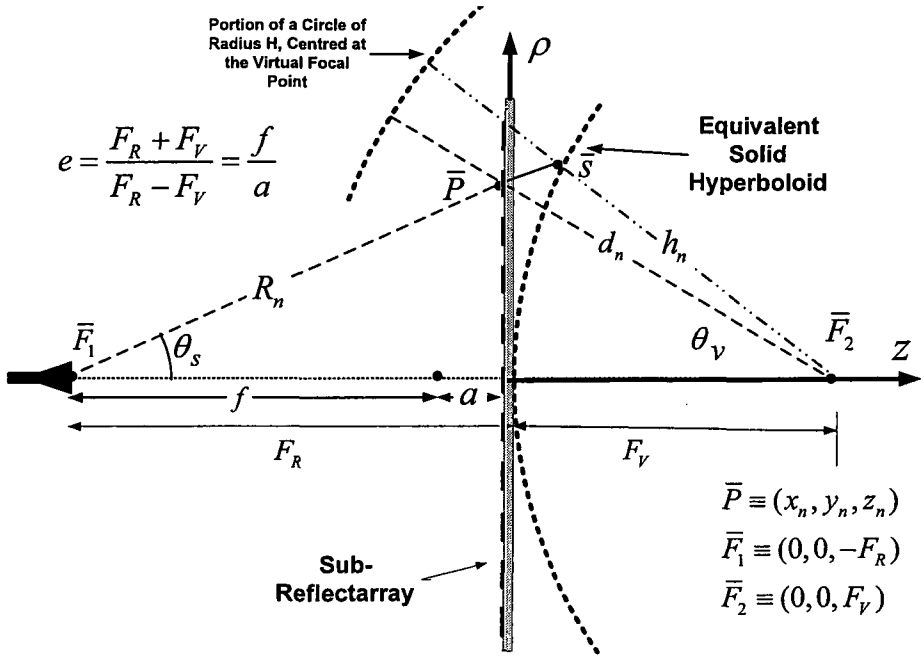

Figure 3.7- Replacement of a hyperboloidal subreflector by an equivalent sub-reflectarray.

The phase-shift that must be defined at each element of a sub-reflectarray to emulate a hyperboloidal subreflector is derived here for the first time. As we mentioned earlier in this chapter, and based on Figure 3.7 shown before, the sub-reflectarray should be

designed to reflect the incident rays from the feed as if emanating from the virtual focal point $\overline{F}_2$. In this way the spherical phase front of the incident and the reflected waves is maintained. This can be accomplished by recognizing the virtual focal point of the hyperbolic reflector as the phase center of the reflected waves, and hence all reflected rays from both the sub-reflectarray and the hyperboloid will have the same phase over a circle centered at this virtual focal point. To achieve this, the n-th patch dimensions must be selected to give a correction phase ψ_n that satisfies

$$-kR_n + \psi_n - k(H - d_n) = -kt_n - k(H - h_n) \tag{3-4}$$

In expression (3-4), R_n is the distance between the feed phase center and point $\overline{P}$, which is the point (x_n, y_n) at the center of the n-th-patch. Symbol d_n is the distance between the hyperboloid virtual focal point and point $\overline{P}$, t_n is the distance between the feed phase center and the reflection point $\overline{S}$ on the sub-reflector surface, h_n is the distance between the hyperboloid virtual focal point and point $\overline{S}$, k is the free space wavenumber and H is the radius of a circle centered at the virtual focal point of the hyperboloid. Since H is the same constant on both sides of (3-4), the correction phase ψ_n at the n-th patch can be expressed as

$$\psi_n = k(R_n - d_n) - k\underbrace{(t_n - h_n)}_{\substack{\text{This is a} \\ \text{Constant} \\ \text{for a Given} \\ \text{Eccentricity}}} \tag{3-5}$$

By definition of the hyperboloidal geometry, quantity $t_n - h_n$ is a constant and so equation (3-5) can be rewritten as

$$\psi_n = k(R_n - d_n) \pm 2\pi N \tag{3-6}$$

From Figure 3.7 one might end up with two different angular ranges θ_V s over which the main parabolic reflector could be illuminated. This is not a problem at all since we can adjust this angular range based upon the *F/D* of the parent reflector and the eccentricity of the subreflector. Moreover one could select the angular range of interest and then sub-reflectarray can be designed accordingly. An altarnative configuration that can be used as a starting point in the derivation of the phase equation given in equation (3-6) is shown in Figure 3.8. It ensures identical illuminating angular ranges of both the sub-reflector and its equivalent sub-reflectarray, and even identical point on the circle that is centered at the virtual focal point $\overline{F}_2$. One arrives at the same phase equation either way.

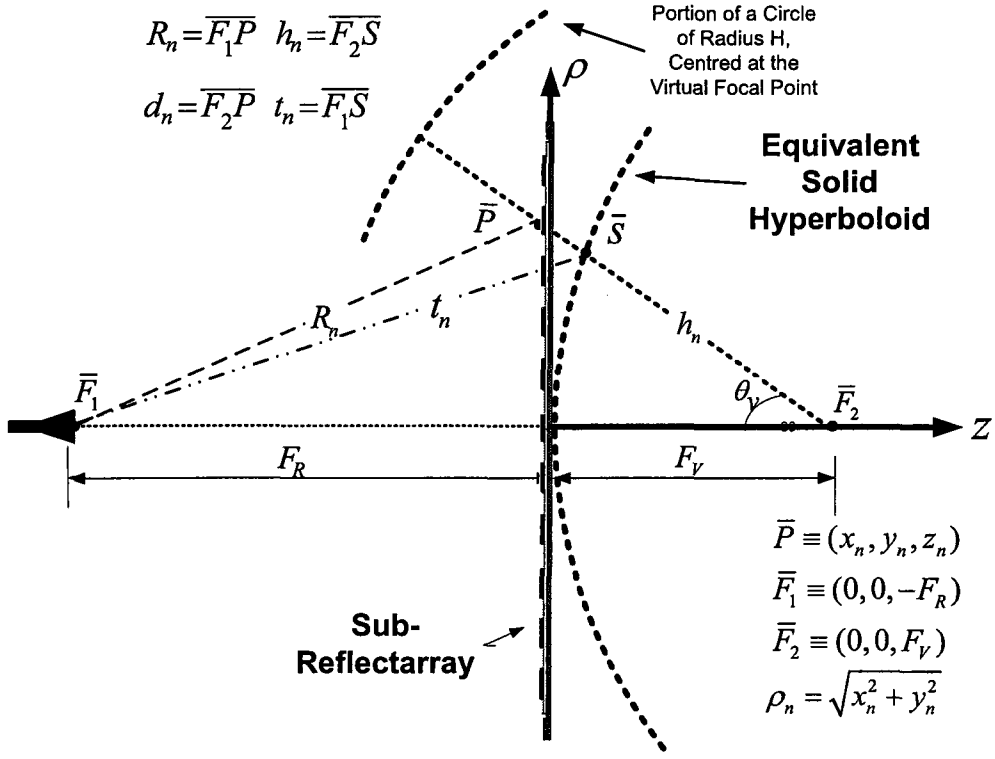

Figure 3.8- Replacement of hyperboloidal subreflector by an equivalent sub-reflectarray, version two.

From Figure 3.8 it is apparent that the amplitude taper of the feed is not the same at the edge of the sub-reflector and at the edge of its equivalent sub-reflectarray. In reality the difference is not big and a lower edge taper at the edge of the sub-reflectarray does

not affect the radiation characteristics considerably since the order of edge taper is very low, as we mentioned in Chapter 2, being typically about -18dB.

3.2.4 Derivation of the Phase Design Equation for a Sub-Reflectarray that Emulates an Ellipsoidal Subreflector

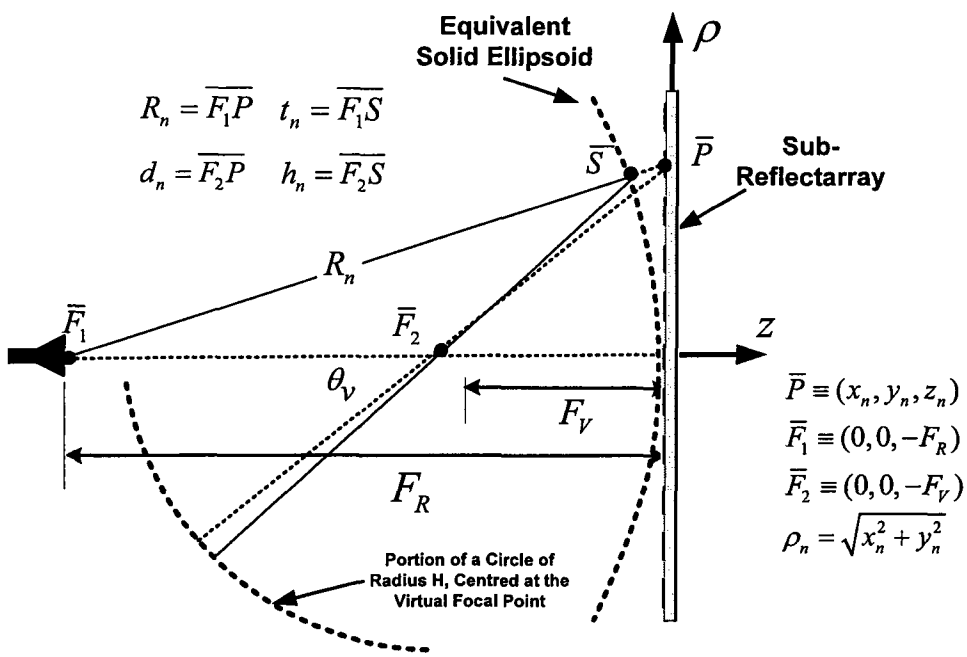

Figure 3.9- Replacement of ellipsoidal subreflector by an equivalent sub-reflectarray.

The phase-shift that must be defined at each element of a sub-reflectarray to emulate an ellipsoidal subreflector is derived in this section. The overall procedure is similar to what presented in the previous section. Figure 3.7 shows the ellipsoidal subreflector and its equivalent sub-reflectarray. The sub-reflectarray patch dimensions should be designed to reflect the incident rays from the feed in such a way that they converge through the virtual focal point prior to re-emerging and spreading out over the illuminating angular range of interest. In this way the spherical phase front requirement of the incident and the reflected waves is maintained. This can be accomplished by conjecturing that since the virtual focal point of the ellipsoidal reflector is the phase center of the reflected waves; all

reflected rays from both the sub-reflectarray and the original ellipsoid must have the same phase over a circle centered at this virtual focal point. To achieve this, the n-th patch dimensions must be selected to give a correction phase ψ_n that satisfies the equation

$$-kR_n + \psi_n - kd_n - kH = -kt_n - kh_n - kH \tag{3-7}$$

where R_n is the distance between the feed phase center and point $\overline{P}$, which is the center (x_n, y_n) coordinate of the n-th patch, d_n is the distance between the ellipsoid virtual focal point and point $\overline{P}$, t_n is the distance between the feed phase center and the reflection point $\overline{S}$ on the subreflector surface, h_n is the distance between the ellipsoid virtual focal point and point $\overline{S}$, k is the free space wavenumber and H is the radius of a circle centered at the virtual focal point of the ellipsoid. Quantity H has the same value on both sides of (3-7), and so the correction phase ψ_n at the n-th patch can be found from (3-7) to be

$$\psi_n = k(R_n + d_n) - k\underbrace{(t_n + h_n)}_{\substack{\text{This is a} \\ \text{Constant} \\ \text{for a Given} \\ \text{Eccentricity}}} \tag{3-8}$$

By definition of the ellipsoidal geometry, quantity $t_n + h_n$ is a constant and so equation (3-8) can be rewritten as

$$\psi_n = k(R_n + d_n) \pm 2\pi N \tag{3-9}$$

Similar to the derivation of the hyperboloidal sub-reflectarray design equation we discussed in Section 3.2.3, we can use a second configuration, this time shown in Figure 3.10, to end up with design equation (3-9).

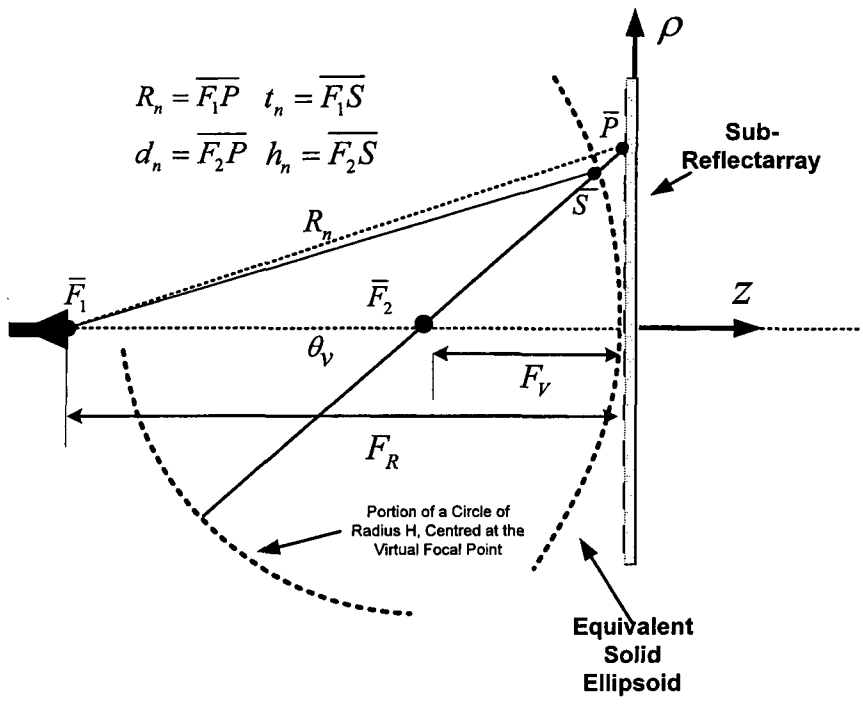

Figure 3.10- Replacement of ellipsoidal subreflector by an equivalent sub-reflectarray, version two.

3.2.5 Further Comments on the Sub-Reflectarray Design Equations

It is clear based on equations (3-6) and (3-9), that there is actually no need to refer to the solid subreflectors each time we want to design sub-reflectarrays. The terms in the two design equations have meaning without having to be solid subreflectors parameters. All features of solid subreflecators like changing the eccentricity to control the radiation patterns, can be accomplished by changing the virtual foci locations F_R and F_V, which leads to the change of R_n and d_n and a change in the element phasing requirement. Nevertheless some examples will be presented in Chapter 4 to show the correspondence between solid subreflectors and their equivalent sub-reflectarrays.

3.3 Two-Dimensional Sub-Reflectarray Integral Equation-Moment Method Formulation

3.3.1 Motivation for Using Two-Dimensional Electromagnetic Models

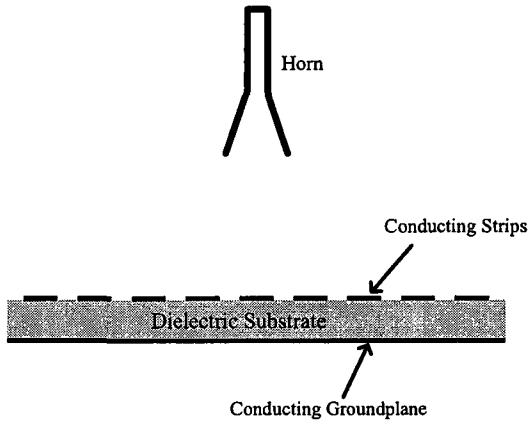

Figure 3.11- Two-Dimensional Sub-Reflectarray Antenna

As stated in Section 2.2.3, we wish to perform an electromagnetic analysis of sub-reflectarrays in sufficient detail that we are able to examine many different aspects: the location of foci and their shifting with a change in frequency; the effect of feed blockage; the far-zone amplitude and phase radiation patterns. It is computationally very demanding (even with present-day computers) to perform such computations using an electromagnetic model of a fully 3-dimensional sub-reflectarray since it is electrically large and dielectrically inhomogeneous. This is especially so if one remembers that we wish to perform trade-off studies, which will require many simulations. We study and model a two-dimensional (2D) sub-reflectarray instead.

The 2D sub-reflectarray is sketched in Figure 3.11, and to this we apply a 2D integral equation formulation, consisting of a magnetic line source that illuminates a

structure consisting of conducting strips, dielectric material and conducting groundplane[1]. In this way it is possible to model the sub-reflectarray's feed-horn, the sub-reflectarray proper, and its interaction with the feedhorn. The electric field lies entirely within the plane of the page, and is thus perpendicular to the conducting strips that form the (in this case two-dimensional) elements of the sub-reflectarray. In the parlance of two-dimensional moment method formulations this is a TE_z case. We have used the integral equation formulation described in [4] as the basis of our formulation, but have extended it so as to be able to accommodate more than just a single dielectric object partially covered by conductors. This extension is described in Section 3.3.2. The resulting additional moment method matrix and excitation matrix terms are provided in Section 3.3.3.

3.3.2 Derivation of the Integral Equation

The horn antenna is modeled by an infinitely long magnetic line source plus conducting walls. The incident field from this line source (i.e. the impressed field) excites the wall surface of the horn, the dielectric slab and the conducting strips, resulting in scattered fields. These scattered fields are considered to be produced by equivalent magnetic currents (an "internal' current density and an "external" current density [4]) on these surfaces. The external total field is the sum of the incident field and the scattered field (due to the external equivalent current density) outside the dielectric. The internal total field is due to the internal equivalent current density. Boundary conditions for the continuity of tangential electric and magnetic fields along the dielectric surface, and zero tangential electric fields on the conducting strips and horn walls, are used in obtaining the integral equations. Application of the method of moments results in a matrix equation. Pulse expansion functions and point matching weighting functions are used in the moment method formulation. This matrix equation is solved to obtain the internal and external equivalent currents, from which the all the fields of the antenna (both near-fields and far-fields) can be calculated.

[1] In the formulation the conducting groundplane need not be treated separately from the strips on the top surface of the substrate. It is simply considered to be a very wide strip, albeit located on the lower surface of the substrate.

Initially we consider the problem of electromagnetic scattering due to a single dielectric slab and conducting strips (with the horn absent) as described in [4]. The solution to this problem is given in [4] for the TE_z case. The scattered field in this case is actually generated by the conduction currents on the strips and the polarization currents in the dielectric. The surface equivalence theorem is used to formulate the problem in terms of equivalent magnetic current sources on the dielectric surface C_d and conducting strips surface C_s. Surfaces C_d and C_s are shown in Figure 3.12.

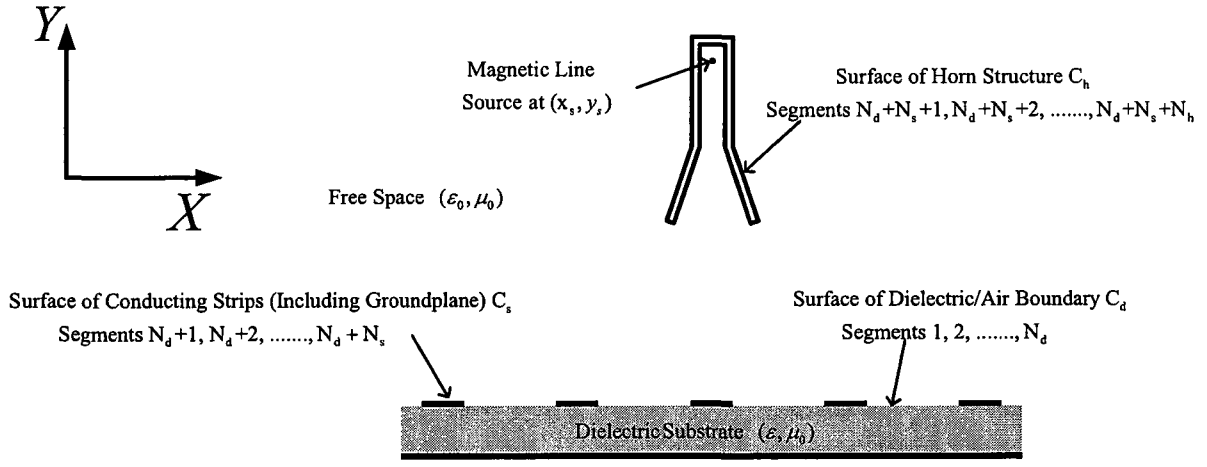

Figure 3.12-Segmentation of the model of the 2D sub-reflectarray antenna

The magnetic field internal to the dielectric can be considered to be produced by an equivalent ("internal") magnetic current source $\hat{z}\, f(\bar{\rho}')$ on C_d and C_s, radiating into the homogenous space filled with dielectric permittivity ε everywhere and given by [4]

$$H_z^{\text{int}}(\hat{z}\, f) = \frac{-k}{4\eta} \int_{C_d+C_s} f(\underline{\rho}') H_o^{(2)}(k|\bar{\rho} - \bar{\rho}'|) dt' \qquad (3\text{-}10)$$

where $k = \omega\sqrt{\mu_o \varepsilon}$ is the wave number in the dielectric of permittivity ε, $\eta = \sqrt{\mu_o / \varepsilon}$ is the intrinsic impedance of the dielectric, $\bar{\rho} = x\hat{x} + y\hat{y}$ is the observation point vector,

$\bar{\rho}' = x'\hat{x} + y'\hat{y}$ is the source point vector, and $H_o^{(2)}$ is the Hankel function of the second kind and zero order. Appendix A can be consulted for details of the vector coordinate system employed. The magnetic field external to the dielectric can be considered as being the sum of the incident field due to the impressed line source plus a scattered field due to an equivalent ("external") magnetic current source $\hat{z}\,g(\bar{\rho}')$ on C_d and C_s, and can be written as [4]

$$H_z^s(\hat{z}\,g) = \frac{-k_o}{4\eta_o} \int_{C_d+C_s} g(\bar{\rho}') H_o^{(2)}(k_o|\bar{\rho} - \bar{\rho}'|)dt' \tag{3-11}$$

On the dielectric surface the boundary conditions require continuity of the internal and external tangential electric and magnetic fields, as shown below in (3-12) and (3-13) respectively.

$$H_z^{\text{int}} = H_z^{ext} \qquad \text{over } C_d \tag{3-12}$$

$$\hat{n} \times \bar{E}^{\text{int}} = \hat{n} \times \bar{E}^{ext} \qquad \text{over } C_d \tag{3-13}$$

The tangential electric fields must be zero on the strips, as indicated in (3-14).

$$\hat{n} \times \bar{E}^{\text{int}} = \hat{n} \times \bar{E}^{ext} = 0 \qquad \text{over } C_s \tag{3-14}$$

Here $\hat{n}$ is a unit vector normal to the relevant boundary. The external magnetic field H_z^{ext} is the sum of the scattered field H_z^s due to the equivalent current sources, and the impressed field H_z^i due to the line source. This is of course also true for the external electric field $\underline{E}^{ext}$. Equations (3-12), (3-13) and (3-14) can thus be rewritten as

$$\hat{n} \times \left(\bar{E}^{\text{int}}(\hat{z}\,f) - \bar{E}^s(\hat{z}\,g)\right) = \hat{n} \times \bar{E}^i \qquad \textit{over } C_d \tag{3-15}$$

$$\hat{z}\left(H_z^{\text{int}}(\hat{z}\,f) - H_z^s(\hat{z}\,g)\right) = \hat{z}\,H_z^i \qquad \textit{over } C_d \tag{3-16}$$

$$\hat{n} \times \bar{E}^{\text{int}}(\hat{z}\,f) = 0 \qquad \textit{over } C_s \tag{3-17}$$

$$-\hat{n} \times \bar{E}^s(\hat{z}\,g) = \hat{n} \times \bar{E}^i \qquad \textit{over } C_s \tag{3-18}$$

and represent coupled integral equations for the two sets of unknown equivalent magnetic currents.

We can extend this formulation to include a second physically separate conducting object needed to model the walls of the horn antenna. When dealing with scatterers that are composed of both conducting and dielectric material this extension is not trivial. Even though the additional object (i.e. the horn walls) is composed of conducting material only, nevertheless two sets of equivalent electric currents must be used to model it in a manner consistent with that used for the dielectric object with the conducting strips. We let $\hat{z}\,b(\bar{\rho}')$ and $\hat{z}\,a(\bar{\rho}')$ represent the equivalent currents on the horn surface C_h; they contribute to both the internal and external fields respectively, namely

$$H_z^{\text{int}}(\hat{z}\,b) = \frac{-k}{4\eta}\int_{C_h} b(\bar{\rho}')H_o^{(2)}(k|\bar{\rho}-\bar{\rho}'|)dt' \qquad (3\text{-}19)$$

$$H_z^{s}(\hat{z}\,a) = \frac{-k_o}{4\eta_o}\int_{C_h} a(\bar{\rho}')H_o^{(2)}(k_o|\bar{\rho}-\bar{\rho}'|)dt' \qquad (3\text{-}20)$$

Application of the boundary conditions on all conducting surfaces and dielectric interfaces then yields the coupled integral equations of the extended formulation as

$$\hat{n}\times\left(\bar{E}^{\text{int}}(\hat{z}\,f)-\bar{E}^{s}(\hat{z}\,g)-\bar{E}^{s}(\hat{z}\,a)+\bar{E}^{\text{int}}(\hat{z}\,b)\right)=\hat{n}\times\bar{E}^{i} \quad \text{over } C_d \qquad (3\text{-}21)$$

$$\hat{z}\left(H_z^{\text{int}}(\hat{z}\,f)-H_z^{s}(\hat{z}\,g)-H_z^{s}(\hat{z}\,a)+H_z^{\text{int}}(\hat{z}\,b)\right)=\hat{z}\,H_z^{i} \quad \text{over } C_d \qquad (3\text{-}22)$$

$$\hat{n}\times\bar{E}^{\text{int}}(\hat{z}\,f)+\hat{n}\times\bar{E}^{\text{int}}(\hat{z}\,b)=0 \quad \text{over } C_s \text{ \& } C_h \qquad (3\text{-}23)$$

$$-\hat{n}\times\bar{E}^{s}(\hat{z}\,g)-\hat{n}\times\bar{E}^{s}(\hat{z}\,a)=\hat{n}\times\bar{E}^{i} \quad \text{over } C_s \text{ \& } C_h \qquad (3\text{-}24)$$

3.3.3 Formulation of the Moment Method Solution of the Extended Integral Equation Formulation

Pulse expansion functions are applied to the above coupled integral equations by dividing the surfaces C_d, C_s and C_h into N_d, N_s and N_h straight-line segments respectively,

as shown in Figure 3.12, and approximating the currents as constant over each segment. The equivalent currents thus take the forms

$$f = \sum_{j=1}^{N_d+N_s} f_j P_j \tag{3-25}$$

$$g = \sum_{j=1}^{N_d+N_s} g_j P_j \tag{3-26}$$

$$b = \sum_{j=1}^{N_h} b_j P_{j+N_d+N_s} \tag{3-27}$$

$$a = \sum_{j=1}^{N_h} a_j P_{j+N_d+N_s} \tag{3-28}$$

where

$$P_j = \begin{cases} 1 & t_1(j) \le t \le t_2(j) \\ 0 & elsewhere \end{cases} \tag{3-29}$$

P_j is a pulse expansion function with a value of 1 over the j^{th} segment. Quantities $t_1(j)$ and $t_2(j)$ are the starting and end points of the j^{th} segment, and t is the arc length along the straight line segments, as illustrated in Figure A-1 in Appendix A. Substituting (3-25) through (3-29) into (3-21) through (3-24), and multiplying both sides of (3-22) by η_o, yields the following intermediate expressions:

$$\sum_{j=1}^{N_d+N_s} f_j \hat{n}\times\bar{E}^{int}\left(\hat{z}P_j\right) + \sum_{j=1}^{N_d+N_s}\left(-g_j\right)\hat{n}\times\bar{E}^{s}\left(\hat{z}P_j\right) + \sum_{j=1}^{N_h}\left(-a_j\right)\hat{n}\times\bar{E}^{s}\left(\underline{u}_z P_{j+N_d+N_s}\right) + \sum_{j=1}^{N_h} b_j \hat{n}\times\bar{E}^{int}\left(\hat{z}P_{j+N_d+N_s}\right) = \hat{n}\times\bar{E}^{i} \quad \text{over } C_d \tag{3-30}$$

$$\eta_0 \sum_{j=1}^{N_d+N_s} \hat{z}\, f_j H_z^{int}\left(\hat{z}P_j\right) + \eta_0 \sum_{j=1}^{N_d+N_s} \hat{z}\left(-g_j\right) H_z^{s}\left(\hat{z}P_j\right) + \eta_0 \sum_{j=1}^{N_h} \hat{z}\left(-a_j\right) H_z^{s}\left(\hat{z}P_{j+N_d+N_s}\right) + \eta_0 \sum_{j=1}^{N_h} \hat{z}\, b_j H_z^{int}\left(\hat{z}P_{j+N_d+N_s}\right) = \eta_0 \hat{z} H_z^{i} \quad \text{over} C_d \tag{3-31}$$

$$\sum_{j=1}^{N_d+N_s} f_j\, \hat{n}\times\bar{E}^{\text{int}}\left(\hat{z}\,P_j\right)+\sum_{j=1}^{N_h} b_j\, \hat{n}\times\bar{E}^{\text{int}}\left(\hat{z}\,P_{j+N_d+N_s}\right)=0 \qquad \text{over } C_s \text{ and } C_h \qquad (3\text{-}32)$$

$$\sum_{j=1}^{N_d+N_s}\left(-g_j\right)\hat{n}\times\bar{E}^{s}\left(\hat{z}\,P_j\right)+\sum_{j=1}^{N_h}\left(-a_j\right)\hat{n}\times\bar{E}^{s}\left(\hat{z}\,P_{j+N_d+N_s}\right)=\hat{n}\times\bar{E}^{i} \qquad \text{over } C_s \text{ and } C_h \qquad (3\text{-}33)$$

The symmetric product of two vectors $\bar{A}$ and $\bar{B}$ on C is defined as

$$\left\langle \bar{A},\bar{B}\right\rangle=\int_C \bar{A}\cdot\bar{B}\,dc \qquad (3\text{-}34)$$

Taking the symmetric product of (3-30) through (3-33) with a set of weighting functions $\hat{z}W_i$, we reduce the integral equations (3-21) through (3-24) to the matrix equation

$$\begin{bmatrix} [Z_1^{\text{int}}] & [Z_1^s] & [Z_1^a] & [Z_1^b] \\ [Y^{\text{int}}] & [Y^s] & [Y^a] & [Y^b] \\ [Z_2^{\text{int}}] & [0] & [0] & [Z_2^b] \\ [0] & [Z_2^s] & [Z_2^a] & [0] \end{bmatrix}\begin{bmatrix} [I^f] \\ [-I^g] \\ [-I^a] \\ [I^b] \end{bmatrix}=\begin{bmatrix} [V_1] \\ [I] \\ [0] \\ [V_2] \end{bmatrix} \qquad (3\text{-}35)$$

The j^{th} element of the column vectors $[I_f]$, $[-I_g]$, $[-I_a]$ and $[I_b]$ in (3-35) are the unknown currents f_j, $-g_j$, $-a_j$ and b_j respectively, and are found by solving the above matrix equation. The excitation vector on the right hand side of the equation consists of elements due to the incident electric and magnetic fields from the magnetic line source. We can write

$$[I]=\begin{bmatrix} [I_1] \\ \\ [I_2] \end{bmatrix} \qquad (3\text{-}36)$$

where $[I_1]$ and $[I_2]$ are column vectors of size N_d and N_s+N_h respectively. The elements of $[I]$ are found from (3-30) and (3-33) to be

$$I_i = \eta_0 \left\langle \hat{z} W_i, \hat{z} H_z^i \right\rangle \tag{3-37}$$

The weighting function W_i is chosen to be the Dirac delta-function $\delta\left(t - \frac{t_1(i)+t_2(i)}{2}\right)$ which is zero everywhere except at the center of the i^{th} segment. The subscript i of the function $\hat{z}W_i$ runs from i=1 to i=N_d over the dielectric surface for (3-30) and (3-31), whereas for (3-32) and (3-33) the i values run from N_d+1 to N_d+N_s+N_h over the horn and strips. Substituting the expression for H_z^i from (B-1) of Appendix B, and W_i into (3-37), we obtain

$$I_i = -\frac{k_o}{4} H_0^{(2)}\left(k_o \sqrt{\left(x_c(i)-x_o\right)^2 + \left(y_c(i)-y_o\right)^2} \right) \tag{3-38}$$

where $(x_c(i),y_c(i))$ are the center points of the i^{th} segment (as defined in Appendix A) and (x_o,y_o) are the coordinates of the line source. Column vector $[V]$ is a vector of length N_d and is expressed as

$$V_i = \left\langle \hat{z} W_i, \hat{n} \times \bar{E}^i \right\rangle \tag{3-39}$$

Performing the vector cross multiplication of the magnetic field $\bar{E}^i$ due to the line source, which is derived in (B-6) and (B-7) of Appendix B, with the normal $\hat{n}$ of the i^{th} segment defined in (A-3) in Appendix A, allows us to write

$$V_i = \left\{ -t_y E_y^i(x_c(i), y_c(i)) - t_x E_x^i(x_c(i), y_c(i)) \right\} \tag{3-40a}$$

with

$$E_x^i(x_c(i), y_c(i)) = \frac{k_o^2}{4j}\left(y_c(i)-y_o\right) \frac{H_1^{(2)}\left\{ k_o \sqrt{(x_c(i)-x_o)^2 + (y_c(i)-y_o)^2} \right\}}{k_o \sqrt{(x_c(i)-x_o)^2 + (y_c(i)-y_o)^2}} \tag{3-40b}$$

$$E_y^i(x_c(i),y_c(i)) = -\frac{k_o^2}{4j}(x_c(i)-x_o)\frac{H_1^{(2)}\left\{k_o\sqrt{(x_c(i)-x_o)^2+(y_c(i)-y_o)^2}\right\}}{k_o\sqrt{(x_c(i)-x_o)^2+(y_c(i)-y_o)^2}} \qquad (3\text{-}40c)$$

Quantities t_x and t_y are the x and y components, respectively, of the unit vector $\underline{t}_i$ along the i^{th} segment, which is derived in (A-1) in Appendix A.

Comparison of (3-30) through (3-33) with matrix equation (3-35) reveals that some of the sub-matrices of the impedance matrix can be grouped together as indicated below in (3-41a), (3-42a), (3-43a) and (3-44a). This is due to the fact that their elements have the same expressions as given in (3-41b), (3-42b), (3-43b) and (3-44b), respectively.

$$\left[Z^{\text{int}}\right] = \begin{bmatrix} \left[Z_1^{\text{int}}\right] & \left[Z_1^b\right] \\ \left[Z_2^{\text{int}}\right] & \left[Z_2^b\right] \end{bmatrix} \qquad (3\text{-}41a)$$

$$Z_{ij}^{\text{int}} = \left\langle \hat{z}W_i, \hat{n}\times\underline{H}^{\text{int}}\left(\hat{z}P_j\right)\right\rangle \qquad (3\text{-}41b)$$

$$\left[Z^s\right] = \begin{bmatrix} \left[Z_1^s\right] & \left[Z_1^a\right] \\ \left[Z_2^s\right] & \left[Z_2^a\right] \end{bmatrix} \qquad (3\text{-}42a)$$

$$Z_{ij}^s = \eta_o\left\langle \hat{z}W_i, \hat{n}\times\overline{E}^s\left(\hat{z}P_j\right)\right\rangle \qquad (3\text{-}42b)$$

$$\left[Y^{\text{int}}\right] = \left[\left[Y^{\text{int}}\right] \quad \left[Y^b\right]\right] \qquad (3\text{-}43a)$$

$$Y_{ij}^{\text{int}} = \left\langle \hat{z}W_i, \hat{z}H_z^{\text{int}}\left(\hat{z}P_j\right)\right\rangle \qquad (3\text{-}43b)$$

$$\left[Y^s\right] = \left[\left[Y^s\right] \quad \left[Y^a\right]\right] \qquad (3\text{-}44a)$$

$$Y_{ij}^{s} = \left\langle \hat{z}W_i, \hat{z}H_z^s\left(\hat{z}P_j\right)\right\rangle \tag{3-44b}$$

Implementable expressions for the matrix terms were derived [4]. We can exploit the mathematical similarity between the expressions for the matrix terms of our extended formulation with various expressions provided in the restricted formulation of [4], to arrive at implementable expressions for the impedance and excitation matrices of the extended formulation. The final implementable expression for Z_{ij}^{int} is

$$Z_{ij}^{\text{int}} = \frac{-k\Delta C_j}{8j}\int_{-1}^{1}\left[-\underline{t}_i\cdot\hat{y}a_x + \underline{t}_i\cdot\hat{x}a_y\right]\frac{H_1^{(2)}\left(k\left|\overline{r}_{ij}\right|\right)}{\left|\overline{r}_{ij}\right|}du' \tag{3-45}$$

With the terms $\overline{r}_{ij}$, a_x and a_y, as well as ΔC_j and u', defined in Appendix A. In like manner

$$Z_{ij}^{s} = \frac{-k_o\Delta C_j}{8j}\int_{-1}^{1}\left[-\underline{t}_i\cdot\hat{y}\,a_x + \underline{t}_i\cdot\hat{x}\,a_y\right]\frac{H_1^{(2)}\left(k_o\left|\overline{r}_{ij}\right|\right)}{\left|\overline{r}_{ij}\right|}du' \tag{3-46}$$

The self-terms evaluated to

$$Z_{ii}^{\text{int}} = -Z_{ii}^{s} = 1/2 \tag{3-47}$$

The internal admittance matrix terms are given by

$$Y_{ij}^{\text{int}} = \frac{-k_o\Delta C_j\varepsilon_r}{8}\int_{-1}^{1}H_0^{(2)}\left(k\left|\overline{r}_{ij}\right|\right)du' \tag{3-48a}$$

and

$$Y_{ii}^{\text{int}} = -\frac{\varepsilon_r k_o\Delta C_i}{4}\left[1 - j\frac{2}{\pi}\left(\log\frac{\gamma k\Delta C_i}{4} - 1\right)\right] \tag{3-48b}$$

The constant γ=1.781, with $ln(\gamma)$ being Euler's constant. The external admittance matrix terms are found from

$$Y_{ij}^{s} = \frac{-k_o \Delta C_j}{8} \int_{-1}^{1} H_0^{(2)}\left(k_o \left|\bar{r}_{ij}\right|\right) du' \tag{3-49a}$$

and

$$Y_{ii}^{s} = -\frac{k_o \Delta C_i}{4}\left[1 - j\frac{2}{\pi}\left(\log\frac{\gamma k_o \Delta C_i}{4} - 1\right)\right] \tag{3-49b}$$

The Hankel function approximation (3-50) given below was used to obtain the self term expressions, for which $i = j$.

$$H_0^{(2)}(x) \xrightarrow[x\to 0]{} 1 - j\frac{2}{\pi}\log\left(\frac{\gamma x}{2}\right) \tag{3-50}$$

3.3.4 Expression for Near- and Far-Zone Electric Fields in the H-plane

Equations (3-36) to (3-49) can be used to construct the impedance and excitation matrices of equation (3-35). A FORTRAN code is used to evaluate these using the implementable expressions provided in the previous sections. This matrix equation is then solved to obtain the equivalent current coefficients f_j, g_j, a_j and b_j. The external field can then be found by adding the scattered fields produced by equivalent currents g_j and a_j to the field incident from the line source, namely

$$H_z^{ext} = H_z^{i} + \sum_{j=1}^{N_d+N_s} \hat{z} g_j H_z^{s}\left(\hat{z}P_j\right) + \sum_{j=1}^{N_h} \hat{z} a_j H_z^{s}\left(\hat{z}P_{j+N_d+N_s}\right) \tag{3-51}$$

H_z^{i} is simply (B-1) of Appendix B. The far-zone form of H_z^{ext} is used in the 2D directivity expression (C-6) of Appendix C to determine the 2D directivity of the sub-reflectarray antenna being modelled.

3.4 Concluding Remarks

In Section 3.2 of this chapter we have provided a detailed derivation of the basic design equation for the required reflection phase of each element in a sub-reflectarray that emulates either an ellipsoidal sub-reflector or a hyperboloidal sub-reflector. These have not been described elsewhere. The derivation has been explained in such a way that it facilitates the understanding of the scattering mechanisms of sub-reflectarrays in a manner that will be make the reading of Chapter 4 and Chapter 5 easier.

In Section 3.3 we provided an integral equation / moment method formulation for the full-wave electromagnetic analysis of 2D reflectarrays (and sub-reflectarrays). All expressions necessary to implement the moment method solution have been provided. Such details for this specific integral equation formulation have not been described elsewhere.

Whereas the TE_z formulation in [4] permits only a single conductor/dielectric object, which derived here allows more than one such object to be present. We have also altered the formulation of [4], which considers only excitation by a plane wave, to permit excitation by a magnetic line source. The feed horn antenna is modelled by an infinitely long magnetic line source plus conducting walls (this is a TE_z problem). The incident field from this line source (i.e. the impressed field) excites the wall surface of the horn, the dielectric slab and the conducting strips, resulting in scattered fields internal and external to the dielectric. These scattered fields are considered to be produced by equivalent magnetic currents on these surfaces. The external field is the sum of the incident and the scattered field outside the dielectric. Enforcement of the boundary conditions for the continuity of tangential electric and magnetic fields along the dielectric surface, and zero tangential electric fields on the conducting strips and horn walls, yields a set of coupled integral equations. Application of the method of moments to these integral equations reduces them to a matrix equation. Pulse expansion functions and point matching weighting functions are used in the moment method formulation. The matrix equation is solved to obtain the equivalent currents, from which the electric fields of the antenna can be calculated.

There are three parts to the FORTRAN codes written. The first one deals with the segmentation of the 2-D surface of the horn walls, the dielectric and the conducting strips when all the dimensions have been provided. The second code reads these segment coordinates and builds the impedance and excitation matrices of the matrix equation (3-35) using the expressions derived in Section 3.3, and thereafter solves (3-35) for the unknown equivalent currents. The third code calculates the electromagnetic fields due to these currents. Near and far fields can also be calculated using this third code.

At this stage of the work we therefore have a computationally efficient electromagnetic simulation tool to study the behavior of sub-reflectarrays in complete detail. This will be done in the next chapter, which will begin with an analysis of 2D reflectarrays (parabolic-type), whose behavior is relatively well-known, in order to provide evidence for the validity of the tool as a means of modelling 2D reflectarrays. Only thereafter will we proceed to the analysis of sub-reflectarrays.

3.5 References for Chapter 3

[1] F.N. Arpin, "Multi-Feed spatial power combining reflectarrays", *Mater Thesis* University of Ottawa, Ontario, Canada, pp. 1, September 2004.

[2] V. J. Dailami and Y. Rahmat-Samii, "Some important geometrical features of conic-sections-generated offset reflector antenna" *IEEE Transactions on Antenna and Propagation*, Vol. 28, No. 6, pp. 952-957, November 1980.

[3] D.M. Pozar, S.D. Targonski, and H.D. Syrigos, "Design of millimeter wave microstrip reflectarrays", *IEEE Transactions on Antenna and Propagation*, Vol. 45, No. 2, pp. 287-295, February 1997.

[4] X. Yuan, R.F. Harrington and S.S. Lee, "Electromagnetic scattering by a dielectric cylinder partially covered by conductors", *Journal of Electromagnetic Waves and Applications*, Vol. 2, No. 1 21-44, 1987

Chapter 4

Validation of Sub-Reflectarray Design Equations Using MoM and Array Analysis

4.1 Introduction

There are several objectives to be achieved in this chapter. Mainly, we wish to show the correctness and reliability of the sub-reflectarray design phase equations we derived in Chapter 3. This will be achieved using the two codes we developed in Chapters 2 and 3 respectively, the 2D MoM integral formulation code and the array theory analysis code. Thus the reliability of these codes should be proven before using them to calculate the radiation patterns of sub-reflectarrays. A good step one can start with is to show the validity of the sub-reflectarray design equations by comparing their radiation patterns (both amplitude and phase patterns) to the radiation patterns of their equivalent solid subreflectors. Another objective we wish to achieve is to study the focusing characteristics of the ellipsoidal sub-reflectarray versus its equivalent solid ellipsoid. This will be done by studying the behavior of the virtual focal point with frequency and variation of feed position. It is worth mentioning that Section 4.4 and Section 4.5 deal with 3D cases while all other sections deal with 2D cases.

In Section 4.2 we will present the electromagnetic model geometries, the design parameters and the feed-horns to be used in this chapter. In Section 4.3 we will show the reliability of the array analysis code and the MoM code we developed in Section 2.5 and Section 3.3, respectively. In order to achieve that, we will use them to calculate the radiation pattern of a parabolic reflectarray whose radiation pattern shape is well-known, namely a main lobe with decreasing sidelobes on either side of it. Predicting it will certainly tell us if the codes work correctly. More accurate verification can be done by comparing the calculated HPBW of the main beam (based on approximate mathematical expressions) with that predicted by the codes. In Section 4.4 we will present amplitude and phase radiation patterns of solid ellipsoidal and hyperboloidal subreflectors obtained

using GRASP-SE [1]. It is necessary to do that since these radiation patterns are quite different from those of parabolic reflectors. The radiation patterns of the solid ellipsoid and hyperboloid on their own (as opposed to that of a complete dual reflector antenna) are rarely reported in literature. Thus we need study them to introduce some concepts that we will be used frequently in this chapter like phase error, edge taper and angular range of interest. Continuing with a discussion of solid subreflector radiation patterns in Section 4.5, we show the correspondences between them and those of their equivalent sub-reflectarrays. This will lead to a better understanding of what we are targeting in this thesis. In Section 4.6 we will show a detailed study of the radiation patterns of ellipsoidal and hyperboloidal sub-reflectarrays which have been designed using the key phase design equations derived in Section 3.2. Each radiation pattern calculated using the 2D MoM will be compared with its equivalent radiation patterns generated using 2D array analysis. Both amplitude and phase patterns will be presented using different feed-horns to show the impact of changing the edge taper upon the radiation patterns. The study of sub-reflectarray reflected radiation amplitude and phase patterns has not been presented elsewhere in literature to date.

In section 4.7 we will show how to determine the location of ellipsoidal and hyperboloidal sub-reflectarrays phase centers (virtual focal points). The determination of sub-reflectarray phase center location helps us to calculate the far-zone phase pattern correctly. Moreover it leads to a better dual antenna system performance by achieving the coincidence between the main parabolic reflector phase center (focal point) and the sub-reflectarray phase center (virtual focal point). In Section 4.8 we will discuss the focusing characteristics of ellipsoidal sub-reflectarrays. This will be accomplished by studying the virtual focal point interaction with feed position change and frequency change. Comparison to solid ellipsoid focusing characteristics will be held to show the similarity between both cases (ellipsoidal sub-refletarray and its equivalent solid ellipsoid).

4.2 Electromagnetic Model Geometries Used in this Chapter

The dimensions of the two-dimensional sub-reflectarray or reflectarray which will be modeled using either the array analysis or the MoM are shown in Figure 4.1. The width of the all sub-reflectarrays to be studied is 15.5λ which equals 155mm (f=30GHz) with a dielectric slab thickness of 0.508mm (20mils) and a relative dielectric constant of 3. The length y_f in Figure 4.1 is the distance between the phase center of the feed and the center point of the upper surface of the reflectarray or sub-reflectarray. Its interpretation changes based on the prototype we simulate. For the parabolic-type reflectarray considered in Section 4.3 it will be the focal length, so that $F=y_f$=155mm and hence F/D=1. In the case of the ellipsoidal-type sub-reflectarray to be discussed in Section 4.6, the dimension y_f is the real focal distance, so that $F_R=y_f$=155mm. For the hyperboloidal type sub-reflectarray also treated in Section 4.6, dimension y_f is also the real focal distance, and will have $F_R=y_f$=320mm.

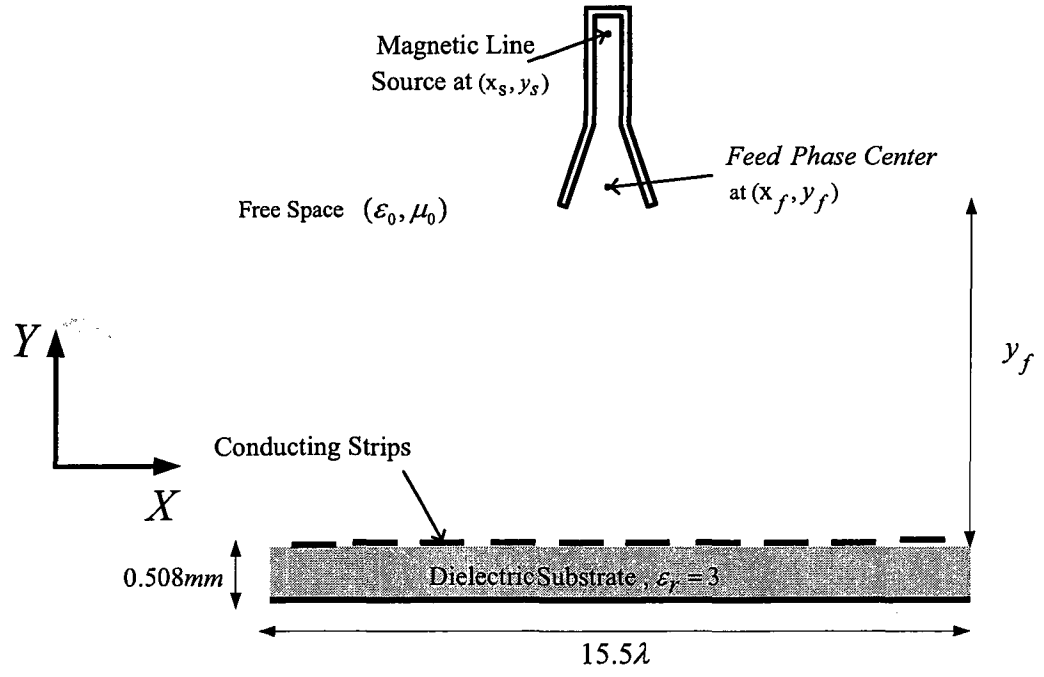

Figure 4.1- Dimensions of two-dimensional sub-reflectarrays used in simulations.

The phase center of the feed will be located at the focal point of the reflectarray and at the real focal points of the ellipsoidal and hyperboloidal sub-reflectarrays. The conducting strip widths will be calculating based on the required phase design equation to be used; parabolic design equation for reflectarray and ellipsoidal or hyperboloidal design equations for sub-reflectarrays.

The phase curve used to calculate the strips lengths in the two-dimensional analysis and the array analysis codes is shown in Figure 2.7; it was generated using HFSS with infinitely long conducting strips of variable widths and a unit cell size of 5mm. Hence the separation between the center coordinates of each pair of strips is 0.5λ =5mm. The feed-horns dimensions used in the 2D MoM modeling are the dimensions of the E-plane cuts of these feed-horns, since the MoM formulation we developed is a TEz formulation. The excitation of the horn is modeled by using a waveguide section with a magnetic line source placed approximately $\lambda_o/4$ (or 2.5 mm for an operating frequency of 30 GHz) away from the short-circuit forming the back wall of the horn. Table 4.1 shows the feed dimensions that will be used in our simulations. In the array analysis code we will model the feed-horn using the $\cos\theta^q$ expression with q will be calculated to give the correct edge taper in the E-plane cut.

Table 4.1- The dimensions of feed-horns used in the simulations

Horn#	waveguide size, mm		Aperture size, mm		Flare lengths, mm	
	a	b	a_1	b_1	l_e	l_h
1	7.11	3.56	13.8	9.25	6.9	9.49
2	7.11	3.56	23.6	17.5	18.01	19.67
3	7.11	3.56	30	20	57.4	58.53
4	7.11	3.56	35	25	75.75	76.3

In Section 4.5 a three-dimensional array analysis will be used to calculate the radiation patterns of sub-reflectarrays in order to be able to compare them with the radiation patterns of their corresponding solid subreflectors which are calculated using GRASP [1]. Thus it is worth mentioning that all design parameters will be same as those of the two-dimensional case presented above except having a three dimensional square sub-reflectarrays with15.5λ size.

4.3 Validation of the Full-Wave MoM and the Array Analysis Modeling Tools

4.3.1 Use of the Array Analysis Method

The array analysis technique we developed in Section 2.5 is an approximate technique since we have not considered feed blockage, finite ground and edge effects, and the coupling effects. However, as we will see, this analysis nevertheless is quite effective. This analysis was carried out using a routine written in MATLAB. In Figures 4.2 and 4.3 we see the predicted E-plane ($\phi = 90^\circ$) and H-plane ($\phi = 0^\circ$) patterns of a parabolic reflectarray respectively. These patterns show that the reflectarray is functioningas expected, since we have a distinct main beam at broadside. To further validate the approximate array analysis under discussion, it was used to compute the half-power beam width, which was found to be 3.245°. An approximate formula [2] for the half power beam width of a rectangular aperture in free space with a uniform distribution gives a half-power beam width $50.6^\circ / (D/\lambda) = 50.6^\circ / (15.\lambda/\lambda) = 3.265^\circ$. These results closely match each other, further validating the reflectarray design and its analysis using the approximate array theory.

The far field pattern prediction for the parabolic-type reflectarray using the approximate array theory encourages us to proceed more confidently to use it in predicting the far field patterns of the ellipsoidal and hyperbolic sub-reflatarrays which are designed using the phase equations derived in Chapter 3. Moreover with such good results one could think of including all factors that affect the radiation patterns, like the blockage effect and the finite groundplane effect in predicting the radiation patterns. This will be accomplished using the full wave electromagnetic analysis that will be validated hereafter in Section 4.3.2. All radiation patterns of sub-reflectarrays in this chapter will be predicted using the two modeling methods to make our simulation validation stronger prior to validating the phase equations experimentally in Chapter 5. In Figures 4.2 and 4.3 the reflectarray amplitude taper mainly depends on the variation of the distance from the feed to the surface of the reflectarray and so is almost uniformly illumination. In other words, it uses q=0 in the raised cosine feed pattern method.

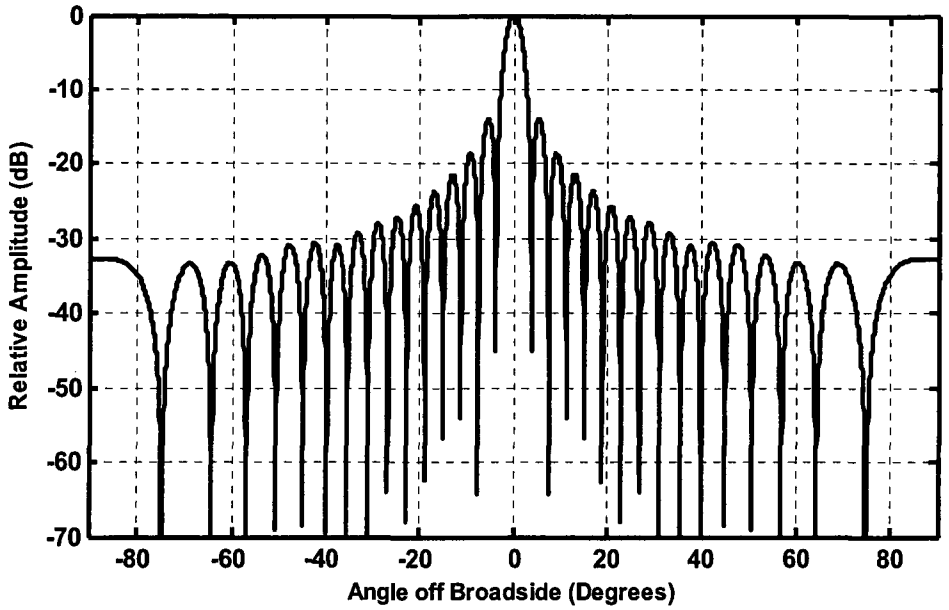

Figure 4.2- Computed E-Plane Far-Field Radiation Pattern of a parabolic reflectarray using array theory. The feed is positioned at the focal point (F=155mm), with almost uniform illumination over the reflectarray aperture.

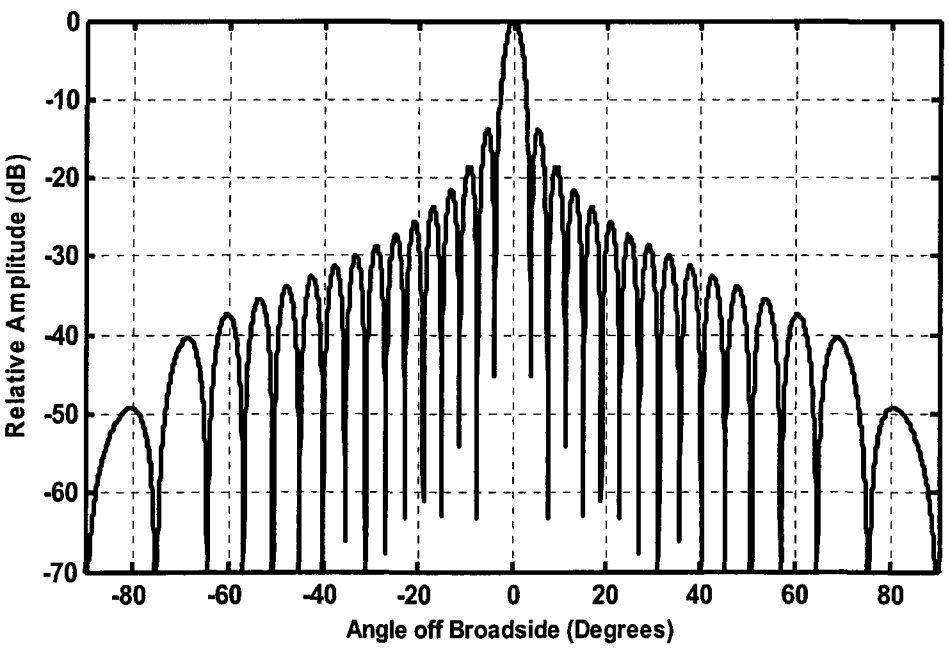

Figure 4.3- Computed H-Plane Far-Field Radiation Pattern of a parabolic reflectarray using array theory. The feed is positioned at the focal point (F=155mm), with almost uniform illumination over the reflectarray aperture.

4.3.2 Use of the Full-Wave Method of Moments Method

The computed E-plane pattern for a two dimensional parabolic reflectarray with a line-source feed is shown in Figure 4.4. It is the field scattered by the reflectarray structure only, since the fields of the line-source are not included. The dashed line pattern is the computed E-plane far field pattern of two-dimensional parabolic reflectarray using full-wave method of moments analysis and the solid line pattern is the computed E-plane far field pattern of the same two-dimensional reflectarray using two-dimensional array analysis.

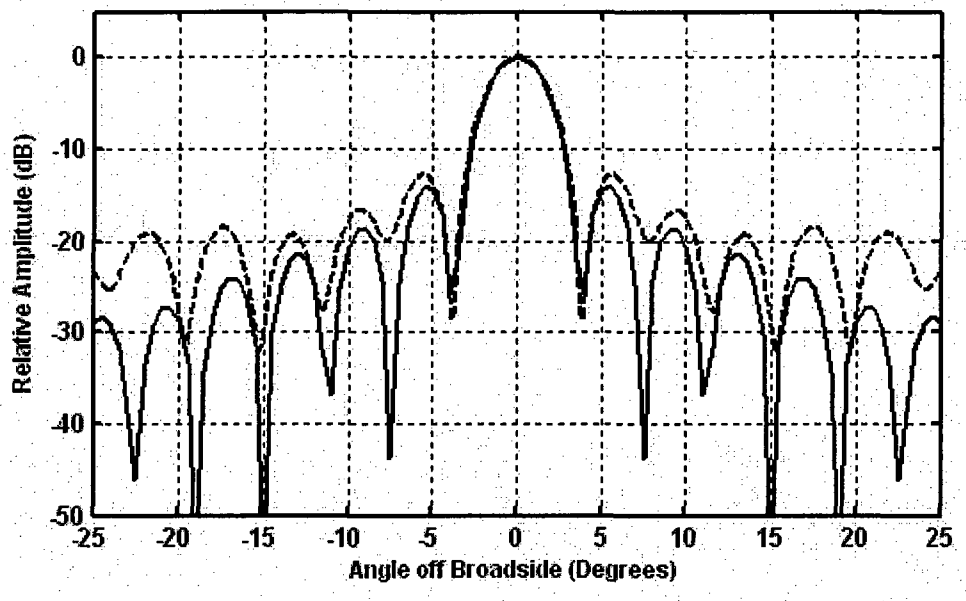

Figure 4.4- Computed E-plane far-zone amplitude pattern of a two dimensional parabolic-type reflectarray, array analysis (——) and a full wave MoM analysis (------) at 30 GHz. Diffraction and finite ground plane effects are automatically included in the full wave MoM analysis. The fields of the line-source have not been included.

Figure 4.4 shows that the full wave MoM analysis is functioning correctly, since we have a distinct main beam at broadside. Since full wave MoM analysis includes the diffraction and the finite groundplane effects, the main beam is very slightly wider than that computed using the approximate array analysis, which leads to a slight reduction of the antenna gain. Moreover, the side lobe level is clearly higher for the MoM case especially as we move a

way from the broadside direction. The finite groundplane effect increases the side lobe level especially at large angles from broadside since the contribution of the currents on the back side of the reflectarray is included. This is expected since the amplitude taper over the reflectarray aperture is controlled only by the variation of the distance from the feed to the surface of the reflectarray (in the present case of a line-source feed). Hence the reflectarray is almost uniformly illuminated and the contribution of the patches close to the rim of the reflectarray is significant, which increases the effects of the edge diffraction. There are no blockage effects in the computation of the radiation patterns of Figure 4.4 because of using line-source as a feed. The source that has been used in the formulation is a magnetic line source. To see the effect of the feed blockage with lower diffraction effect we modeled the E-plane cut of feed-horn#1 of Table 4.1 with an edge taper of -3dB at a subtended angle of 26.56° (the angle between the outermost ray emanating from the feed and the edge of the reflectarray). It is evident from Figure 4.5 that the main beam agreement is very good but at small angles from broadside the side lobe level looks high due to the feed-horn blockage. The diffraction effect is lower compared with Figure 4.4 since the feed applies an amplitude taper across the reflectarray. The diffraction effect, finite groundplane effect and scattering from feed-horn distort the pattern far off broadside.

To see how severe the blockage effect is, we can compare the array analysis with the scattered field of the reflectarray (excluding the scattered field of the horn) produced by the MoM analysis. In order to do this, we exclude the scattered fields due to the currents on the feed-horn walls. This removes the feed blockage effects, but nevertheless still gives the fields scattered from the reflectarray when there is a feed pattern taper of -3dB. Figure 4.6 shows clearly that the MoM-predicted side lobe level at small angles (±15°) are comparable to those of the array analysis since the diffraction effect has been reduced considerably at small angles (due to the feed taper). The pattern distortion far away from the main beam is caused by the finite groundplane effects.

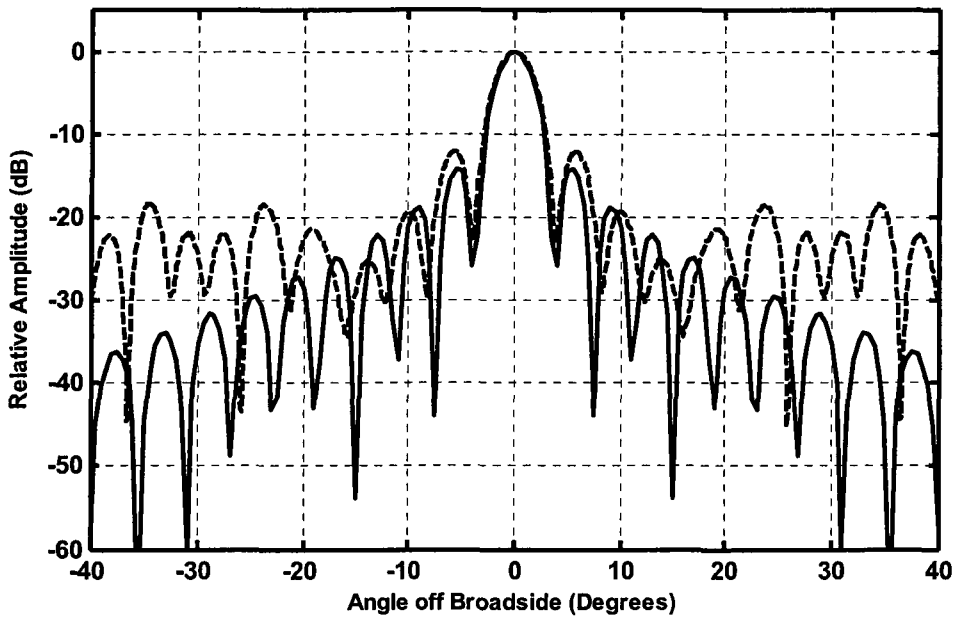

Figure 4.5- Computed total (scattered + incident) E-plane far-zone amplitude pattern of a two dimensional parabolic-type reflectarray using array analysis (——) and a full wave MoM analysis (- - - -). The edge taper is -3dB. Blockage effects of feed-horn#1, and finite groundplane effects, are of course included in full wave MoM analysis.

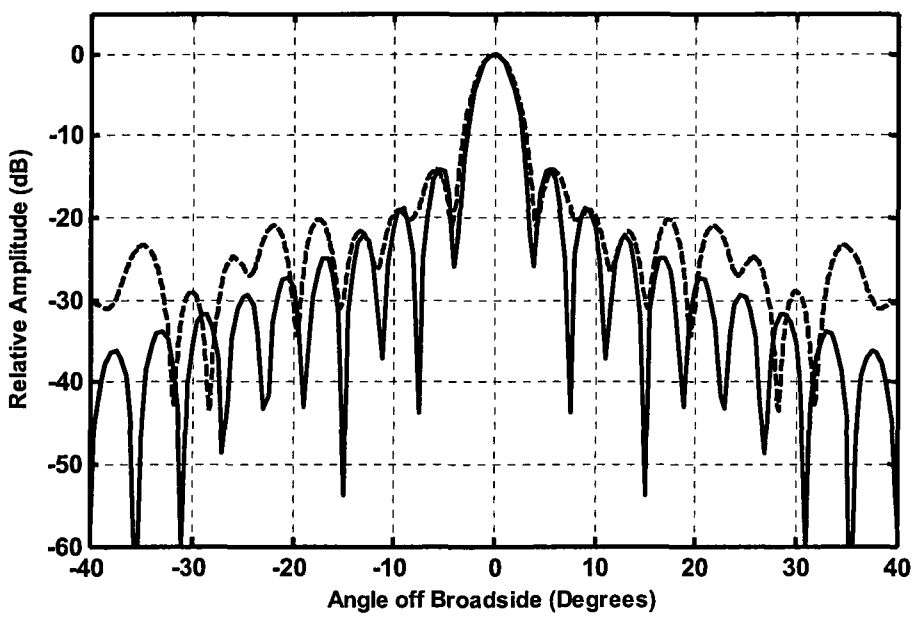

Figure 4.6- Computed E-plane far-zone amplitude pattern of a two dimensional Parabolic-type reflectarray using array analysis (——) and a full wave MoM analysis (------). The edge taper is -3dB. Blockage effects of the feed-horn#1 are excluded from the full wave MoM analysis by ignoring the contributions of currents on all horn walls.

The slight broadening of the main beam in Figure 4.5 and 4.6 reduces the gain of the reflectarray. This is expected since any tapering of the illuminating field over the aperture of the reflectarray would decrease the aperture efficiency.

4.4 Scattering from a Hyperboloidal and Ellipsoidal Subreflectors

In order to understand and analyze the scattered field of sub-reflectarrays, it is important to start by looking at the scattered fields of solid subreflectors. This will give a clear idea about these scattered fields, which are rarely reported in the literature and would clarify some important concepts like the phase error, angular range of interest, and edge taper effects. Unlike the scattered field of a parabolic reflector or reflectarray, which has a narrow directive main beam with considerably low side lobe levels, the scattered field of an ellipsoidal or a hyperboloidal reflector (or their equivalent sub-reflectarray) has a very wide beamwidth with a low directivity. This is completely compatible with the intended functionality of these subreflectors which are used to illuminate the electrically large main parabolic reflector over a relatively wide angular range in most cases. Figures 4.7 and 4.8 show the scattered amplitude and phase patterns of a hyperboloidal subreflector respectively generated by the commercially reliable reflector software GRASP [1]. The hyperboloid design parameters used are: diameter 12.8λ; eccentricity e=1.5 (f= 19.2λ and a=12.8λ); subtended angle $\theta_e = 13.5^\circ$; angular range of interest is $\pm 60^\circ$. The source used in GRASP is a Gaussian beam source. Two different edge taper values will be considered successively, namely -5dB and -15dB. A sketch showing the design parameters is given in Figure 3.4. The operating frequency is 30GHz.

The extreme geometrical ray mentioned above determines what we called the angular range of interest, which can be defined simply as the region in space over which we want to illuminate the main parabolic reflector. As such it is very important to set up the design parameters of the subreflector in a way that enables the subreflector to scatter the incident field of the feed over that prescribed angular range. The *F/D* ratio of the main parabolic reflector should be considered when we set up the geometric design parameters of the

subreflector since the coincidence between the focal point of the main reflector and the virtual focal point of the subreflector is important.

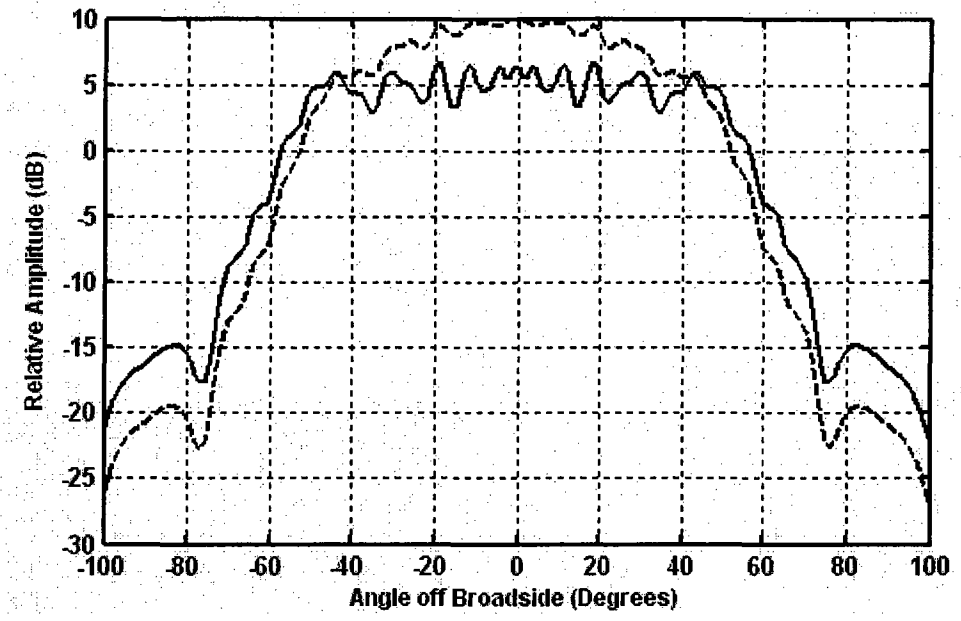

Figure 4.7- Computed H-plane far-zone amplitude pattern of the hyperboloidal subrefletor using GRASP at two edge taper values, -5dB (——) and -15dB (------).

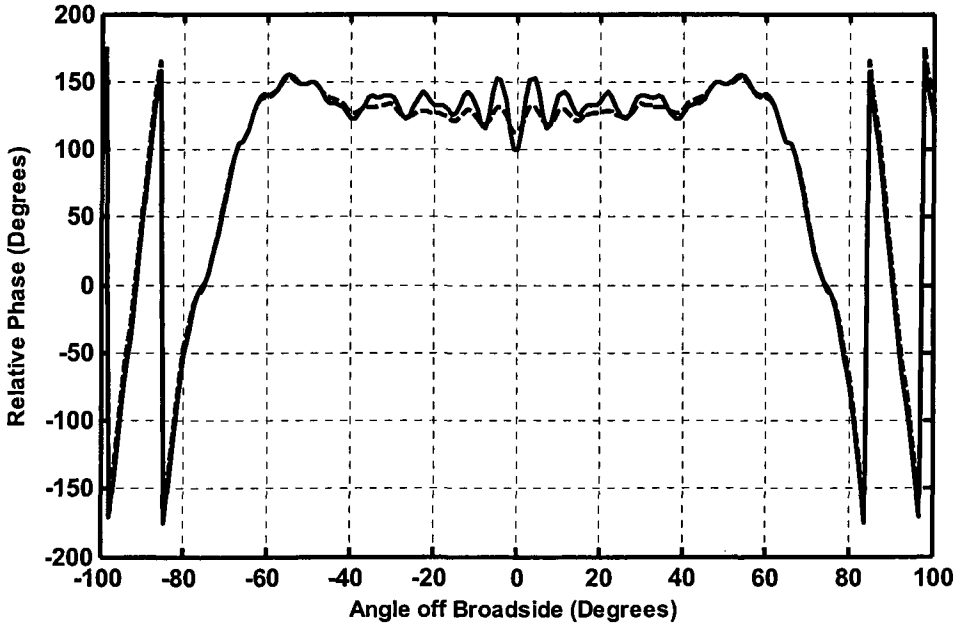

Figure 4.8- Computed H-plane far-zone phase pattern of the hyperboloidal subrefletor using GRASP at two edge taper values, -5dB (——) and -15dB (------). The phase is referenced to the geometrical virtual focal point.

In Figures 4.7 and 4.8 the angular range of interest extends from -60° *to* 60°. Thus since the field is a scattered field, which includes neither the blockage effects nor the feed fields, it is enough to concentrate on the behavior of the field within this angular range. When the blockage and feed fields are included, a high side lobe level could appear directly outside of the angular range of interest. This would increase the forward spillover behind the main parabolic reflector.

The phase error will be defined as the peak-to-peak ripple is the far-zone phase pattern over the angular range of interest. In Figure 4.8 it is clear that the phase error is significantly influenced by the amplitude taper over the surface of the subreflector; the phase error for an edge taper of -15dB is reduced to less than a quarter of its value for an edge taper of -5dB. The amplitude pattern behavior is tied to that of the phase pattern. The deep ripples of the amplitude pattern generated for an edge taper of -5dB almost vanished when the edge taper decreased to -15dB. The change of amplitude taper value from -5dB to -15dB over the subreflector surface has another important impact upon the amplitude pattern; it causes the phase pattern to take on a "concave down" shape over the angular range of interest with exactly -15dB at the extremes of the $\pm 60^\circ$ angular range. As shown, we need sufficient edge taper to get the minimum possible phase error over the surface of the parabolic reflector which needs a uniform phase distribution to optimize the dual reflector system performance. Unfortunately, for the on axis dual reflector system the large amount of edge taper that would reduce the phase error is associated with high blockage effect of the feed-horn (which would need a large aperture). But this creates a large phase error at small angles from the broadside direction, which in turn leads to a considerable distortion of the amplitude pattern in this region. Figure 4.9 [5] shows the theoretical and measured amplitude patterns of a hyperboloidal subreflector with the same eccentricity and angular range of interest we used to generate Figures 4.7 and 4.8. In Figure 4.9 the blockage effect distorts the amplitude pattern at small angles from 0° *to* 20°, but the agreement between the theoretical pattern and the measured pattern is relatively good over the angular range from 20° *to* 80° (note that we exceeded the angular range of interest to check the influence of the side lobe levels directly beyond 60°).

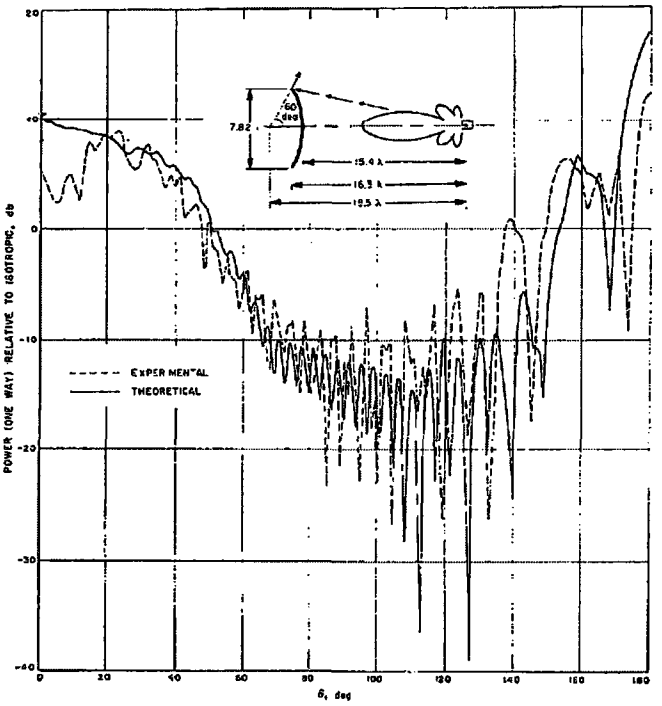

Figure 4.9- Total H-plane far-zone amplitude pattern of a hyperboloidal subrefletor, theoretical pattern (——), measured pattern (------). (After [5])

Similar analysis and interpretations can be done for the scattered amplitude and phase patterns of an ellipsoidal subreflector. The ellipsoidal subreflector design parameters used are: diameter 12.8λ; eccentricity e=0.4344 (f= 4.7λ and a=12.8λ); subtended angle $\theta_e = 26.6°$, angular range of interest is $\pm 60°$. A graphical representation of the design parameters is shown in Figure 3.5. Figures 4.10 and 4.11 successively show the scattered far-zone amplitude and phase patterns of the ellipsoidal subreflector.

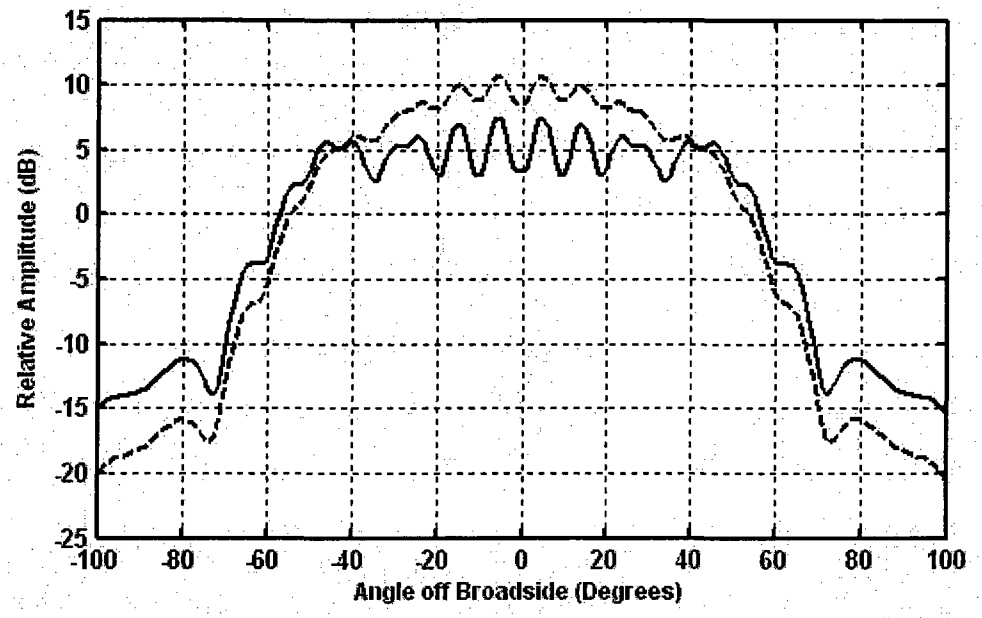

Figure 4.10- Computed H-plane far-zone amplitude pattern of the ellipsoidal subrefletor using GRASP at two edge taper values, -5dB (——) and -15dB (-----).

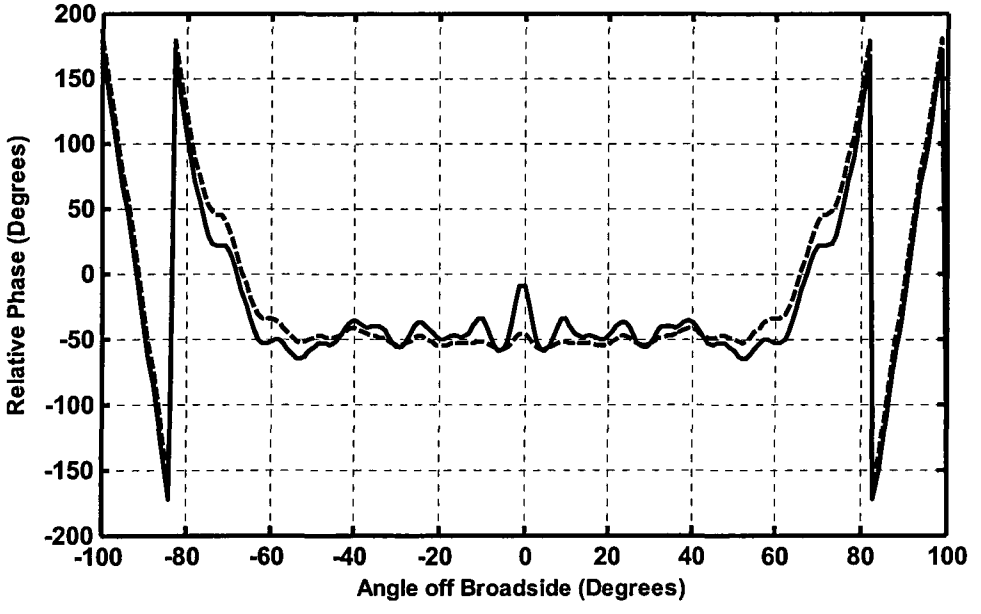

Figure 4.11- Computed H-plane far-zone phase pattern of the ellipsoidal subrefletor using GRASP at two edge taper values, -5dB (——) and -15dB (------).

4.5 Sub-Reflectarrays versus Solid Subreflectors

In order to see how the scattered field of sub-reflectarrays fare compared to their solid sub-reflector equivalents, which in turn validates our derived sub-reflectarray phase equations, the amplitude and phase far field patterns of two subreflectarrays will be compared with their solid subreflector equivalents. In the first example we consider the case where F_R = 292mm and F_V = 115mm [6], as shown in Figure 3.5. The H-plane amplitude and phase radiation patterns at 30 GHz, of a solid ellipsoidal sub-reflector with these parameters (and diameter 142mm), is given by the solid lines in Figures 4.12 and 4.13 respectively. These were obtained using the code GRASP9-SE [1], with a Gaussian-shaped feed pattern that provides a -10dB pattern taper at the reflector edge. Also provided by the dashed lines in the latter figures are the patterns of the equivalent sub-reflectarray obtained using the array analysis technique. The sub-reflectarray layout is that in Figure 4.14. It was designed by applying equation (3-9) and the phase versus patch size curve obtained using an HFSS [7] as shown in Figure 2.5. The raised-cosine feed pattern used for the sub-reflectarray pattern analysis was adjusted to ensure it closely matches the above-mentioned Gaussian-shaped pattern, in this case giving a feed pattern edge taper of about 10dB. The phase patterns are shown referenced to the geometrical virtual focal point indicated in Figure 3.5 (so that $z_{\text{ref}} = -115\,\text{mm}$ in this example), and so are relatively flat within the angular range $\pm 36^{\circ}$ as expected. The comparison between the patterns of the solid sub-reflector and its equivalent sub-reflectarray is favorable. The minor discrepancies between them are due to many reasons. First, the phase curve generation we perform to determine patch sizes is an approximate process. We assume that any wave that hits the sub-reflectarray is locally a plane wave, which is not precisely true. Second, the diffraction effect is not included in the array analysis thus we see deeper ripples on the solid ellipsoid patterns. Third, the model used for the primary feed was not the same for the two methods. The primary feed was modeled in GRASP as a Gaussian beam, and as $\cos\theta^q$ function in the array analysis code. And of course all the phase design equations expressions are approximate expressions from the point of view of rigorous electromagnetic theory.

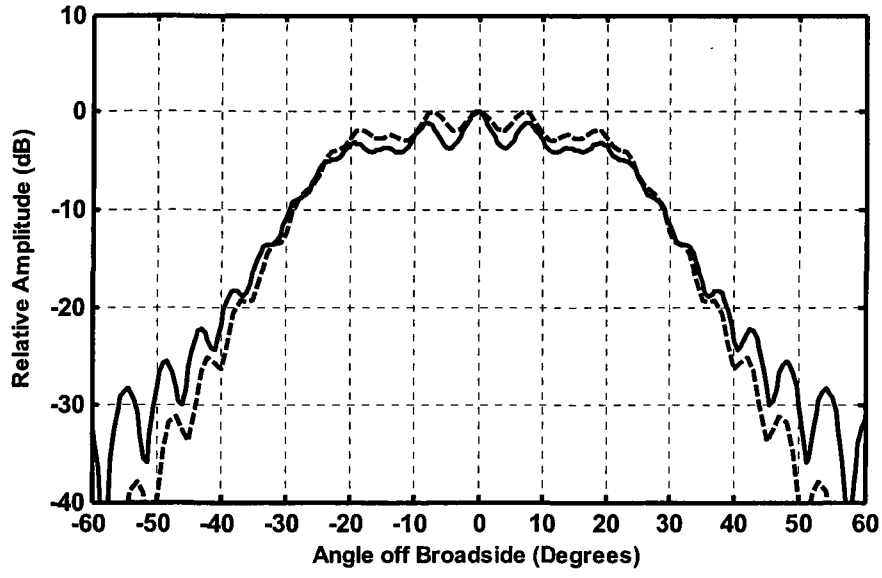

Figure 4.12- Computed H-plane far-zone amplitude pattern of a solid ellipsoidal subreflector using GRASP (——) and its equivalent sub-reflectarray using array analysis (------) at 30 GHz. The edge taper is -10dB.

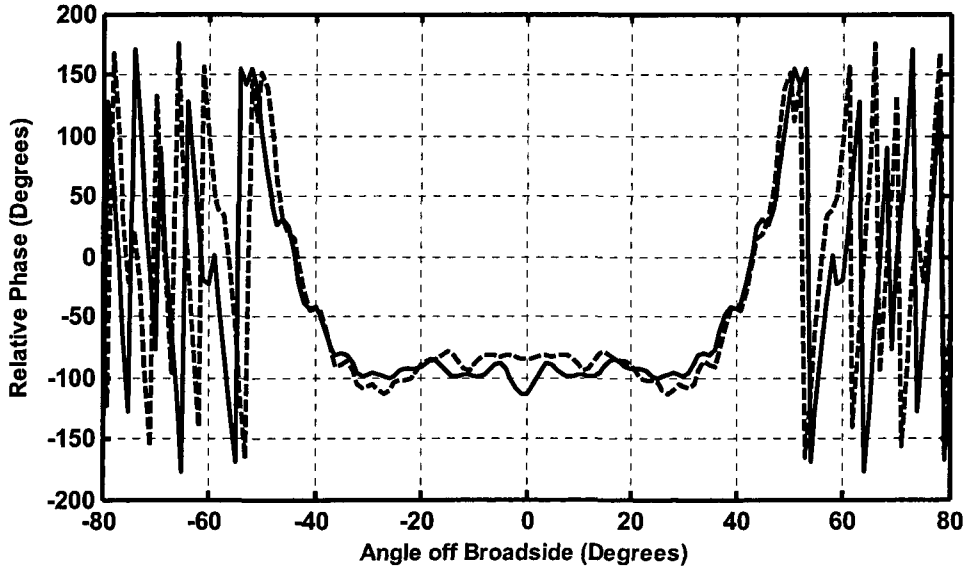

Figure 4.13- Computed H-plane far-zone phase pattern of a solid ellipsoidal subreflector using GRASP (——) and its equivalent sub-reflectarray using array analysis (------) at 30 GHz. The edge taper is -10dB.

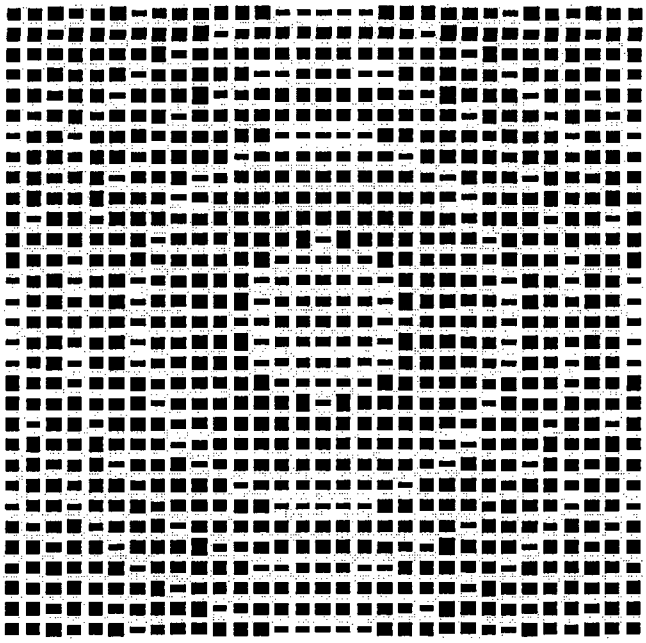

Figure 4.14- Layout of the ellipsoidal sub-reflectarray whose far-zone amplitude and phase patterns are shown in Figures 4.12 and 4.13, respectively. There are 961 elements (31 x 31 patches), the centre-to-centre spacing between elements is $\lambda/2$ at 30GHz, and the sub-reflectarray size is $15.5\lambda \times 15.5\lambda$.

In the second example we consider the case of the hyperboloidal sub-reflectarray where $F_R = 380$mm and $F_V = 114$mm as shown in Figure 3.4. The H-plane amplitude and phase radiation patterns at 30 GHz, of a solid hyperboloidal subreflector with these parameters (and diameter 144mm), is given by the solid lines in Figures 4.15 and 4.16 respectively. These were obtained using the code GRASP9-SE [1], with a Gaussian-shaped feed pattern that provides a -10dB pattern taper at the reflector edge. Also provided by the dashed lines in the latter figures are the patterns of the equivalent sub-reflectarray obtained using the array analysis technique. The sub-reflectarray layout is that in Figure 4.17. It was designed by applying equation (3-6) and phase versus patch size curve in Figure 2.5. The raised-cosine feed pattern used for the sub-reflectarray pattern analysis was adjusted to ensure it closely matches the above-mentioned Gaussian-shaped pattern, in this case giving a feed pattern edge taper of about 10dB. The phase patterns are shown referenced to the geometrical virtual focal point indicated in Figure

3.4 (so that $z_{ref} = 114\,\text{mm}$ in this example), and so are relatively flat within the angular range $\pm 34^\circ$ as expected. Similar to the ellipsoidal case the comparison between the patterns of the solid sub-reflector and its equivalent sub-reflectarray is very good.

It is essential to check both the amplitude and phase patterns in the previous examples as we have done here. Using the wrong design equations it is possible to obtain amplitude patterns which appear deceptively correct but have associated phase patterns which are not those of a sub-reflector. Note that no blockage has been taken into account in either of the situations in Figures 4.12 through 4.16, nor are the fields of the feeds included. It is only the field scattered from the subreflector and sub-reflectarray that is shown. As mentioned in Section 4.2, the sub-reflectarray substrate we used is Rogers RT3003 substrate with $\varepsilon_r = 3$ and a thickness of 20 mils

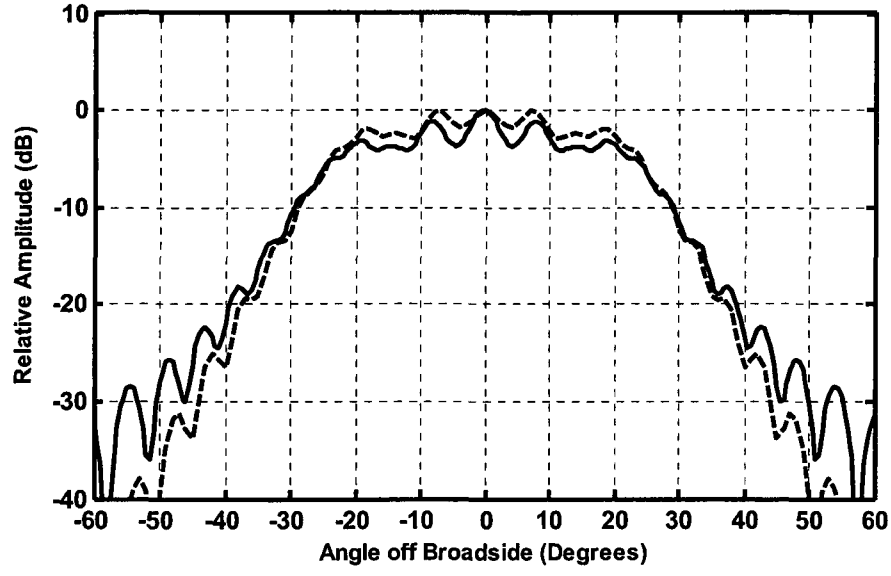

Figure 4.15- Computed H-plane far-zone amplitude pattern of a solid hyperboloidal subreflector using GRASP (——) and its equivalent sub-reflectarray using array analysis (------) at 30 GHz. The edge taper is -10dB.

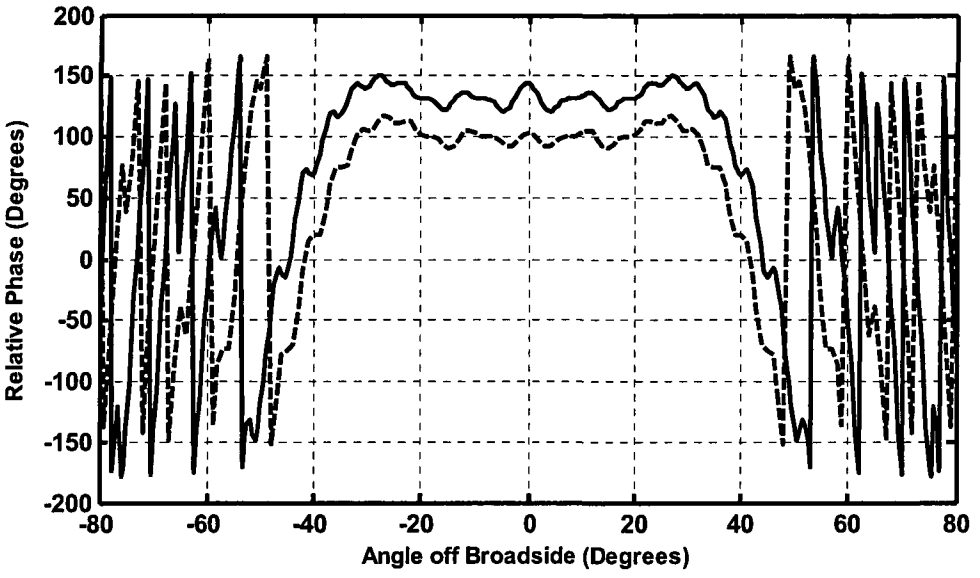

Figure 4.16- Computed H-plane far-zone phase pattern of a solid hyperboloidal subreflector using GRASP (——) and its equivalent sub-reflectarray using array analysis (------) at 30 GHz. The edge taper is -10dB.

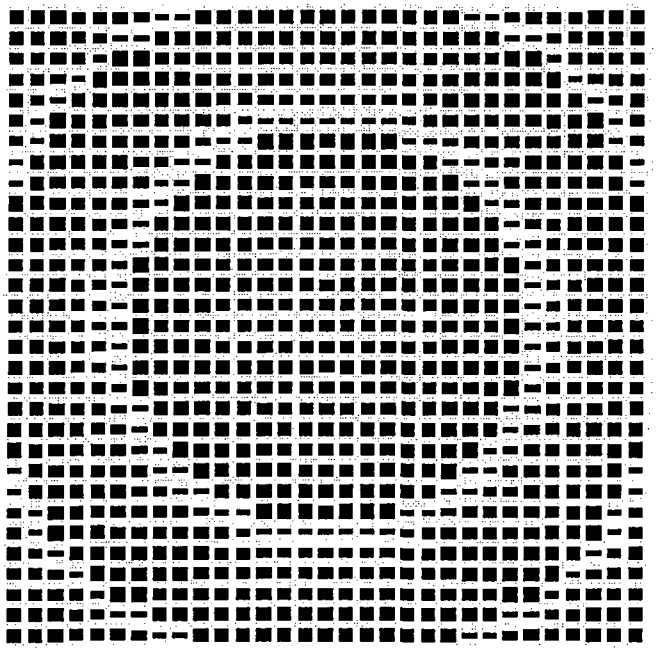

Figure 4.17- Layout of the hyperboloidal sub-reflectarray whose far-zone amplitude and phase patterns are shown in Figures 4.15 and 4.16, respectively. There are 961 elements (31 x 31 patches), the centre-to-centre spacing between elements is $\lambda/2$ at 30GHz, and the sub-reflectarray size is $15.5\lambda \times 15.5\lambda$.

4.6 Validation of Sub-Reflectarray Design Equations Using MoM and Array Analysis

In Section 4.3 we validated the 2D moment method and the array analysis codes by studying the far field radiation patterns of a parabolic-type reflectarray designed based on the general design equation (3-3), we will use both modeling tools to validate the sub-reflectarray design equations we derived in this thesis. Each radiation pattern calculated using the 2D MoM will be compared with its equivalent radiation patterns generated using a 2D array analysis. Both amplitude and phase patterns have been generated with different feed-horns illuminating the sub-reflectarrays to show the impact of changing the edge taper upon both the amplitude and phase far field patterns, as well as to show the impacts of the edge diffraction and the feed blockage upon the radiation patterns.

4.6.1 Validation of the Ellipsoidal Sub-Reflectarray Design Equation

Using the same design parameters presented in Section 4.2 for the ellipsoidal sub-reflectarray, we calculated the E-plane far field amplitude and phase patterns using the 2D full wave MoM and 2D array analysis formulations. The patterns we calculated are total patterns for the MoM case (which means they consist of the field reflected from the sub-reflectarray and the feed-horn field) and scattered field only in the 2D array analysis case. Different horn-feeds have been modeled in both cases. In 2D MoM, an actual feed-horn E-plane cut has been modeled as shown in Figure 4.1, whereas a $\cos\theta^q$ function has been used in the array analysis code to model the feed-horns. It is worth mentioning that the phase centers of all feed-horns have been calculated in advance using SABOR [9] to ensure the coincidence between the real focal point and the calculated phase centers. All conducting strips widths have been calculated based upon design equations (3-9).

The computed far field amplitude and phase patterns of the ellipsoidal sub-reflecatrray illuminated by feed-horn#1, which gives an edge taper of -2.7 dB at the subtended angle $\theta_s = 26.6^\circ$, are shown in Figures 4.18 and 4.19 respectively. The similarity between

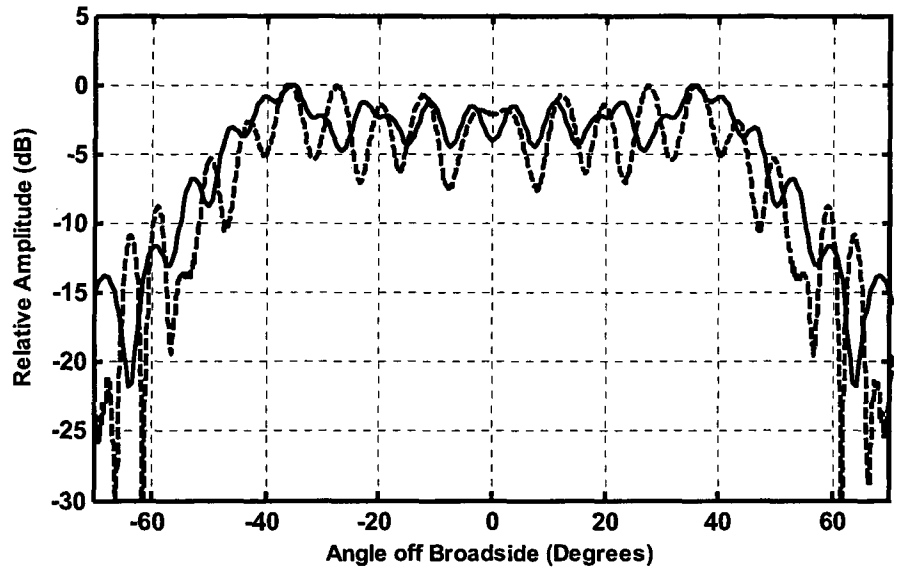

Figure 4.18- Computed E-plane far-zone amplitude pattern of the ellipsoidal sub-reflectarray using array analysis (——) and MoM (------) at 30 GHz. The edge taper is -2.7dB.

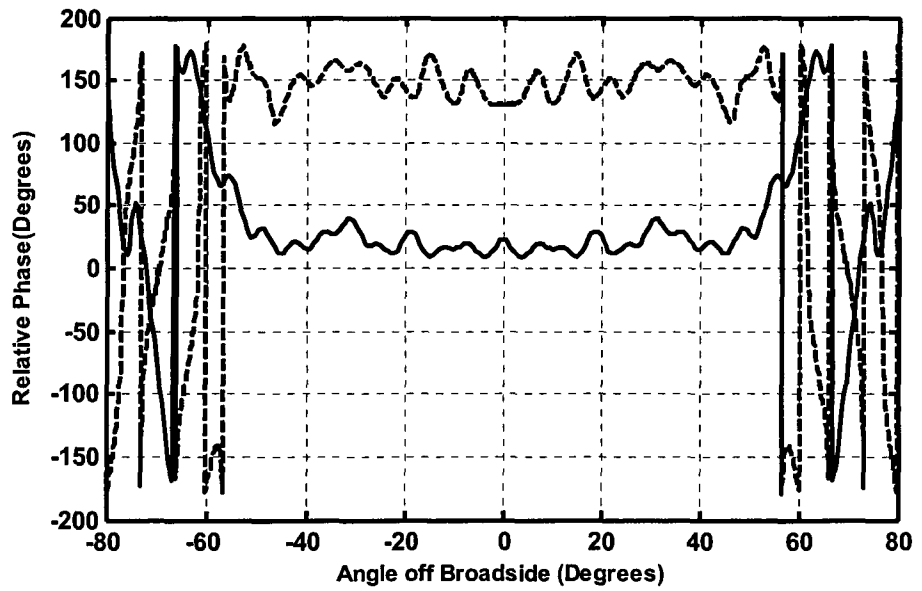

Figure 4.19- Computed E-plane far-zone phase pattern of the ellipsoidal sub-reflectarray using array analysis (——) and MoM (------) at 30 GHz. The edge taper is -2.7dB.

the patterns computed using MoM and array analysis is clear; they cover almost same angular range with similar amplitude patterns envelops with flat phase responses in both cases. However it is noticeable that there are discrepancies between amplitude and phase patterns calculated using the two methods, especially if we look at the ripples depth of both amplitude patterns and the phase error values of the two phase patterns. It is expected to get such differences especially with such a small edge taper; hence the array analysis computed patterns do not suffer from the edge diffraction effect. Moreover the blockage effects are not included in the array analysis code. As such and since all the mentioned effects are included in the full wave MoM, we see relatively deep nulls at small angles from broadside. These are mainly caused by the blockage effect whereas, many other smaller ripples spread over the angular range of interest caused mainly by the diffraction effect and scattering from the feed-horn walls which are not expected to contribute significantly for feed-horn#1 as it has small aperture and flare dimensions.

Similar effects can be used to justify the higher phase error values of the phase pattern computed using MoM code. It has high phase error compared with the phase pattern generated using the array analysis, which causes the ripples shown on the amplitude pattern. The blockage effect is clear around the broadside direction in the phase pattern predicted using the MoM. Since the feed is small, the blockage effect is limited and scattering from its walls does not have a large impact upon the phase pattern. However using feed-horns with larger dimensions are expected to show more phase error caused by scattering from the feed-horn walls and the blockage effect it introduces.

Further study of the edge taper impact upon the radiation patterns of the ellipsoidal sub-reflectarray can be achieved by illuminating the sub-reflectarray with lower amplitude taper. We know from Section 4.4 what impact increased tapering has on the pattern of a solid ellipsoidal subreflector. If the general trends are the same for the ellipsoidal-type sub-reflectarray, this would increase confidence in the correctness of the design equation. To achieve that goal we replaced feed-horn#1 in Figure 4.1 by feed-horn#2 that gives lower amplitude taper of -9dB. Figures 4.20 and 4.21 show the far field

amplitude and phase patterns respectively with feed-horn#2 illuminating the ellipsoidal sub-reflectarray. It is evident from Figure 4.20 that the null depths at small angles is larger than that of Figure 4.18 (which uses feed-horn#1) since the feed-horn#2 aperture is larger that that of feed-horn#1, and so there is more blockage.

More importantly, in the region of the greatest importance $\pm 15^{\circ}$ *to* $\pm 60^{\circ}$ the ripples depths of Figure 4.20 amplitude pattern were reduced considerably compared with ripples depths of amplitude pattern on Figure 4.18. This is mainly due to the increased edge taper. As we increase the edge taper both the diffraction and the finite groundplane effects are reduced since the field value near the edges of the groundplane is reduced; the MoM analysis exhibits this behavior.

One thing that might be confusing is the comparable phase error in both cases, or the even higher phase error at small angles with the usage of feed-horn#2. This might appear to contradict the result we expect when increasing the amplitude taper. However, we can justifying that by recognizing the fact that the increased edge taper associated with larger feed-horn#2 is associated by increased blockage. We can in fact demonstrate that this so can be done by comparing the total far field patterns of the ellipsoidal sub-reflectarray using two feed-horns of comparable aperture size but different edge tapers. This can be accomplished by increasing the flare length of one of them considerably. The two feed-horns used are feed-horn#2 and feed-horn#3 with edge tapers -9dB and -14dB respectively. Figures 4.22 and 4.23 show the far field total and scattered amplitude far field E-plane radiation patterns of the ellipsoidal sub-reflectarray using these two mentioned feed-horns.

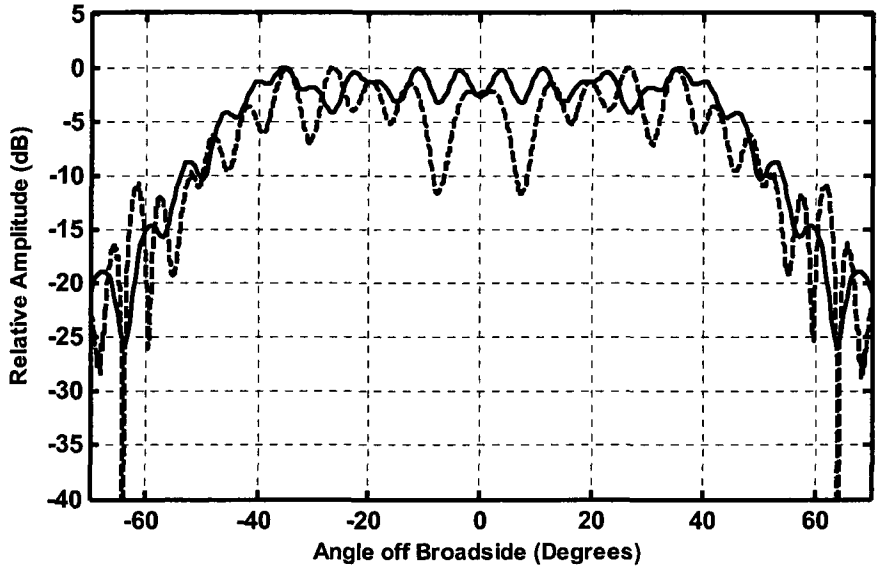

Figure 4.20- Computed E-plane far-zone amplitude pattern of the ellipsoidal sub-reflectarray using array analysis (——) and MoM (------) at 30 GHz. The edge taper is -9dB.

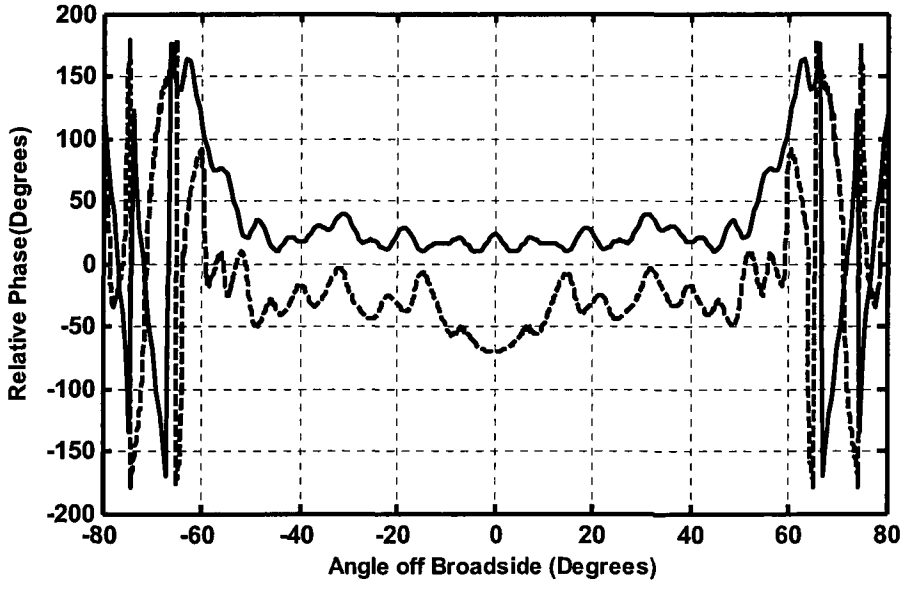

Figure 4.21- Computed E-plane far-zone phase pattern of the ellipsoidal sub-reflectarray using array analysis (——) and MoM (------) at 30 GHz. The edge taper is - 9dB.

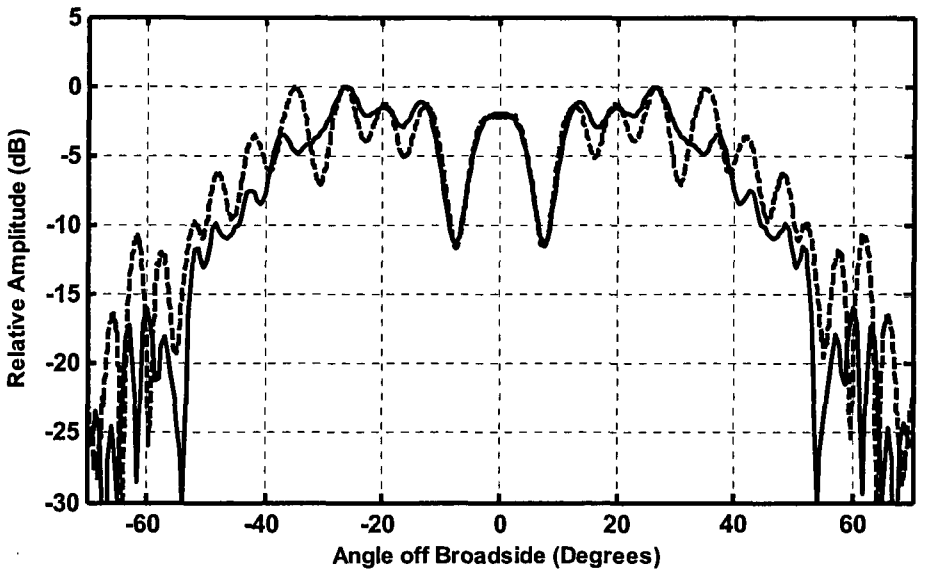

Figure 4.22- Computed total E-plane far-zone amplitude pattern of the ellipsoidal sub-reflectarray calculated using the full wave MoM code at two different edge taper values, -14dB (——) and -9dB (- - - - -) at 30 GHz.

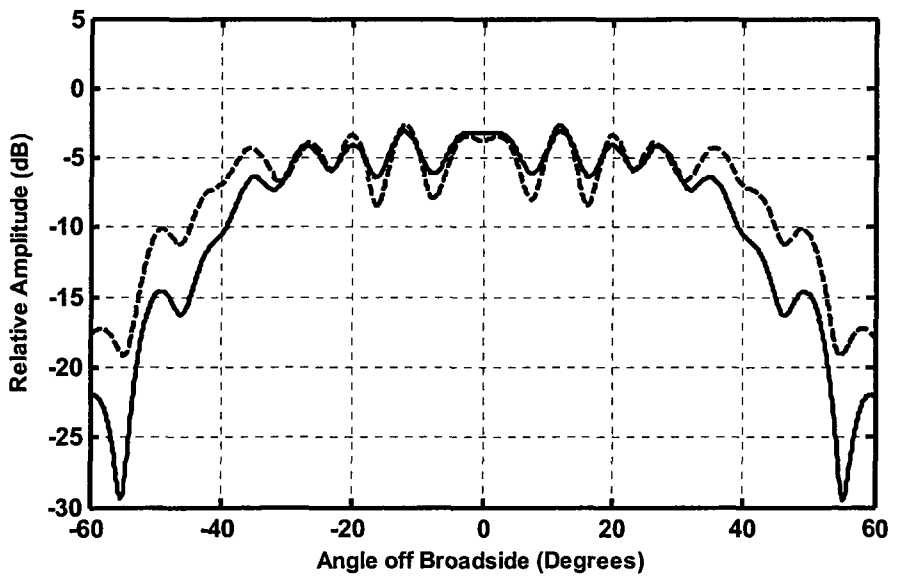

Figure 4.23- Computed scattered E-plane far-zone amplitude pattern of the ellipsoidal sub-reflectarray calculated using the full wave MoM code at two different edge taper values, -14dB (——) and -9dB (------) at 30 GHz.

It is evident from Figure 4.20 that the considerable increase of edge taper from about -9dB to -14dB has minimized the ripple depths very much within the region of greatest importance $\pm 15^{\circ}$ *to* $\pm 60^{\circ}$. This is what we are trying to show. The amplitude pattern obtained using feed-horn#2 is a bit narrower than that using feed-horn#1. This is also expected, since we observed this for the solid subreflector in Figure 4.10. To make this point still clearer Figure 4.23 shows the scattered amplitude patterns of the ellipsoidal sub-reflectarray using the two edge taper values mentioned above; recall that these scattered patterns have the effects of the feed-horn wall currents excluded.

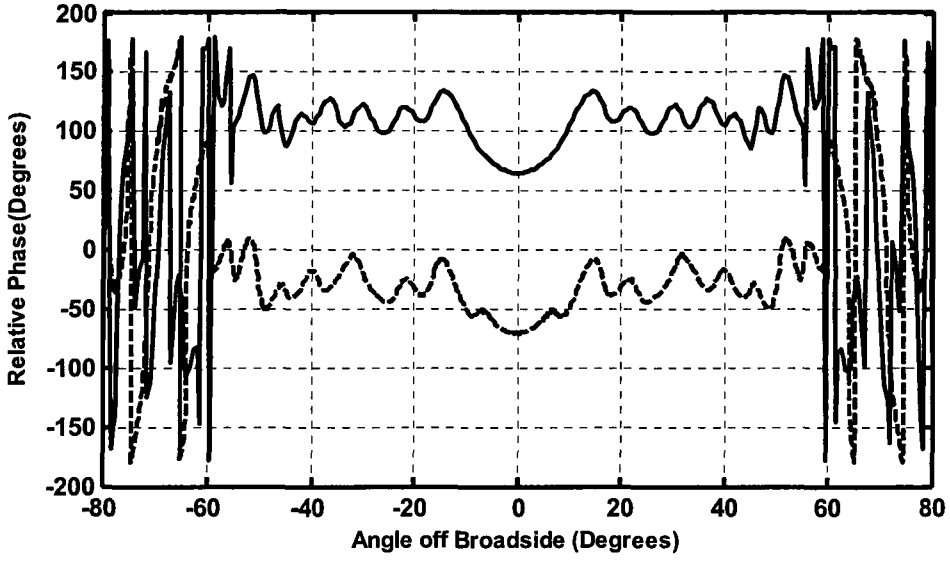

Figure 4.24- Computed total E-plane far-zone phase pattern of the ellipsoidal sub-reflectarray calculated using the full wave MoM code at two different edge tapers, -14dB (——) an -9dB (----) at 30 GHz

Figure 4.24 shows the phase patterns of amplitude patterns (all generated using MoM) shown in Figure 4.20. It is straightforward now to conclude the impact of the amplitude taper upon the radiation patterns of the ellipsoidal sub-reflectarray. The phase error associated with -14dB edge taper is lower than that with -9dB edge taper, as also reflected in the amplitude patterns presented earlier.

It is worth mentioning that the order of typical edge taper used in many reported research work on sub-reflectarrays is around -18 to -20 dB [9,10], which still way below the -14 dB we used (the horn aperture size starts to become very large at such edge taper values). The reason behind the usage of such very low edge taper is to minimize the phase error to the lowest possible degree to enhance the uniformity of the phase over the main reflector surface and then to optimize the overall dual reflector system performance. However the work in [9, 10] is for offset configuration where feed blockage is not an issue.

4.6.2 Validation of the Hyperboloidal Sub-Reflectarray Design Equation

To design the 2D hyperboloidal sub-reflectarray, we used same dielectric substrate parameters (h=20mils and ε_r=3) presented in Section 4.2 with all conducting strips widths calculated based on equation (3-6). The focal length y_f shown in Figure 4.1 is 320mm for the hyperboloidal sub-reflectarray considered here. As for the ellipsoidal sub-reflectarray in Section 4.6.1, we calculated the E-plane far field amplitude and phase patterns using the 2D full wave MoM, and 2D array analysis, formulations. The patterns we calculated are total patterns, which means they consist of the field reflected from the sub-reflactarray and the feed-horn field. Two feed-horns have been modeled to illuminate the hyperboloidal sub-reflectarray, namely feed-horn#3 (that gives -2.5dB edge taper at the subtended angle of interest $\theta_s = 13.5^\circ$) and feed-horn#4 that gives -9dB edge taper.

The resulting far field E-plane amplitude and phase radiation patterns using feed-horn#3 illuminating the hyperboloidal sub-reflectarray are shown in Figures 4.25 and 4.26 respectively. Figures 4.27 and 4.28 show the resulting patterns when feed-horn#4 illuminates the hyperboloidal sub-reflectarray. With same interpretations we used to comment upon the ellipsoidal sub-reflectarray radiation patterns, we again note the similarity between the patterns computed using the MoM and array analysis. They cover almost the same angular range with similar amplitude patterns envelopes and flat phase

responses in both cases. With an edge taper of -9dB the similarity is very good even though the array analysis code does not account for blockage or finite groundplane effects. This nicely supports the correctness of the phase design equations that have been used.

The deep amplitude ripples and high phase errors associated with edge taper of -2.5dB is expected, since finite groundplane effects are high. To minimize the phase error and its undesirable consequences we increased the amplitude taper to get lower phase error and less amplitude's ripple depth in the angular region of interest, as shown in Figures 4.27 and 4.28. To see more clearly the pattern changes achieved by increasing the amplitude taper we plot both edge taper cases in Figures 4.29 and 4.30 respectively. It is clear that the phase error associated with -9dB edge taper is considerably lower than that with the -2.5dB edge taper, which is also directly reflected in the amplitude patterns of Figures 4.25 and 4.27. The blockage effect of feed-horn#4 is a bit higher than that of feed-horn#3 since its aperture dimension in the E-plane is 20% larger. The difference in blockage effect of both feed-horns is noticeable especially at small angles on Figure 4.29.

The similarity between the behavior of the above hyperboloidal-type sub-reflectarray, and that of the solid hyperboloidal subreflector presented in Figures 4.7 and 4.8, finalizes the theoretical validation of the phase design equation (3-6).

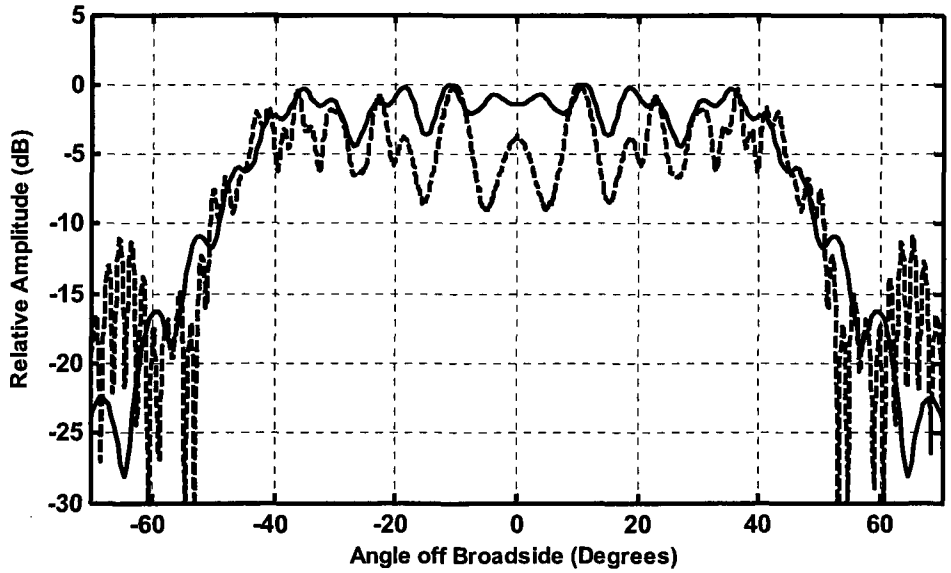

Figure 4.25- Computed E-plane far-zone amplitude pattern of the hyperboloidal sub-reflectarray using array analysis (——) and MoM (------) at 30 GHz. The edge taper is - 2.5dB.

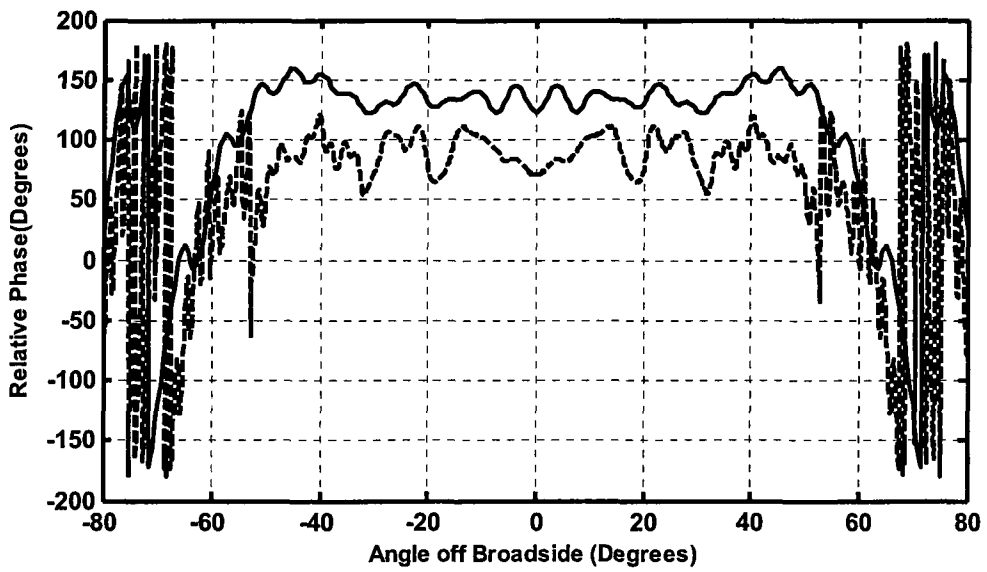

Figure 4.26- Computed E-plane far-zone phase pattern of the hyperboloidal sub-reflectarray using array analysis (——) and MoM (------) at 30 GHz. The edge taper is - 2.5dB.

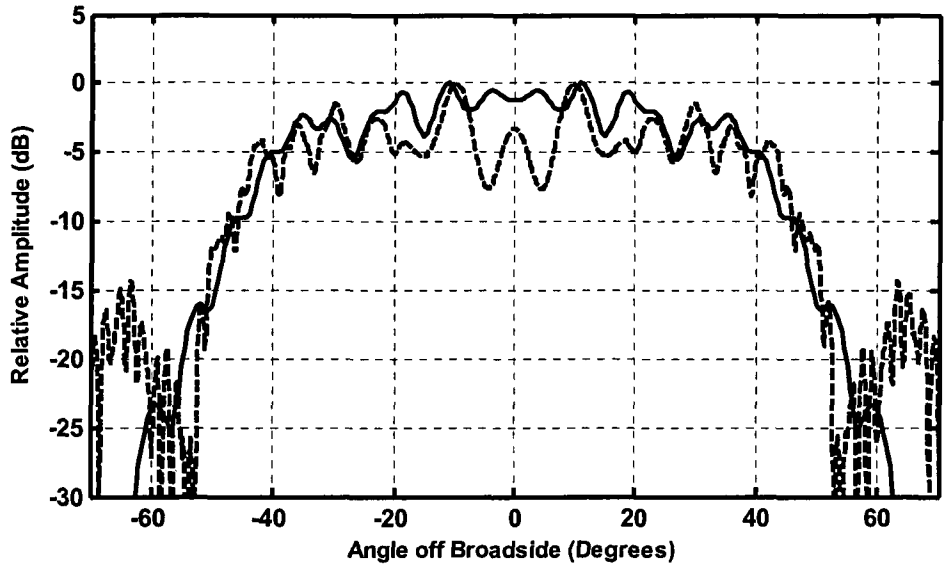

Figure 4.27- Computed E-plane far-zone amplitude pattern of the hyperboloidal sub-reflectarray using array analysis (——) and MoM (------) at 30 GHz. The edge taper is - 9dB.

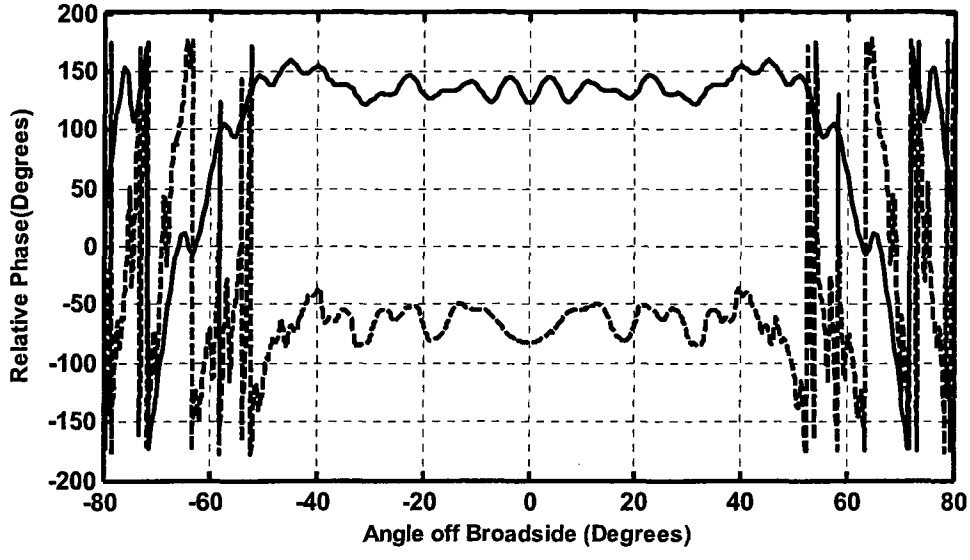

Figure 4.28- Computed E-plane far-zone phase pattern of the hyperboloidal sub-reflectarray using array analysis (——) and MoM (------) at 30 GHz. The edge taper is - 9dB.

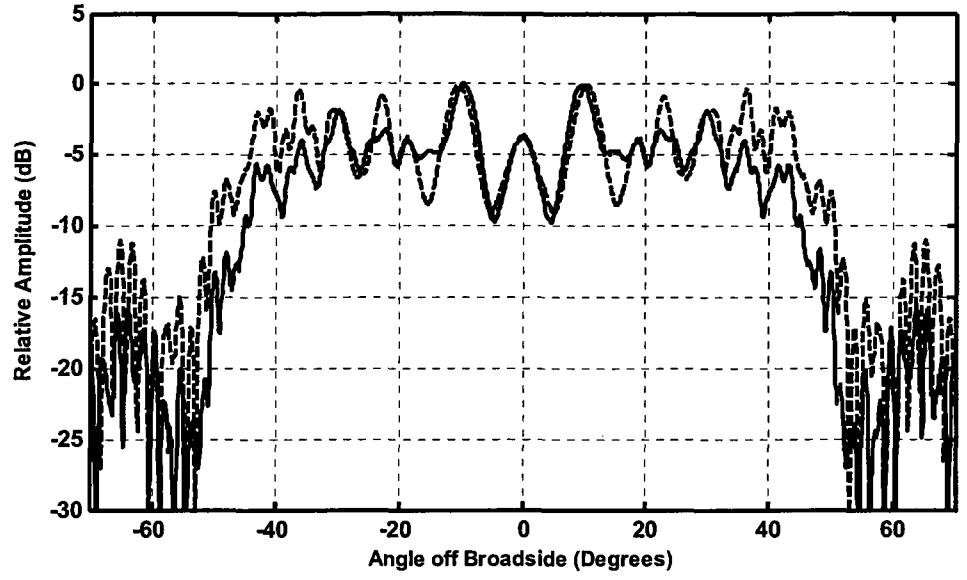

Figure 4.29- Computed total E-plane far-zone amplitude pattern of the hyperboloidal sub-reflectarray calculated using the full wave MoM code at two different edge taper values, -9dB (——) and -2.5dB (------) at 30 GHz.

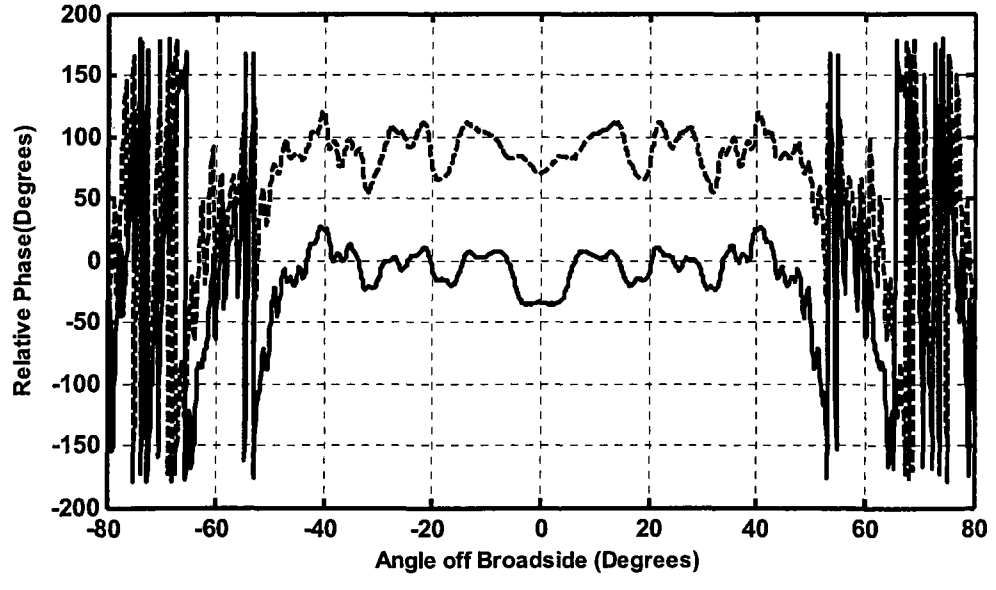

Figure 4.30- Computed total E-plane far-zone phase pattern of the hyperboloidal sub-reflectarray calculated using the full wave MoM code at two different edge taper values, -9dB (——) and -2.5dB (------) at 30 GHz.

4.7 Sub-Reflectarrays Phase Centers

4.7.1 Primarily Remarks

All the far field phase patterns we calculated in Section 4.5 and Section 4.6 are referenced to the virtual foci of the solid subreflectors or their equivalent sub-reflectarrays. We did that since we want to reference the phase patterns to the point from which the spherical waves emerge (the phase center of the spherical wave). This enables us to check the uniformity of the phase and the phase error over the main parabolic reflector surface since the phase over any spherical cap centered at the virtual focal point should be as uniform as possible, as shown in Figures 3.2, 3.8 and 3.10. In Figures 3.8 and 3.10 any ray emerging from the feed and undergoing reflection from the subreflector travels the same distance to any spherical surface centered at the virtual focal point. For the equivalent sub-reflectarrays we compensate for any phase difference by changing the patch dimensions (using the phase equations) to end up with same phase over any spherical surface centered at the virtual focal point. We do not expect a perfect coincidence between the geometric virtual focal point of the solid subreflector and the virtual focal point of its equivalent sub-reflectarray, the difference depending upon the focal length, the eccentricity and the size of the subreflector and its equivalent sub-reflectarray.

4.7.2 Ellipsoidal Sub-Reflectarray Phase Center

For the ellipsoidal subreflector, the best and most accurate way to find out the phase center is to calculate the near field over the axis of symmetry Z shown in Figures 3.8 and 3.10. Based on a ray tracing view point, the point at which all rays intersect and re-emerge with a spherical wave front is the point at which we have the highest electric field intensity, and it should be the phase center. Thus if we use the full wave electromagnetic MoM 2D code to calculate the near field along the axis of symmetry we can find out the location of the virtual focal point. Figure 4.31 shows the scattered field from an ellipsoidal subreflector of eccentricity of 0.4352 where the feed is a line source located at F_R=155mm from the subreflector and the geometrical virtual focal point is located

at F_V=61mm. It is evident that the point of greatest field strength is at F_V= 60.72mm, which deviates .028λ from the assumed geometric virtual focal point location. This shift is expected [5]. The number of segments per λ used in the MoM simulation was 80, more segments having been shown to alter the result negligibly.

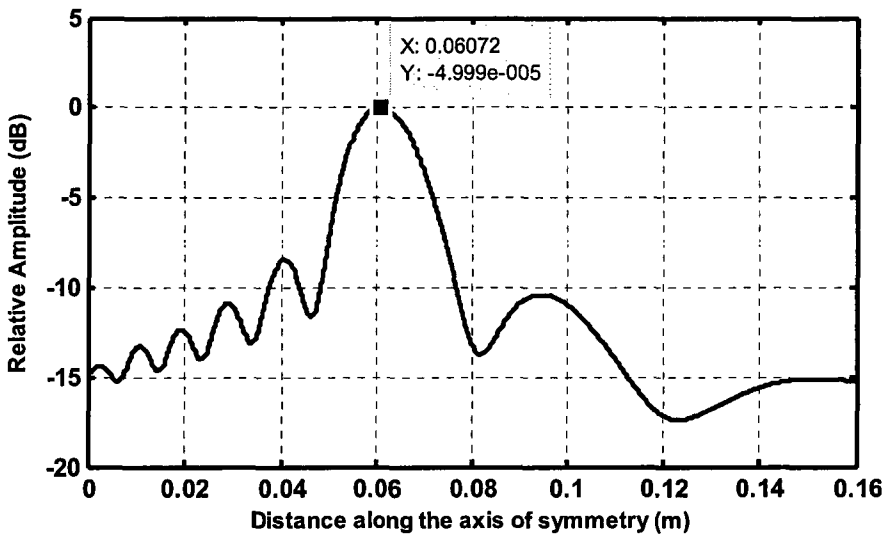

Figure 4.31- Computed scattered field of the ellipsoidal subreflector along the axis of symmetry. The ellipsoid is illuminated by a line source located at F_R=155mm.

The equivalent sub-reflectarray of the same design parameters illuminated by a line source and with a size of 15.5λ has the highest field value at F_V=62.45, as shown in Figure 4.32. This shift from the geometric virtual focal point location F_V= 61mm can be ascribed to the approximations used in the reflection phase design curve generation process mentioned earlier. For the example presented in Section 4.6 with feed-horn#2 illuminating the ellipsoidal sub-reflectarray it was found that the virtual focal point shifted (to F_V=63.5) about$\lambda/10$ compared to its location with the present line source illumination as shown in Figure 4.33. This change of focal point position can be justified if we remember that the phase center calculation of the feed-horns using SABOR [8] is an approximate technique. Moreover, one could surmise that the virtual focal point position of the sub-reflectarray changes with the edge taper value which was changed

from almost 0dB with the line source illuminating the sub-reflectarray to about -9dB when feed-horn#2 used.

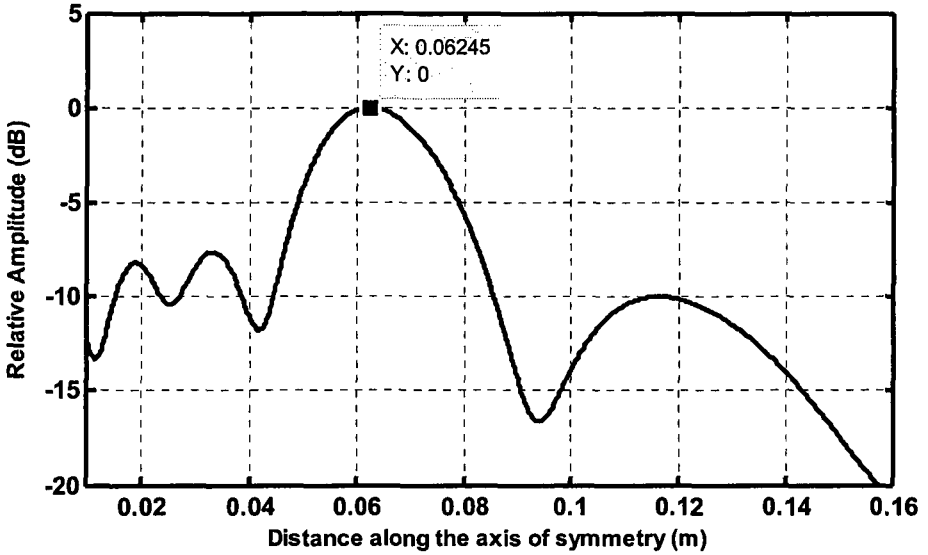

4.32- Computed scattered field of the ellipsoidal sub-reflectarray along the axis of symmetry. The sub-reflectarray is illuminated by a line source located at F_R=155mm.

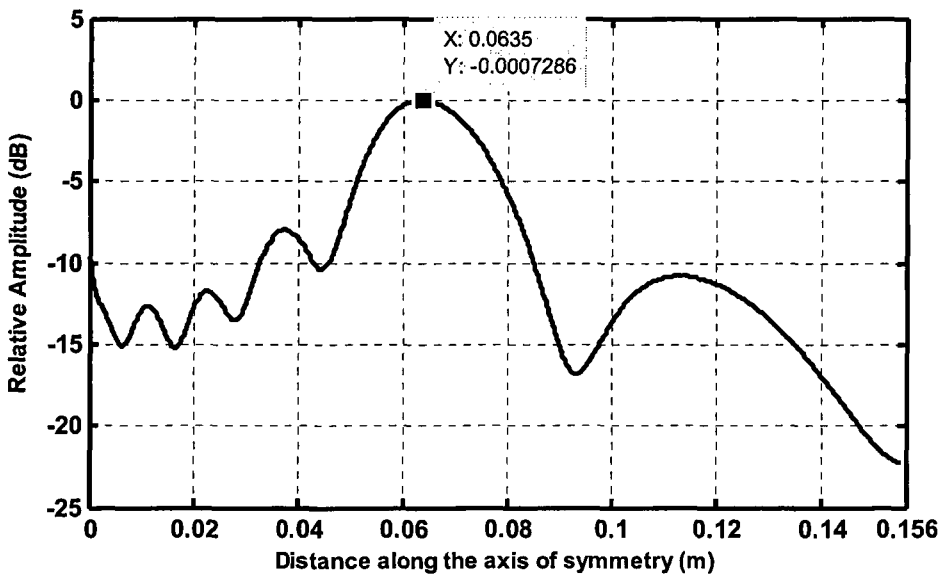

4.33- Computed scattered field from the ellipsoidal sub-reflectarray along the axis of symmetry. The sub-reflectarray is illuminated by a feed-horn#2 with its phase center located at F_R=155mm.

The virtual focal point position F_V=63.5mm with feed-horn#2 illuminating the ellipsoidal sub-reflectarray has been investigated in several ways to make sure that the virtual focal point location we determined is the best fit phase center which can be used to calculate the far field phase pattern. One method is the calculation of the field over axis of symmetry.

Another method is to verify that the virtual focal point calculated is the best fit phase center. This can be used with either simulation or measurements. We calculated the far field phase pattern of the given sub-reflectarray using the 3D array analysis with the $\cos\theta^q$ function to model feed-horn#2. Using a phase center located at F_V=63.5 and at $F_V \pm (1/4)\lambda$, we end up with three phase responses referenced to these three reference locations used as shown in Figure 4.34. A similar behavior will be observed in the measured results in Figure 5.7 of Chapter 5 when we discuss experimental validation of the basic design equations there.

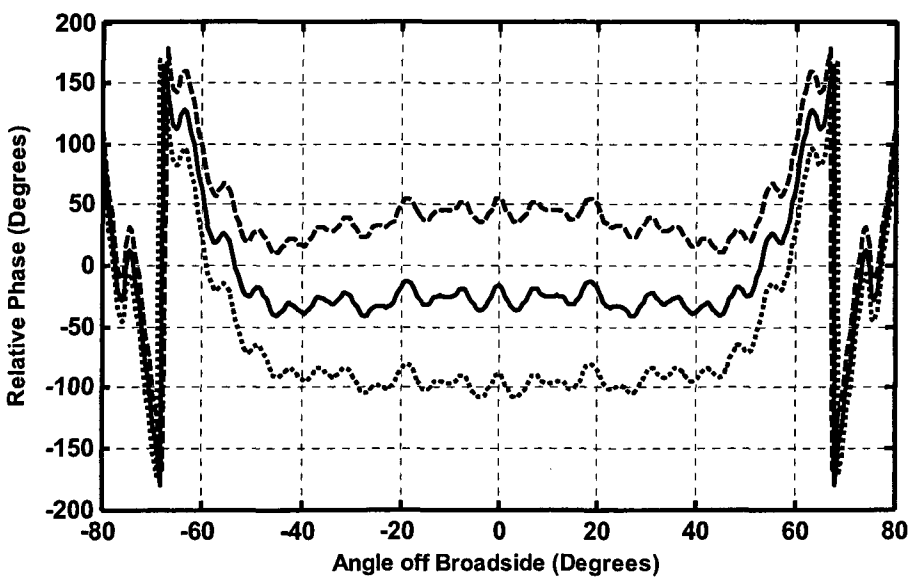

Figure 4.34- Computed H-plane far-zone phase patterns of the ellipsoidal sub-reflectarray calculated using the 3D array analysis code with the patterns calculation referenced to three points located quarter wavelength apart; F_V =61(--------), F_V = 63.5mm (——) and F_V =66 (.....).

In Figure 4.34, it is evident that the virtual focal point located at F_V=63.5 represents the best fit phase center since the calculated phase pattern referenced to this phase center has the best flatness. This can be realized by examining the plots or using the following procedure: calculate the mean of all phase values and then check how far it is from the mean of the maximum phase deviations within the angular range of interest. We did this for very tiny change of the phase reference point since as the figures show a quarter wavelength shift changed the phase pattern significantly. A shift of $\lambda/4$ backwards (to F_V=61mm) caused the phase pattern to be concave down whereas a $\lambda/4$ shift forwards (to F_V=66mm) gave a concave up phase pattern. As an aside we comment that the fact that the far field phase patterns of sub-reflectarrays are so sensitive to any tiny shift of the phase center could in fact be used as a measurement technique to precisely determine feed-horn phase centers. However, this would need to be investigated further, and is outside the goals of this thesis.

4.7.3 Hyperboloidal Sub-Reflectarray Phase Center

Unlike the ellipsoidal sub-reflectarray, it is not possible to determine the virtual focal point of the hyperboloidal sub-reflectarray by calculating the near field along the axis of symmetry since the virtual focal point of the hyperboloidal sub-reflectarray lies behind it, as shown in Figure 3.10. It is a true "virtual" focal point. As such we can only use the second method to predict the best fit phase center of the hyperboloidal sub-reflectarray by calculating the far field phase pattern referenced to many points starting from the geometric virtual focal point of the equivalent hyperboloidal sub-reflectarray.

Figure 4.35 shows the far field phase patterns of a 2D hyperboloidal sub-reflectarray calculated using the 2D array analysis code with the three reference points, one located at the geometric virtual focal point F_V=61mm and the other two located at $F_V \pm (1/4)\lambda$. The eccentricity is e=1.5 and feed-horn#4 is located at F_R=320mm in all cases. For more certainty in determining the best fit phase center of the above mentioned hyperboloidal sub-reflectarray, same phase patterns were generated using the 2D MoM code as shown

in Figure 4.36. It is evident from both Figures 4.35 and 4.36 that the virtual focal point located at F_V=64mm represents the best fit phase center since the calculated phase pattern referenced to this phase center has the best flatness. Again the two sets of phase patterns have something in common. A shift of the reference phase point of $\lambda/4$ backwards (to F_V=66.5mm) caused the phase pattern to be concave down, whereas a $\lambda/4$ shift forwards (to F_V=61.5mm) gave a concave up phase pattern. This is just the opposite of what we saw in Section 4.7.2 for the ellipsoidal-type sub-reflectarray. This makes sense since the eccentricity value in the two cases causes two different concavity orientations of the scattarer.

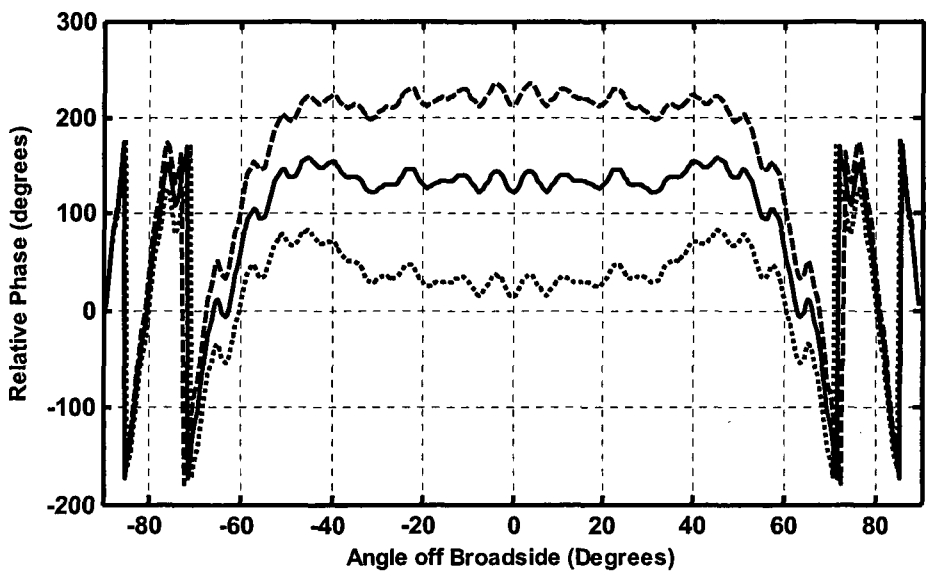

Figure 4.35- Computed E-plane far-zone phase patterns of the hyperboloidal sub-reflectarray calculated using the 2D array analysis code with the patterns calculation referenced to three points located quarter wavelength apart; F_v=66.5(--------), F_v = 64mm (——) and F_v=61.5 (.....).

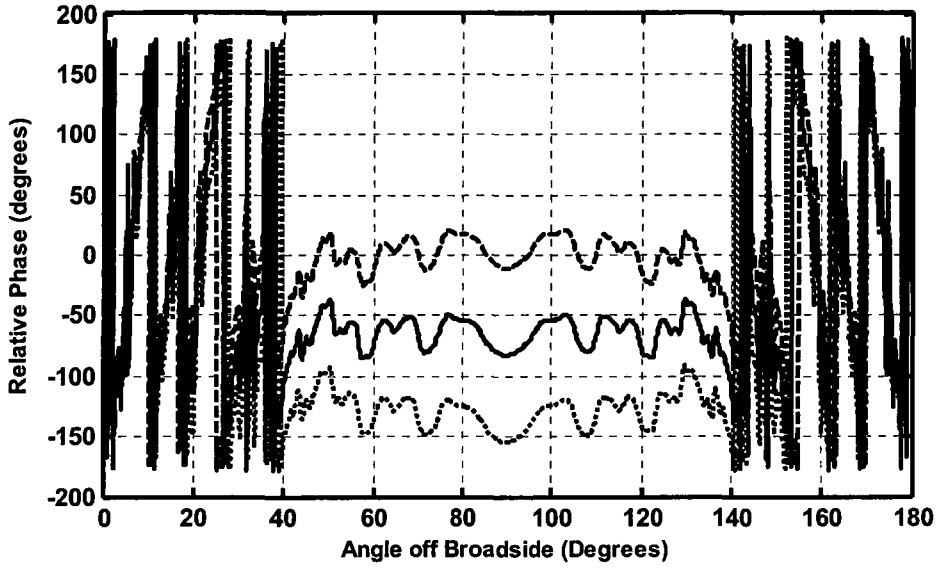

Figure 4.36- Computed E-plane far-zone phase patterns of the hyperboloidal sub-reflectarray calculated using the 2D MoM code with the patterns calculation referenced to three points located quarter wavelength apart; F_v =66.5(-------), F_v = 64mm (——) and F_v =61.5 (.....).

4.8 Power Focusing Characteristics of the Ellipsoidal Sub-reflectarray

4.8.1 Primarily Remarks

In addition to the usage of the ellipsoidal reflector as a subreflector in the Gregorian dual reflector antenna system, it was used in the past in many applications like the perimeter systems for base security and the illumination of biological specimens [11]. Recently the ellipsoidal reflector has been used for detecting objects hidden in people's bodies by benefiting from the use of its focusing characteristics in millimeter-wave imaging [12].

The near on axis field reflected by an ellipsoidal reflector has been studied in few references [11, 12, 13]. We can say generally that the literature on this subject is scant and the subject in need of further study and investigation. In this section we will perform a detailed study of the focusing characteristics of an ellipsoidal reflector as well as its equivalent sub-reflectarray. We will concentrate on the displacement of the virtual focal point as a function of the source displacement and changes in frequency for both the solid

ellipsoid and its equivalent sub-reflectarray. Then we will comment on the size of the focal region.

The validity of the ellipsoidal phase design equation (3-9) has already been established in this thesis. Nevertheless we will go steps further and show how similar the field scattered from the solid ellipsoid and its equivalent sub-reflectarray is by calculating the amplitude and phase patterns of the scattered near field for both the solid ellipsoid and its equivalent subreflectarray using the 2D full wave MoM over a rectangular region shown in Figures 4.37 and 4.38. The design parameters in both cases are the same except for the size. All design parameters are mentioned under the figure captions. The phase patterns have been shown merely to provide a qualitative view of the various wavefronts.

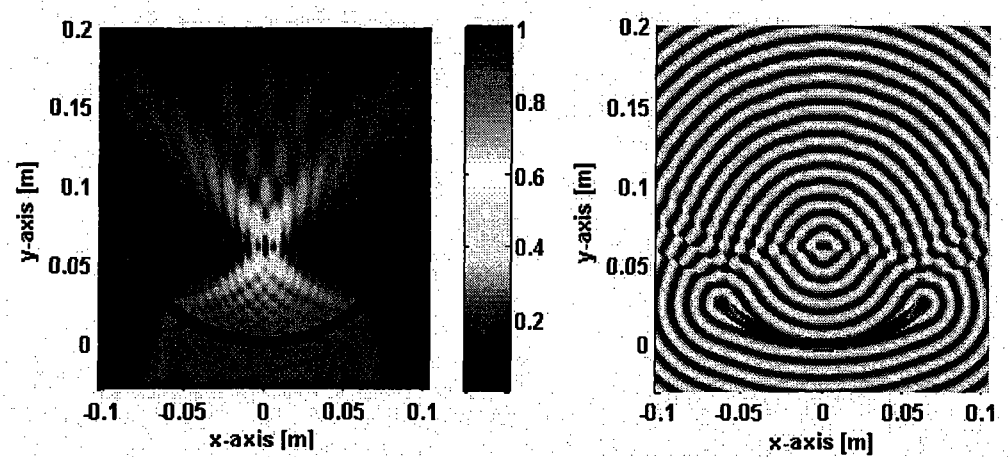

Figure 4.37- Computed E-plane near-zone amplitude and phase patterns of the ellipsoidal reflector using the 2D MoM code. A line source located at F_R =155mm from the aperture used to illuminate the reflector, e=0.4352, aperture size =128mm. The virtual focal point is found to be at F_V = 60.72mm.

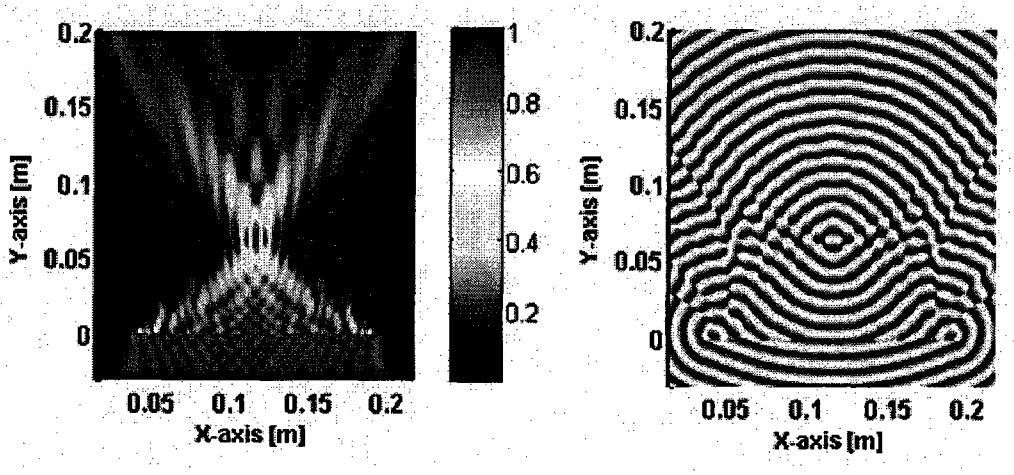

Figure 4.38- Computed E-plane near-zone amplitude and phase patterns of the ellipsoidal sub-reflectarray using the 2D MoM code. A line source located at F_R =155mm from the aperture used to illuminate the sub-reflectarray, e=0.4352, aperture size =128mm. The virtual focal point is found to be at F_V = 62.45mm.

By looking at the amplitude and phase patterns given in the figures, we immediately realize the high degree of similarity, especially if we concentrate the focusing characteristics along the axis of symmetry. This further increases our confidence about the validity of our design equation as well as about the ability to use the ellipsoidal sub-reflectarray in all applications in place of the solid ellipsoid. The field in both cases peaks at the focal spots (the virtual focal points) F_v=60.72mm and F_v=62.45mm, respectively. These are the values we obtained before when we calculated the near field along the axis of symmetry. The phase patterns in both cases show that the points from which the spherical phase fronts start emerging are the virtual focal points (best fit phase centers).

As we move away from the axis towards the edges we notice some degradation on both the phase and amplitude patterns of the sub-reflectarray scattered field in Figure 4.38. On the whole the result is very promising and the similarity is satisfactory. Improvements of the patterns shown in Figure 4.38 could possibly be obtained by using a phase versus patch width curve for actual (non-normal) angles of incidence. This can be accomplished by generating a several phase curves with a plane wave incidence at several incident angles, and then dividing the sub-reflectarray to several zones in each of which we calculate the patch widths according to a prescribed phase curve data.

4.8.2 The Displacement of the Virtual Focal Point as a Function of Feed Displacement

A valid method to check how close the ellipsoidal sub-reflectarray functions compared to that of the solid ellipsoidal subreflector is to examine the change of the virtual focal point positions, and the focusing characteristics, of both antennas when the feed position changes. We consider the same design parameters used to generate Figures 4.37 and 4.38 to calculate the rest of the results in this section, with the 2D MoM code as our simulation tool. Figures 4.39 and 4.40 show the scattered near field calculated along the axis of symmetry for the ellipsoidal subreflector and its equivalent sub-reflectarray, respectively.

For this ellipsoidal case it is clear that while F_V is "virtual" from the dual-reflector point of view it is actually a very "real" focal point.

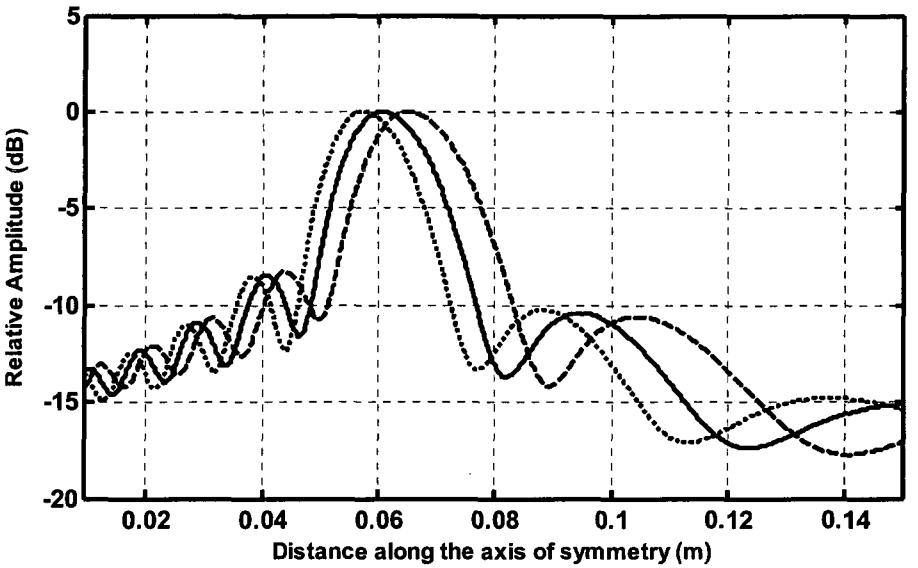

Figure 4.39- Computed scattered field of the ellipsoidal subreflector along the axis of symmetry. The subreflector is illuminated by a line source located at three positions, F_R =155mm(——) no displacement, F_R = 135mm(--------)-2 λ displacement , F_R = 175mm(.....)+2 λ displacement.

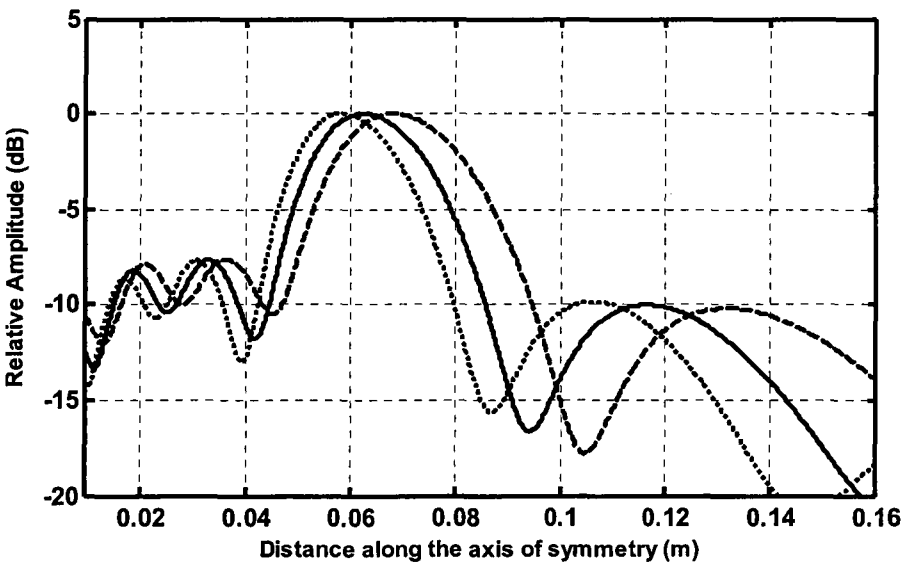

Figure 4.40- Computed scattered field of the ellipsoidal sub-reflectarray along the axis of symmetry. The sub-reflectarray is illuminated by a line source located at three positions, F_R =155mm (——) no displacement, F_R = 135mm (--------) -2 λ displacement, F_R = 175mm (.....)+2 λ displacement.

. The field is calculated for three different feed positions. The feed positions and the resulting virtual focal point shifts are given in Table 4.2.

Table 4.2- Virtual focal point position changes as a function of feed displacements

Feed		Subreflector		Sub-Reflectarray	
Position, F_R mm	**Displacement**	**F_v mm**	**Shift from F_V =60.72mm**	**F_v mm**	**Shift from F_V =62.45mm**
155	0	60.72	0	62.45	0
135	-2λ	65.22	4.5	68.25	5.8
175	$+2\lambda$	57.46	3.26	58.35	4.1

It is evident from Figures 4.39 and 4.40, as well as the quantitative data in Table 4.2 that the virtual focal points for both the ellipsoidal subreflector and the sub-reflectarray behave similarly. They move outward from the antenna as the feed is moved toward it (-2λ displacement, for F_R=135mm), whereas they move toward the antenna (subreflector or sub-reflectarray) when the feed is moved backward ($+2\lambda$ displacement, for F_R=175mm). For the solid subreflector such behavior has been reported in [11]. Thus it is clear that the virtual focal point of the sub-reflectarray has a similar response as a function of feed displacement as the virtual focal point of the subreflector. This further supports the validity of the design equations derived in Chapter 3.

The amount the virtual focal point shifts back and forth in the two cases is different as shown in Table 4.2. The interesting thing is that the ratio of the front to back shift in both cases are very close, which tells us that both the subreflector and its equivalent sub-reflectarray perform in much the same way. The ratio is 1.39 for the subreflector and 1.41 for the sub-reflectarray. To be certain about the similarity of the virtual focal point behavior as a function of feed displacement for both the subreflector and its equivalent sub-reflectarray we displaced the feed far backward and forward. Another target of doing such big shift of the feed position is to see the change in axial focusing characteristics as the two foci become close (that is F_R moves close to the geometrical F_V), and to check

the possibility of having the high field focal spot behind the point at which we locate the feed (the real focal point).

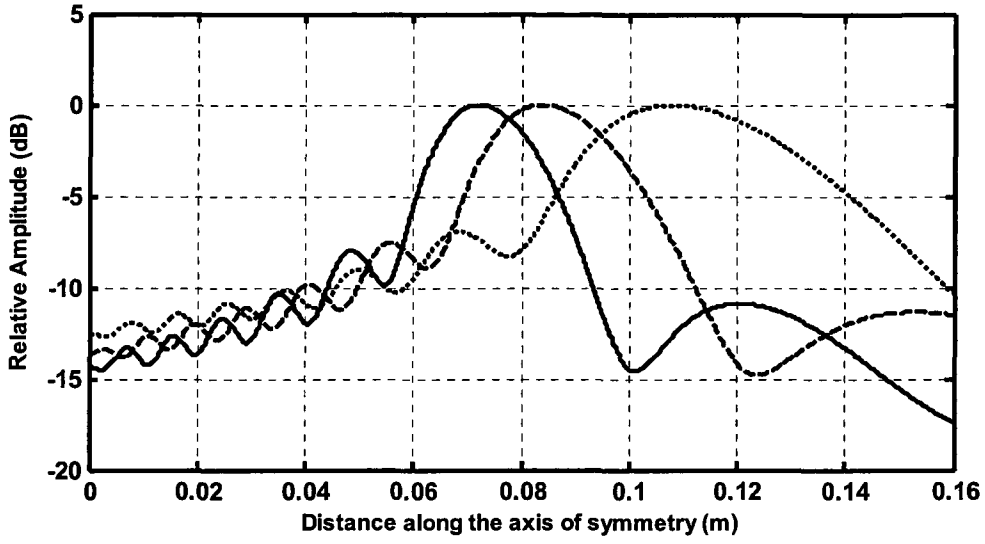

Figure 4.41- Computed scattered field of the ellipsoidal subreflector over the axis of symmetry. The subreflector is illuminated by a line source located at three positions, F_R =115mm (——) - 4 λ displacement, F_R = 95mm (--------) -6 λ displacement, F_R = 75mm (.....) -8 λ displacement.

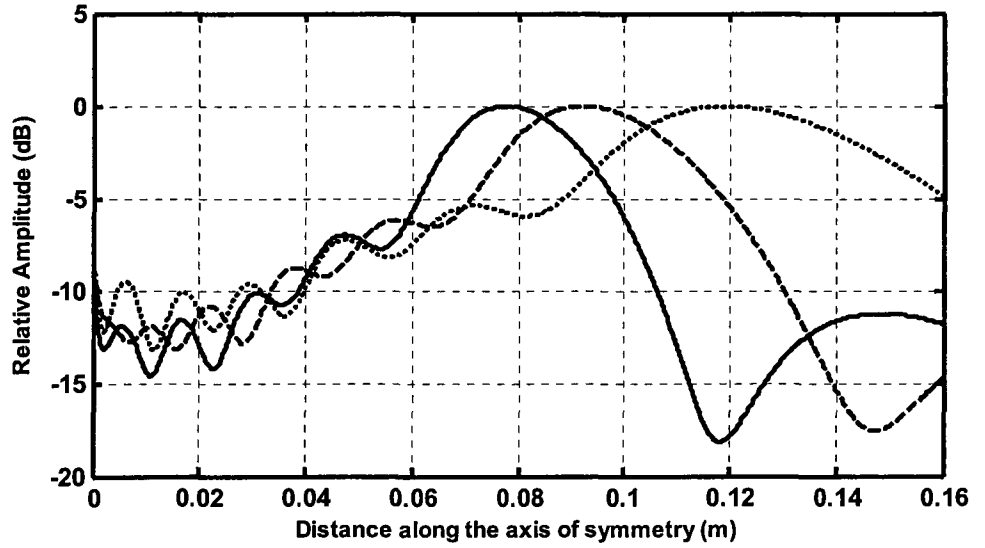

Figure 4.42- Computed scattered field of the ellipsoidal sub-reflectarray over the axis of symmetry. The sub-reflectarray is illuminated by a line source located at three positions, F_R =115mm (——) - 4 λ displacement, F_R = 95mm (--------) -6 λ displacement, F_R = 75mm (.....) -8 λ displacement.

Table 4.3 shows the feed positions and the resulting virtual focal point shifts. Figures 4.41 and 4.42 show the resulting virtual focal point shift for the subreflector and the sub-reflectarray, respectively when the feed is moved considerably toward the antenna.

Table 4.3- Virtual focal point position changes as a function of feed displacements with big shifts forward

Feed		Subreflector		Sub-Reflectarray	
Position, F_R mm	Displacement	F_v mm	Shift from F_v =60.72mm	F_v mm	Shift from F_v =62.45mm
115	-4λ	72.12	11.4	78.05	15.6
95	-6λ	83.9	20.18	92.45	30
75	-8λ	108.2	47.48	119	56.55

The resulting virtual point shifts for both the subreflector and the sub-reflectarray shown in Figures 4.41 and 4.42 respectively, as well as Table 4.3, make us more confident about the duality we have in virtual focal point behavior as a function of feed displacement and the focusing characteristics. It is clear that the virtual focal point keeps moving outward with respect to the antenna surface as the feed moves toward it. By moving the feed 8 wavelengths toward the antenna surface we reached the point where the focal spot of highest field value is situated beyond the feed position.

When we consider the movement of the virtual focal point with large backward shifts of the feed we obtained the results shown in Figures 4.43 and 4.44. Numerical values are summarized in Table 4.4. Notice that there is only a small forward shift of the virtual focal point, even for very large displacement of the feed backwards. For instance, when the feed displacement backwards changes from 12λ to 15.5λ (which is a large change), the virtual focal point changes into location by only about 0.08λ. It is expected that as we move the feed backward still more we might get a relatively stationary virtual focal point (phase center).

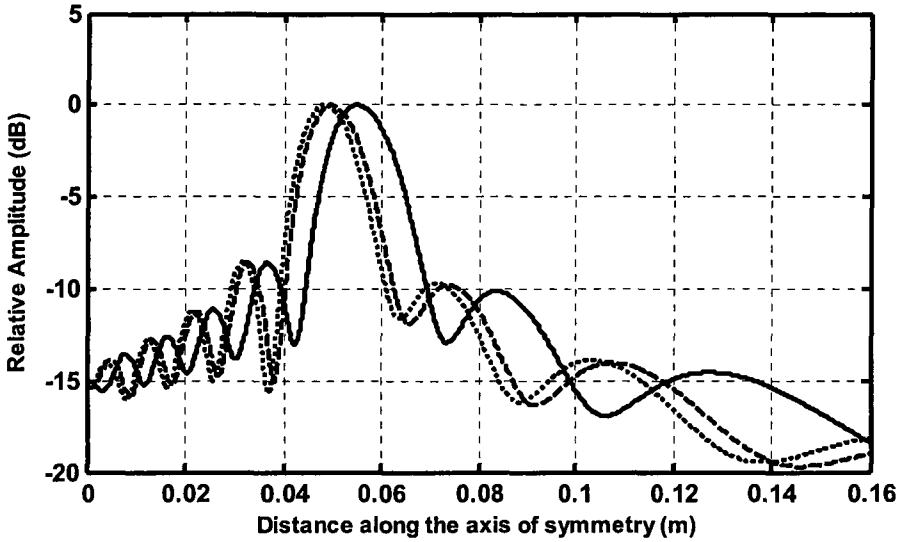

Figure 4.43- Computed scattered field of the ellipsoidal subreflector over the axis of symmetry. The subreflector is illuminated by a line source located at three positions, F_R =195mm (——) 4 λ displacement, F_R = 275mm (--------) 12 λ displacement, F_R = 310mm (.....) 15.5 λ displacement.

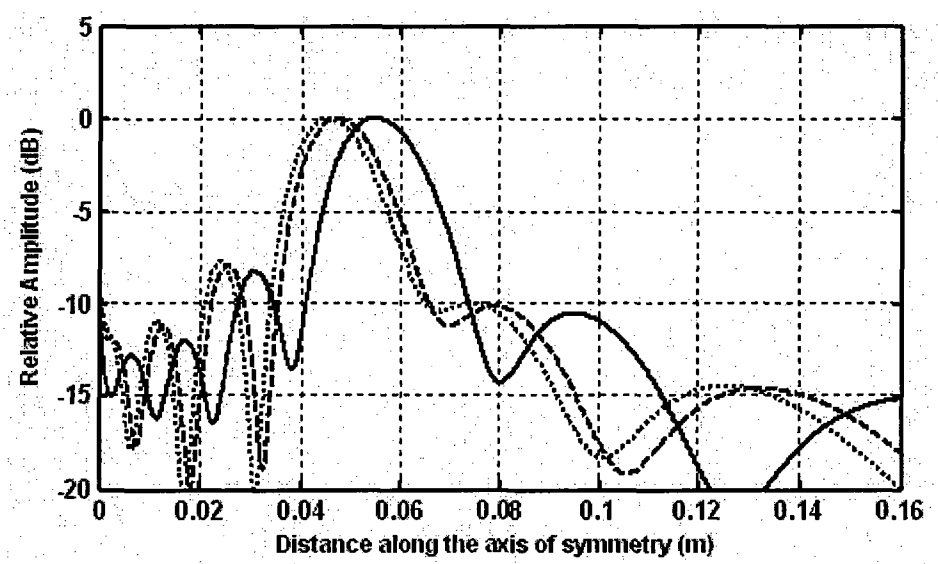

Figure 4.44- Computed scattered field of the ellipsoidal sub-reflectarray over the axis of symmetry. The sub-reflectarray is illuminated by a line source located at three positions, F_R =195mm (——) 4 λ displacement, F_R = 275mm (--------) 12 λ displacement, F_R = 310mm (.....) 15.5 λ displacement.

Table 4.4- Virtual focal point position changes as a function of feed displacements with big shifts backward.

Feed		Subreflector		Sub-Reflectarray	
Position, F_R mm	Displacement	F_v mm	Shift from F_v =60.72mm	F_v mm	Shift from F_v =62.45mm
195	4λ	54.99	5.73	54.95	7.5
235	12λ	49.6	11.12	47.25	15.2
310	15.5λ	48.2	12.52	46.46	15.99

Finally, it is likely that we have a big changes in the focusing characteristics associated with all focal point shifts for both the subreflector and its equivalent sub-reflectarray. In Figures 4.41 and 4.42, as the focal point moves to the right (away from the antenna surface) the size of the of the focal region increases, which in turn yields poor focusing characteristics. The opposite happens as the focal point moves to the left, as presented in Figures 4.43 and 4.44. However, by knowing that the focusing characteristics are affected by other factors like the eccentricity value and the size of the antenna, we expect that we can get around such a problem by select the appropriate values for the design parameters. The impact of the eccentricity upon the focusing characteristics of the ellipsoidal subreflector has been reported in [11]. It has been shown that as the eccentricity of the ellipsoidal subreflector decreases its focusing characteristics improve. The impact of antenna size on the focusing characteristics is considered in Section 4.8.3.

4.8.3 The Displacement of the Virtual Focal Point as a Function of Frequency

A. Solid Ellipsoidal Subreflector

We started by examining the impact of frequency change upon the virtual focal point for the solid ellipsoidal subreflector by changing the frequency to half, and then double, the center frequency. The 2D MoM analysis was used. When such a big change of frequency is made we nevertheless observe only an extremely small shift of the virtual focal point, as shown in Figures 4.45 and 4.46. Numerical values are summarized in Table 4.5.

Table 4.5- Virtual focal point position changes as a function of frequency change, for ellipsoidal subreflector.

Frequency GHz	Subreflector Electrical size λ	F_v mm subreflector	Shift from F_v =60.72mm
15	7.75	59.98	0.74
30	15.5	60.72	0
60	31	60.91	.18

When we halved the frequency to 15GHz, and thus halved the size of the subreflecter, the shift of the virtual focal point toward the subreflector is only 0.74mm. When we doubled the frequency to 60GHz, and thus we doubled the size of the subreflector accordingly, we got a virtual focal point shift away from the subreflector, but of only about 0.18mm. It is interesting to notice that the ratios of the two shifts (namely 0.18/.74) roughly equals the ratio of the two operation frequencies (15 /60), or alternatively the ratio of the two corresponding electrical sizes of the subreflector .

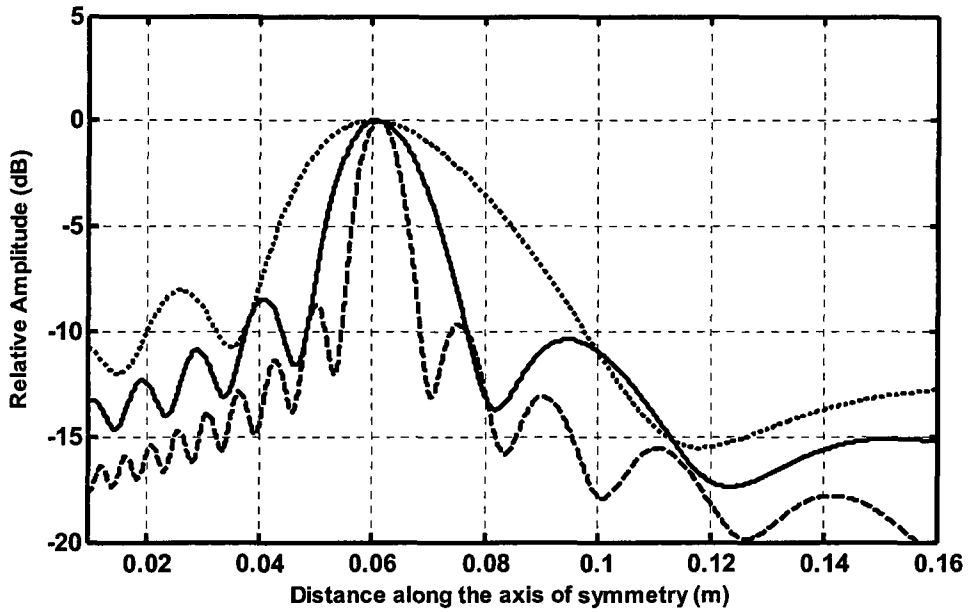

Figure 4.45- Computed scattered field of the ellipsoidal subreflector along the axis of symmetry. The subreflector is illuminated by a line source at three frequencies, f =30GHz (——), f =60GHz (- - - - - -), f =15GHz (.....)

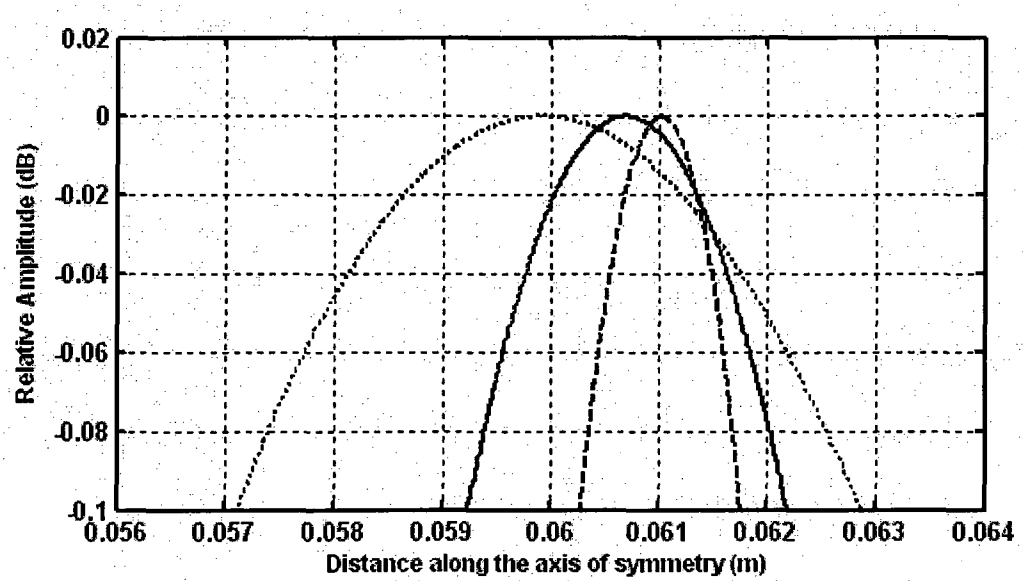

Figure 4.46- Zoomed in virtual focal point locations of Figure 4.45.

The very tiny shift of the virtual focal point is expected since it is known that all solid metallic reflectors are inherently broadband, with theoretically infinite bandwidth. In the above computations no matter what the frequency change is, the phase center of all spherical wave fronts is located at or so close to the virtual focal point.

The effect of subreflector size upon the focusing characteristics is very clear in Figure 4.45. The size of focal region is reduced considerably when the subreflector size has been doubled. The power is concentrated in a smaller spot instead of being distributed over a broader interval like that shown in the case of 15GHz operating frequency.

B. Ellipsoidal-Type Sub-Reflectarray

For the ellipsoidal sub-reflectarray, which is a narrowband antenna, we repeated same procedure we used with the subreflector in part A, but with much smaller frequency increments. All results are shown in Figures 4.47 through 4.49.

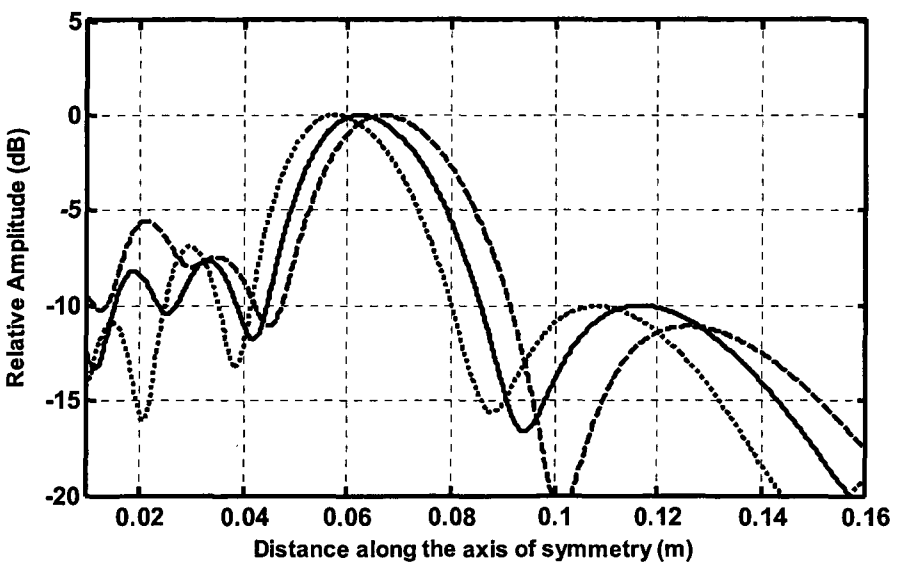

Figure 4.47- Computed scattered field of the ellipsoidal sub-reflectarray over the axis of symmetry. The sub-reflectarray is illuminated by a line source at three frequency values, f =30GHz (——), f =31GHz (--------), f =29GHz (.....)

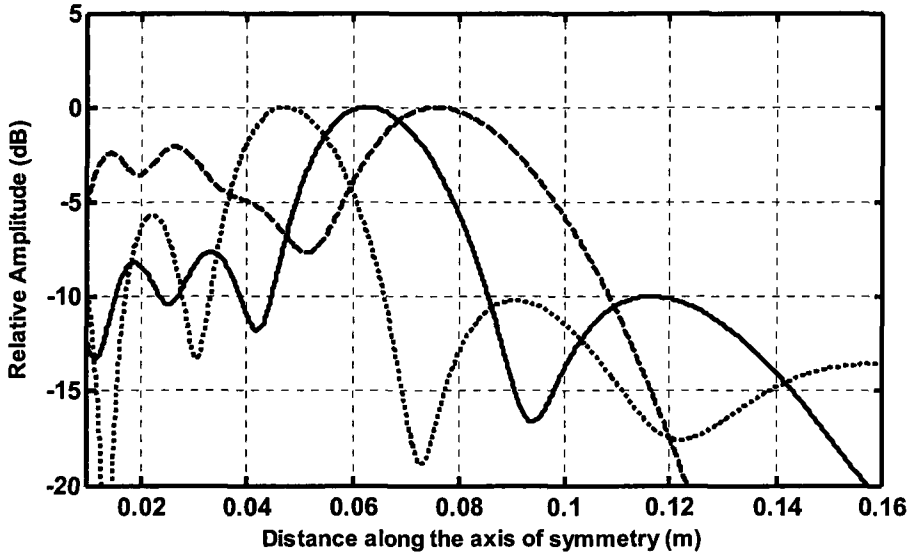

Figure 4.48- Computed scattered field of the ellipsoidal sub-reflectarray over the axis of symmetry. The sub-reflectarray is illuminated by a line source at three frequency values, f =30GHz (——), f =33GHz (--------), f =27GHz (.....)

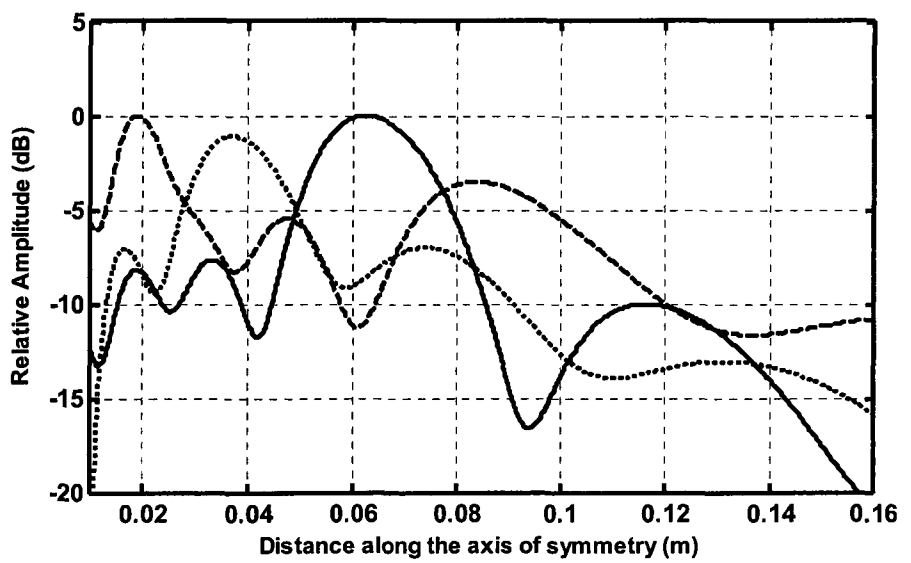

Figure 4.49- Computed scattered field of the ellipsoidal sub-reflectarray over the axis of symmetry. The sub-reflectarray is illuminated by a line source at three frequency values, f =30GHz (——), f =35GHz (--------), f =25GHz (.....).

Unlike the case of the ellipsoidal subreflector, the resulting plots of the axial field scattered from the ellipsoidal-type sub-reflectarray show the virtual focal point of the ellipsoidal sub-reflectarray changes its location considerably with any frequency change. This is expected due the narrowband nature of the reflection phase versus element width behavior. Two interesting conclusions can be drawn from Figures 4.47 through 4.49:

1- The virtual focal point of the ellipsoiodal sub-reflectarray is sensitive to any change in the operating frequency and it moves toward the sub-reflectarray aperture when the frecuency decreases and vice versa as it increases, relative to the center frequency.

2- A severe degradation of the focusing along the axis of symmetry starts after about ± 3GHz around the center frequency, which emphasizes the narrowband property of the single-layer sub-reflectarrays with simple "patch" elements. The 3GHz /30GHz percentage is comparable to the 1dB gain bandwidth of the single-layer sub-reflectarrays. The degradation starts when the deviation of the element reflection phase from the required values becomes large at the off-center frequencies.

4.9 The Displacement of the Virtual Focal Point of a Hyperboloidal Sub-Reflectarray as a Function of Frequency

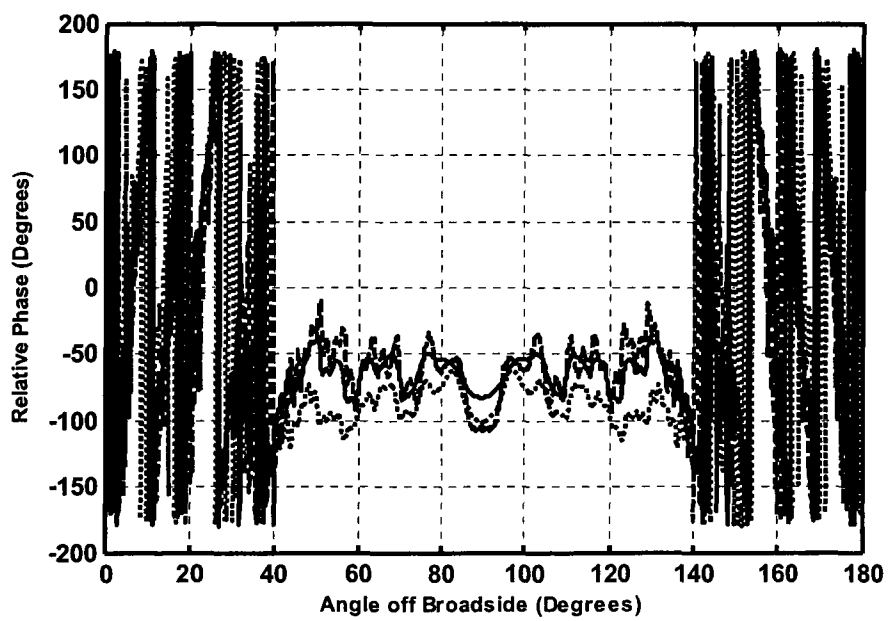

Figure 4.50- Computed E-plane far-zone phase patterns of the hyperboloidal sub-reflectarray calculated using the 2D MoM code with the patterns calculation performed at three frequency values f =30GHz (——), f =30.5GHz (--------), f =29.5GHz (.....).

Figure 4.50 shows how the far-zone phase pattern of a hyperboloidal sub-reflectarray changes with frequency. All three patterns shown are referenced to the same geometrical virtual focal point F_V= 64mm. Based on the far-zone phase pattern change with virtual focal point shifts given in Section 4.7 (the concaving up and down of the far-zone phase pattern based on the virtual focal point shift direction), we can conclude that as the frequency decreases the virtual focal point moves away from the sub-reflectarray surface, and vice versa if the frequency increases.

4.10 Concluding Remarks

In Section 4.3 we validated the simulation tools we use in this thesis both the array analysis and the 2D MoM codes. This has been done by calculating the radiation pattern of a parabolic reflectarray, which is very well known and frequently reported in the literature. Both codes showed very similar results that match the expected patterns with only minor discrepancies that have been justified.

In Section 4.4 we discussed the scattered field of ellipsoidal and hyperboloidal subreflectors. Both the amplitude and phase far field patterns were presented. This gives clear idea about the radiation characteristics of the subreflectors, which is rarely reported in the literature, as well as it introduces some important concepts we want to understand leading to the analysis sub-reflectarrays radiation characteristics. We proceeded talking about subreflectors in Section 4.5, but this time to show the similarity and correspondence between their radiation patterns and radiation patterns of their equivalent sub-reflectarrays. The calculated radiation patterns of the subreflectors and their equivalent subreflectarrays have a high degree of similarity, which proves the correctness of the derived phase design equations and show the validity of the codes we developed in this thesis.

In Section 4.6, we continued our validation of the sub-reflectarray design equations derived in Chapter 3. We validated them using the two simulation tools namely, the array analysis and the full wave MoM codes. We compared the sub-reflectarrays amplitude and phase patterns computed using the two codes. The similarity was very high and all discrepancies were justified. Moreover, we discussed the effects of feed blockage, finite

groundplane and edge taper change on the amplitude and phase radiation patterns of ellipsoidal-type and hyperboloidal-type sub-reflectarrays.

In section 4.7 we discussed the determination of ellipsoidal and hyperboloidal sub-reflectarrays virtual focal points (phase centers) locations. Two ways presented to find out the locations of sub-reflecarrays virtual focal points. One is solely used to determine ellipsoidal-type sub-reflectarray virtual focal point location, through calculating its scattered field on the axis of symmetry. The highest field point along the axis is the virtual focal point. Another way is to calculate the far field phase patterns of the sub-reflectarrays referenced to many points in the vicinity of the geometric virtual focal point. The best fit phase response with highest flatness and uniformity is the one that is referenced to the best fit phase center or the correct virtual focal point.

In Section 4.8 we studied the focusing characteristics of the ellipsoidal sub-reflectarray. This has been done by observing the behavior of the virtual focal point (the highest axial field point) as a function of feed displacement and frequency change. All cases we studied were done for both the ellipsoidal subreflector and its equivalent sub-reflectarray. By comparing the virtual focal point behavior in both cases, we concluded that if we select the design parameters properly, the ellipsoidal sub-reflectarray could replace the ellipsoidal subreflector successfully in all applications that needs high field strength to be focused at a certain point with the feed located at the other focal point.

4.11 References for Chapter 4

[1] Code GRASP9-SE, TICRA Engineering Consultants, Denmark (www.ticra.com).

[2] C.A.Balanis. Antenna Theory: Analysis and Design. Harper and Row, 1982.

[3] Y.Rahmat-Samii and P.Cramer, "Realizable feed element patterns for multibeam reflector antenna analysis", *IEEE Transactions on Antenna and Propagation*, vol.29, no.6, pp.961-963, November 1981.

[4] Y.Rahmat-Samii & S.W.Lee, "Directivity of planar array feeds for satellite reflector applications", *IEEE Transactions on Antenna and Propagation*, vol.31, no.3, pp.463-470, May 1983.

[5] W.V.T.Rusch, "Scattering from a hyperboloidal reflector in a cassegrainian feed system", *IEEE Transactions on Antenna and Propagation*, vol.11, no.4, pp.414-421, July 1963.

[6] C.Granet, "Designing classical offset Cassegrain or Gregorian dual-reflector antennas from combinations of prescribed geometric parameters", *IEEE Antenna and Propagation Magazine*, vol.44, no.3, pp.114-123, June 2002.

[7] High Frequency Structure Simulator (HFSS), Ansoft LLC, USA (www.ansoft.com).

[8] Software for the Analysis of Horns and Reflectors (SABOR), SSR-UPM Spain (http://www.gr.ssr.upm.es/sabor.htm)

[9] M.Arrebola, L. de Haro, J.A.Encinar & L.F. de la Fuente, "Contoured-beam Gregorian antenna with a reflectarray as subreflector", Proc. 2nd European Conf. Antennas Propagat. (EuCAP'2007), pp.1-6, Nov.2007.

[10] M. Arrebola, L. Haro and J.A. Encinar, "Analysis of dual-reflector antennas with a reflectarray as subreflector", *IEEE Transactions on Antenna and Propagation Magazine*, vol. 50, pp. 39-51, December 2008.

[11] Ronald L.Fante, "An analysis of the elliptical reflector", *IEEE Transactions on Antenna and Propagation*, vol.27, no.4, pp.455-459, July 1979.

[12] W. Nannan, Q. Jinghui & D. Weibo, "The analysis and simulation of focusing characterstics of ellipsoidal antenna for millimeter-wave imaging", *Microwave and Millimeter Wave Technology conference, ICMMT*, vol.4, pp.1862-1865, April 2008.

[13] K. Hirasawa, K. Fojimoto, T. Uchikura and H. Naito, "Power focusing characteristics of ellipsoidal reflector", *IEEE Transactions on Antenna and Propagation*, vol.32, no.10, pp.1033-1039, October 1984.

Chapter 5

Experimental Validation of Design Expressions for Sub-Reflectarrays

5.1 Preliminary Remarks

This chapter is dedicated solely to the experimental validation of the sub-reflectarray phase design equations. Measurements performed on examples of the ellipsoidal and hyperboloidal sub-reflectarrays will be described and discussed, showing the far field amplitude and phase patterns, in so doing validating the sub-reflectarray design equations.

In Section 5.2 the ellipsoidal phase design equation (3-9) will be validated; the measured far field amplitude and phase patterns of the ellipsoidal sub-reflectarray will be compared with simulated amplitude and phase patterns that have been calculated using the array analysis code. This will be done using two different feed amplitude taper values at the edge of the sub-reflectarray to gauge the impact of the amplitude taper upon the radiation characteristics of the ellipsoidal sub-reflectarray. We do a similar validation for the hyperboloidal phase design equation (3-3) in Section 5.3. The measured far field amplitude and phase patterns of the hyperboloidal sub-reflectarray will be compared with simulated patterns that have been calculated using the array analysis code.

5.2 Experimetal Validation of the Ellipsoidal Sub-reflectarray Design Equation

The size and layout of the ellipsoidal sub-reflectarray that has been used to validate the ellipsoidal phase design equation experimentally is shown in Figure 5.1. The lengths of all patches shown in Figure 5.1 have been determined based upon phase equation (3-9) and using the phase versus patch lengths curve given in Figure 2.6 with a fixed width for all patches w=3mm. The unit cell size is 0.5λ=5mm at a frequency of 30GHz. The dielectric substrate (Rogers 30030) thickness is 0.508mm (20mils) with a relative dielectric constant of 3. The focal length $F_{R=} f + a$ illustrated on Figure 3.5 equals 15.5λ=155mm, and is the distance between the phase center of the feed-horn and the center of the sub-reflectarray, whereas F_Y = 61mm. The subtended angle θ_s, which has been calculated using the given sub-reflectarray size and focal length, is 26.56°. The subtended angle is an important parameter in the determination of the edge taper values.

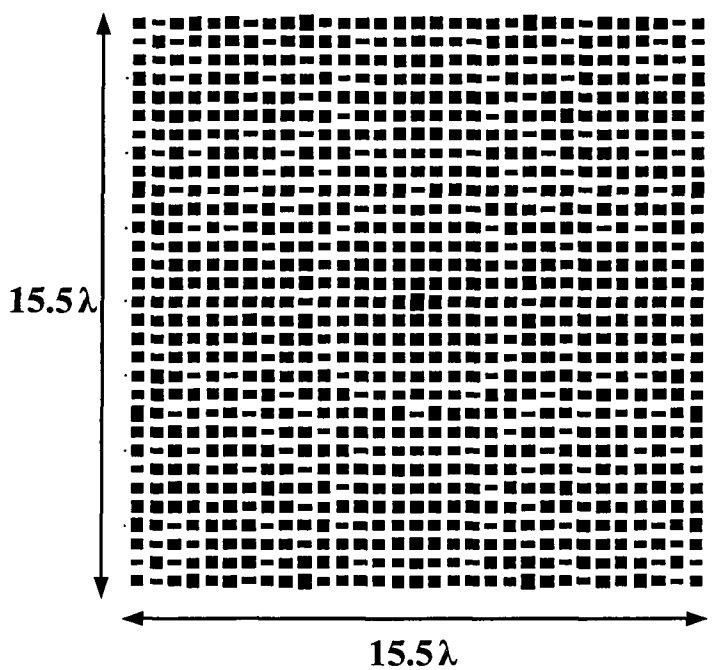

Figure.5.1- The layout and size of ellipsoidal sub-reflectarray used in measurements.

Two sets of measurements have been done to find the far field amplitude and phase patterns of the elliposoidal sub-reflectarray. The one with feed-horn#2 F_R illuminating the sub-reflecrarray, in which case the edge taper equals -3dB. The other with feed-horn#3 illuminating the ellipsoidal sub-reflectarray, with an edge taper of -9dB. In the array analysis code we modeled the feed-horn#2 and feed-horn#3 using a $\cos\theta^q$ function with a q value such that these closely match the edge taper values of the actual horn at the subtended angle $\theta_s = 26.56^\circ$. A picture of the experimental set up is shown in Figure 5.2. The dimensions of the above-mentioned feed-horns were provided in Table 4.1.

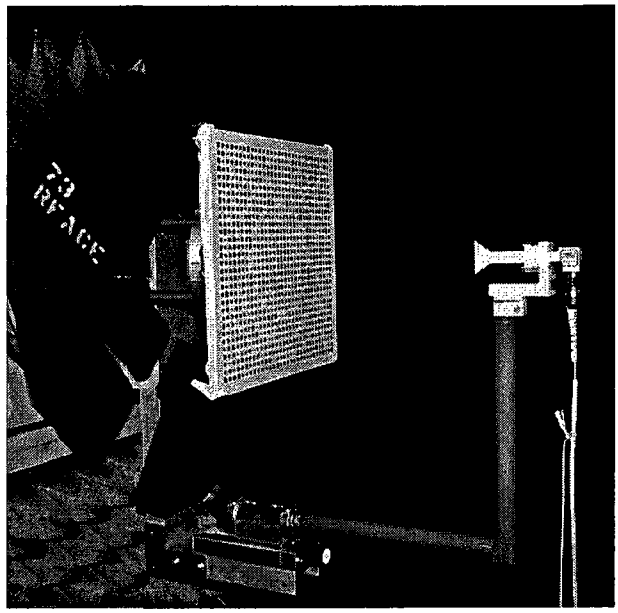

Figure.5.2- Picture of the experimental set-up used to measure the far-zone amplitude and phase patterns.

First we consider the case when feed-horn#2 illuminates the sub-reflectarray. The measured and computed far field amplitude and phase patterns in this case are shown in Figures 5.3 and 5.4, respectively. In each figure we have the measured pattern and its simulated equivalent using the array analysis technique. The phase patterns are shown referenced to the geometrical virtual focal point $F_V = 61\,\text{mm}$.

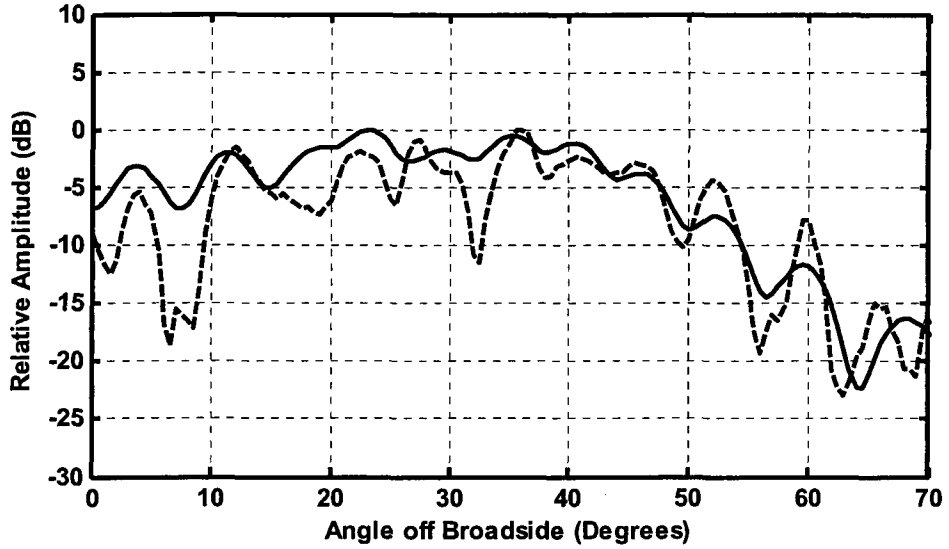

Figure.5.3- Measured (------) and computed (——) H-plane far-zone amplitude pattern of an ellipsoidal-type sub-reflectarray at 30 GHz with feed-horn#2 illuminating the sub-reflectarray. The edge taper is -3dB.

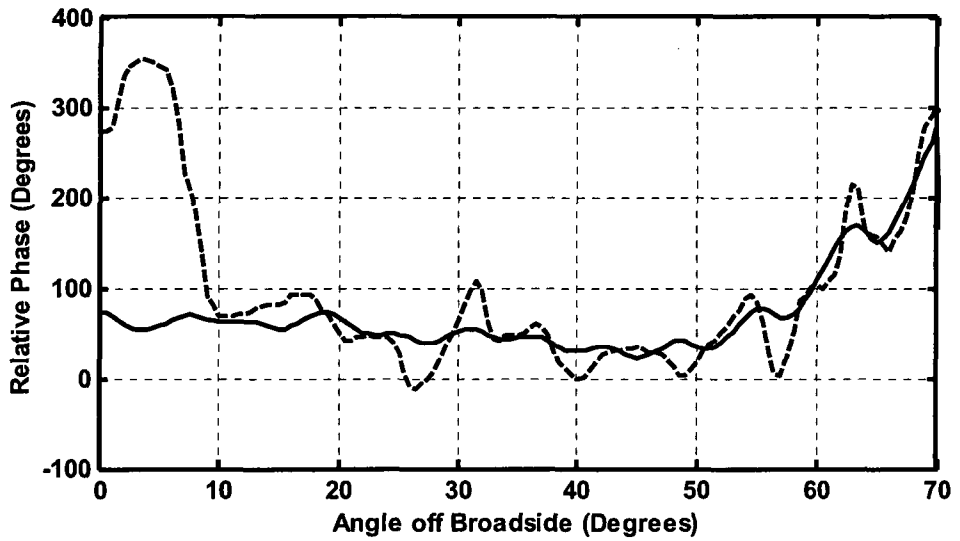

Figure.5.4- Measured (------) and computed (——) H-plane far-zone phase pattern of an ellipsoidal-type sub-reflectarray at 30 GHz with feed-horn#2 illuminating the sub-reflectarray. The edge taper is -3dB.

Since it is not possible to directly measure only the scattered fields of the sub-reflectarray, the blockage effects of the feed-horn will always be present in the measurement. So the measured results in the latter figures include such effects while the computed ones do not. The largest discrepancies are over the angular region 0° to 10° where the influence of the feed and the feed/sub-reflectarray support structure blockage is at its greatest. Differences between measured and computed results outside of this region are due to the fact that the array analysis does not include the effects of the finite ground plane or the edge diffraction effect on the patterns of the individual patch elements. The measured results used a pyramidal horn feed that provided a feed pattern edge taper of only -3dB. This is a larger edge illumination than would normally be used [1, 2], and so in practice the edge effects would be less severe. Nevertheless, the comparison between measured and computed results shows good agreement and it is on a par with that obtained for solid subreflectors [3] and paraboloidal-type reflectarrays with shaped beams [4].

It is evident from Figure 5.4 that the measured phase pattern deviates from the computed one by up to 50° at many points within the region of greatest importance. This is mainly caused by the large edge illumination that has been used in this case since the feed pattern taper is only -3dB. Thus to see the big impact of the feed edge taper upon the radiation characteristics of the ellipsoidal sub-reflectarray, we next considered the case where feed-horn#3 illuminates the sub-reflector. Figures 5.5 and 5.6 show the measured and computed far field amplitude and phase patterns of the ellipsoidal sub-reflectarray with feed-horn#3 illuminating the sub-reflectarray, for which the edge taper equals 9dB. Both figures show a much better agreement between the measured and computed patterns compared to the previous case (-3dB edge taper). This is due to the fact that the lower edge taper (-9dB) decreases the ground plane edge diffraction effects. The peak-to-peak phase variation within the region of greatest importance is a bout 60°, which is an improvement over that in Figure 5.4. The ever lower edge taper as is used with sub-reflectarrays in [1, 2] would give much better results.

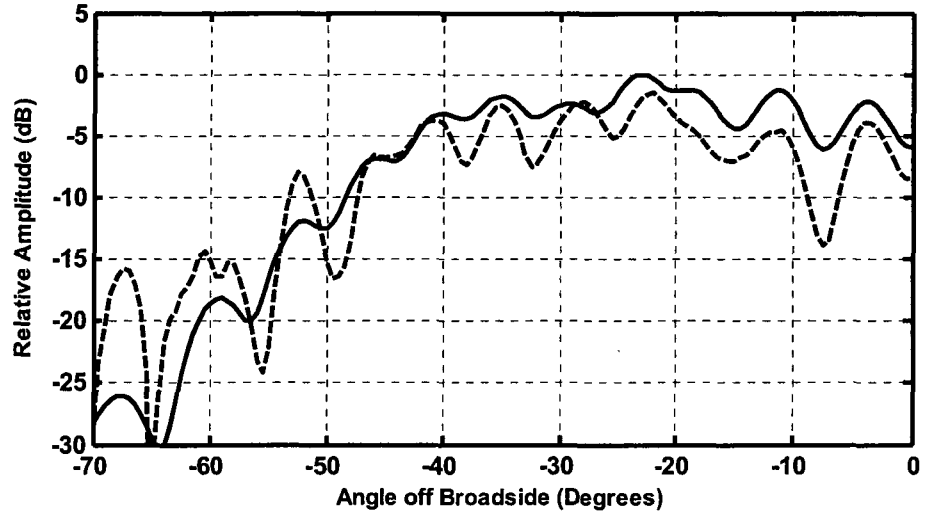

Figure.5.5- Measured (------) and computed (——) H-plane far-zone amplitude pattern of an ellipsoidal-type sub-reflectarray at 30 GHz with feed-horn#3 illuminating the sub-reflectarray. The edge taper is -9dB.

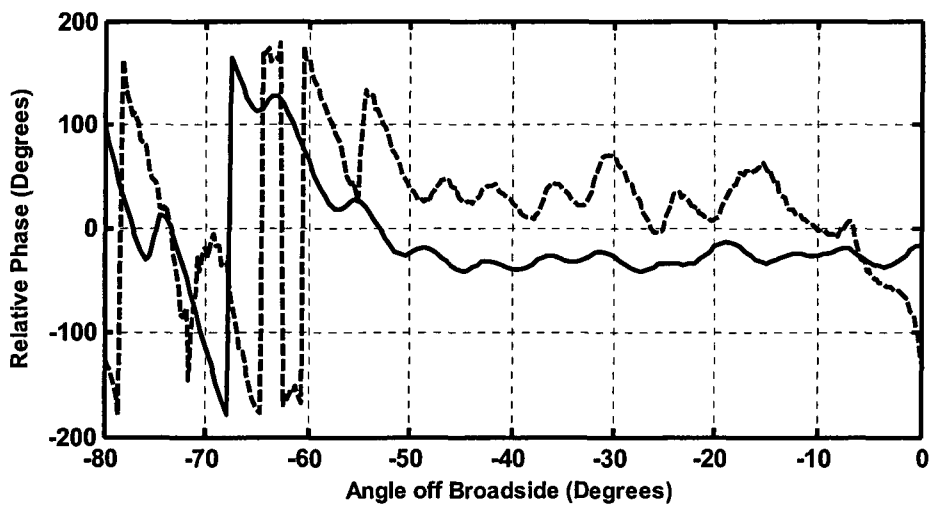

Figure.5.6- Measured (------) and computed (——) H-plane far-zone phase pattern of an ellipsoidal-type sub-reflectarray at 30 GHz with feed-horn#3 illuminating the sub-reflectarray. The edge taper is -9dB.

Note that the phase patterns shown in Figure 5.6 are referenced to the calculated virtual focal point $F_V = 63.5\text{mm}$ and not to the geometrical one $F_V = 61\text{mm}$. This has been done based upon our trials in Section 4.7 to get the best fit phase pattern (highest phase flatness and uniformity) which correspond to the best fit phase center. Figure 5.7 shows the measured far field phase pattern of the ellipsoidal sub-reflectarray with feed-horn#3 illuminating it (edge taper 9dB) referenced to three points $F_V = 63.5\text{mm}$ and $F_V = 63.5\text{mm} \pm 0.25\lambda$.

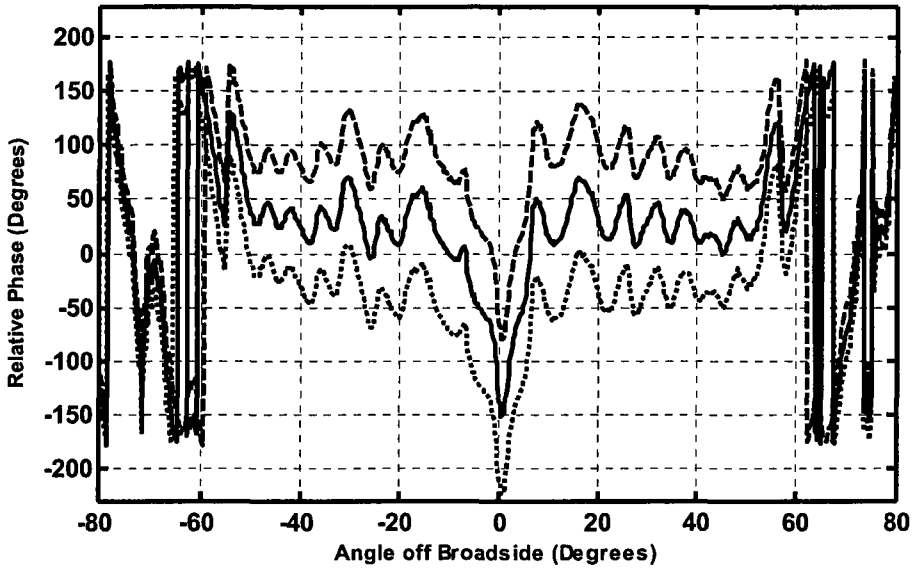

Figure 5.7- Measured H-plane far-zone phase patterns of the ellipsoidal sub-reflectarray far field phase values measured referenced to three points located quarter wavelength apart; F_V =61(--------), F_V = 63.5mm (——) and F_V =66 (.....).

Notice that in Figures 5.3 through 5.6 we presente donly one half of the associated patterns. The reason behind that is the unavoidable asymmetries we had in the measurements set up, which sometimes resulted in asymmetric patterns. Figure 5.8 and 5.9 represent the complete version of Figures 5.5 and 5.6 with an evident asymmetry around the broadside in both figures. As a result of the above analysis of the measured versus computed patterns we can say that we completed the validation of the ellipsoidal phase design equation by appealing to experiment.

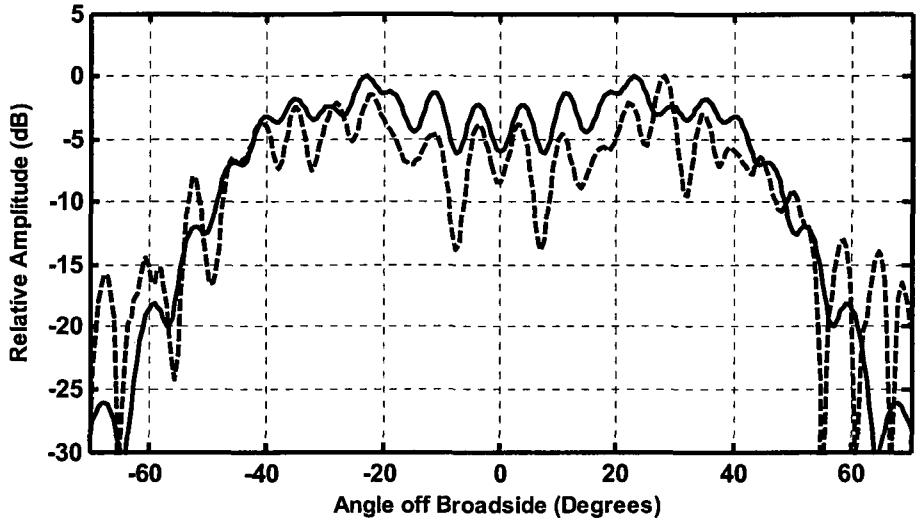

Figure.5.8- Complete measured amplitude pattern, showing the asymmetry (------), and computed (——) H-plane far-zone amplitude pattern of an ellipsoidal-type sub-reflectarray at 30 GHz with feed-horn#3 illuminating the sub-reflectarray. The edge taper is -9dB.

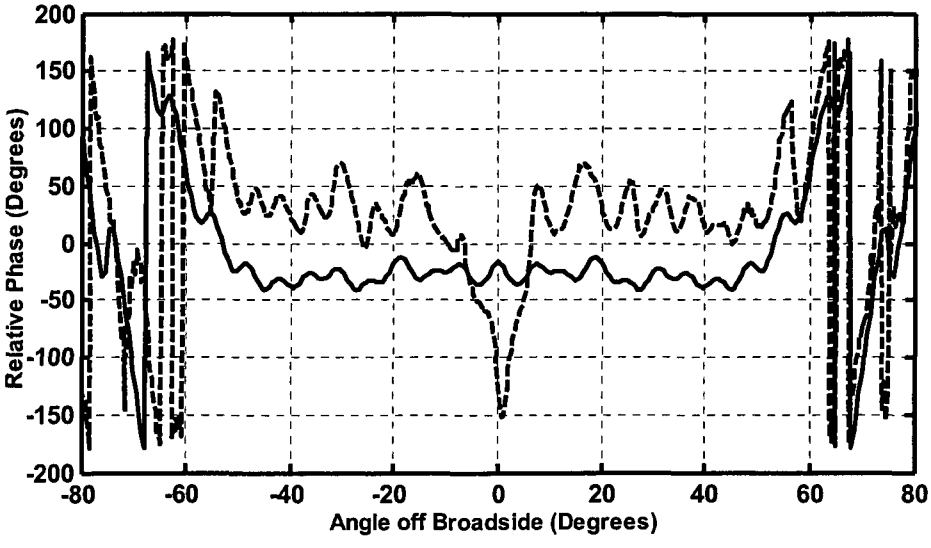

Figure.5.9- Complete measured phase pattern, showing the asymmetry (------), and computed (——) H-plane far-zone phase pattern of an ellipsoidal- type sub-reflectarray at 30 GHz with feed-horn#3 illuminating the sub-reflectarray. The edge taper is -9dB.

5.3 Experimetal Validation of the Hyperboloidal Sub-Reflectarray Design Equation

The size and layout of the hyperboloidal sub-reflectarray that has been used to validate the hyperboloidal phase design equation experimentally are shown in Figure 5.10. The lengths of all patches shown in Figure 5.10 have been determined based upon phase equation (3-3) and using the phase versus patch length curve given in Figure 2.6 with a fixed width for all patches of w=3mm. The unit cell size is 0.5λ=5mm at a frequency of 30GHz. The dielectric substrate (Rogers 30030) thickness is 0.508mm (20mils) with a relative dielectric constant equal to 3. The focal length F_R in Figure 3.4, is $F_R = 32\lambda$=320mm, and F_V = 64mm. The subtended angle θ_s using the given sub-reflectarray size is 13.5°, the subtended angle is an important parameter in determination of the edge taper values

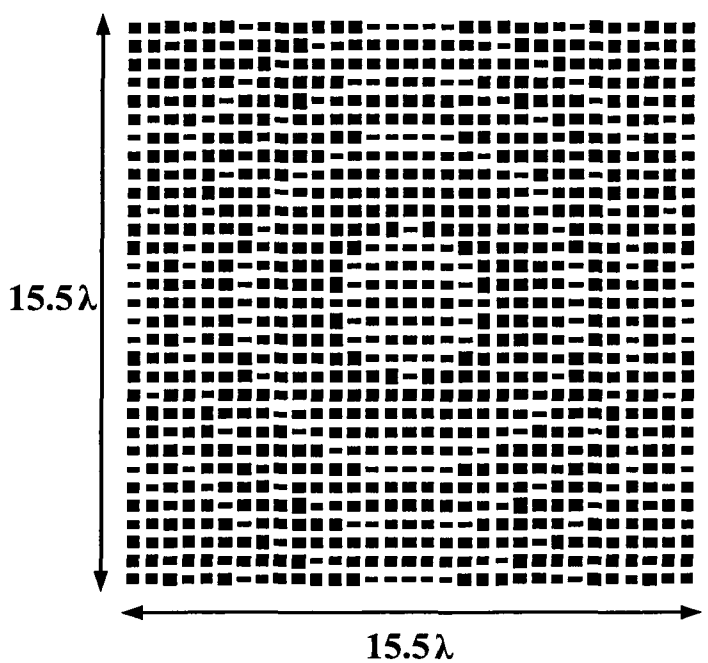

Figure.5.10- The layout and size of hyperboloidal sub-reflectarray used in measurements.

Again we used two feed-horns in measuring the far field amplitude and phase patterns of the hyperboloidal sub-reflectarray. Feed-horn#3 gives an edge taper of -2.5dB at $\theta_s =$ 13.5° and feed-horn#4 gives a -7.5dB edge taper. In the array analysis code we again modeled the feed-horn patterns using the $\cos\theta^q$ function, with q selected to give the correct edge taper values at $\theta_s = 13.5^\circ$. We first consider the case when feed-horn#3 illuminates the hyperboloidal sub-reflectarray. The measured and computed far field amplitude and phase patterns for this case are shown in Figures 5.11 and 5.12, respectively. In each figure we have the measured pattern and its simulated equivalent using the array analysis technique. The phase patterns are shown referenced to the geometrical virtual focal point $F_V = 64\,\text{mm}$.

The high edge taper value of -2.5 dB caused considerable discrepancies between the computed and the measured patterns, for both amplitude and phase. Experience with ellipsoidal sub-reflectarray in Section 5.2 showed us that this is to be expected, since the high edge illumination increases the peak to peak deviations in the phase pattern and deepens the ripples of the amplitude pattern. Recall that the computed patterns do not include feed blockage or finite ground plane effects. The blockage effect appears as usual at small angles, but for hyperboloidal sub-reflectarray whose phase center lies far enough behind it (due to the long focal length F_V) we expect lower blockage effects than what we experienced with the ellipsoidal sub-reflectarray.

To reduce the edge illumination we used feed-horn#4 to illuminate the hyperboloidal sub-reflectarray. There is a significant improvement has been achieved in the measured amplitude and phase patterns. Figures 5.13 and 5.14 show very good agreement between measured and computed patterns with good phase uniformity. The amplitude patterns almost have same angular range and same envelope. It is evident that an even lower edge taper would provide even better patterns. The full patterns of Figures 5.13 and 5.14 (which exhibit the asymmetries with the measurement) are shown in Figures 5.15 and 5.16.

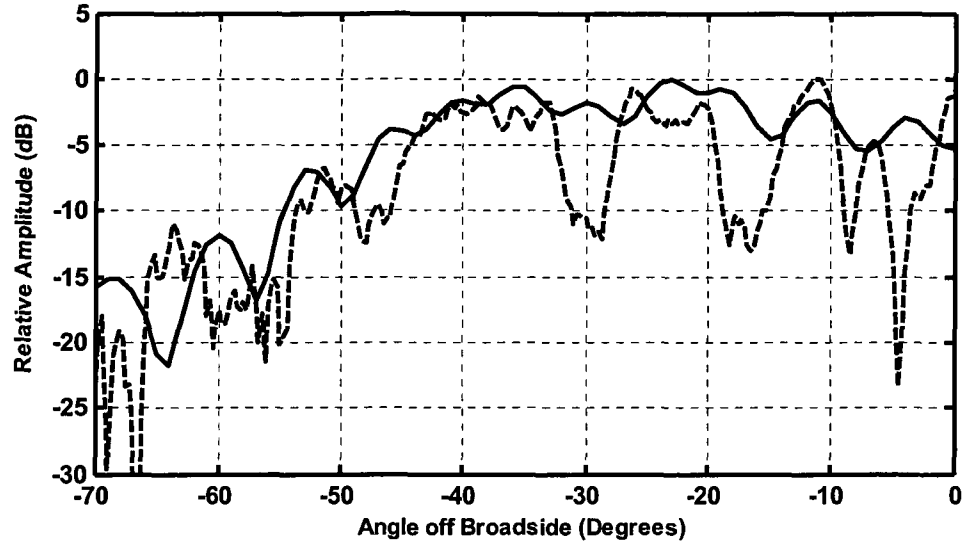

Figure.5.11- Measured (------) and computed (——) H-plane far-zone amplitude pattern of a hyperboloidal-type sub-reflectarray at 30 GHz with feed-horn#3 illuminating the sub-reflectarray. The edge taper is -2.5dB.

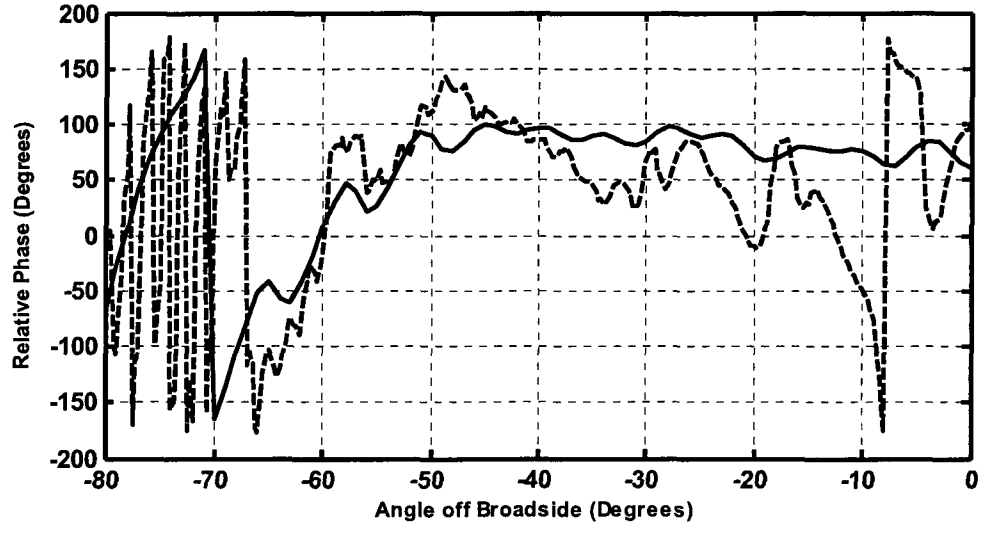

Figure.5.12- Measured (------) and computed (——) H-plane far-zone phase pattern of a hyperboloidal-type sub-reflectarray at 30 GHz with feed-horn#3 illuminating the sub-reflectarray. The edge taper is -2.5dB.

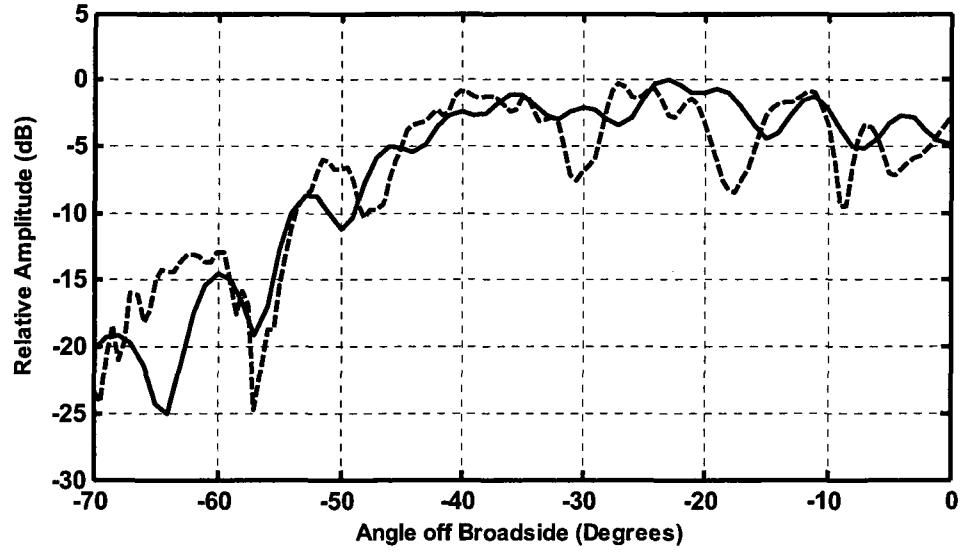

Figure.5.13- Measured (------) and computed (——) H-plane far-zone amplitude pattern of a hyperboloidal-type sub-reflectarray at 30 GHz with feed-horn#4 illuminating the sub-reflectarray. The edge taper is -7.5dB.

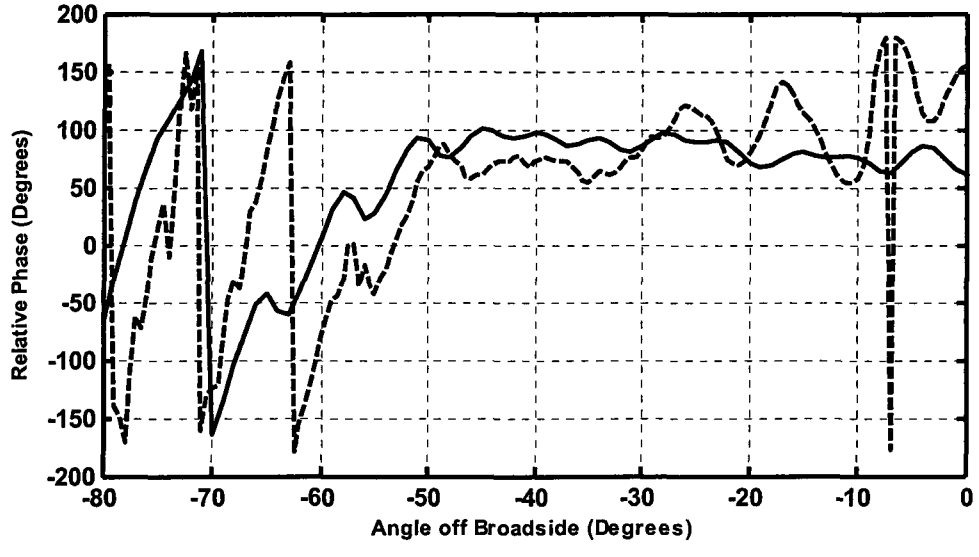

Figure.5.14- Measured (------) and computed (——) H-plane far-zone phase pattern of a hyperboloidal- type sub-reflectarray at 30 GHz with feed-horn#4 illuminating the sub-reflectarray. The edge taper is -7.5dB.

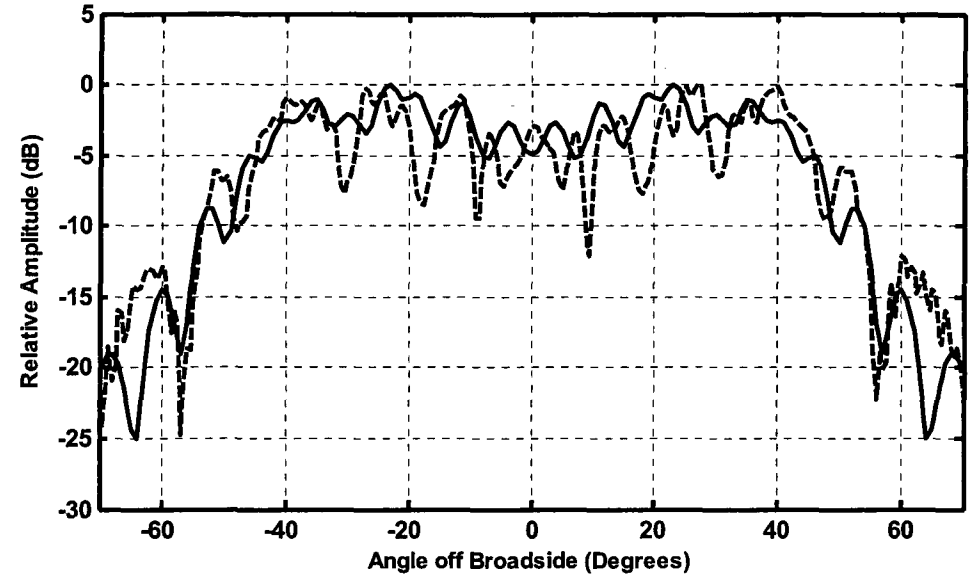

Figure.5.15- Complete measured amplitude pattern, showing the asymmetry (------), and computed (——) H-plane far-zone amplitude pattern of a hyperboloidal-type sub-reflectarray at 30 GHz with feed-horn#4 illuminating the sub-reflectarray. The edge taper is -7.5dB.

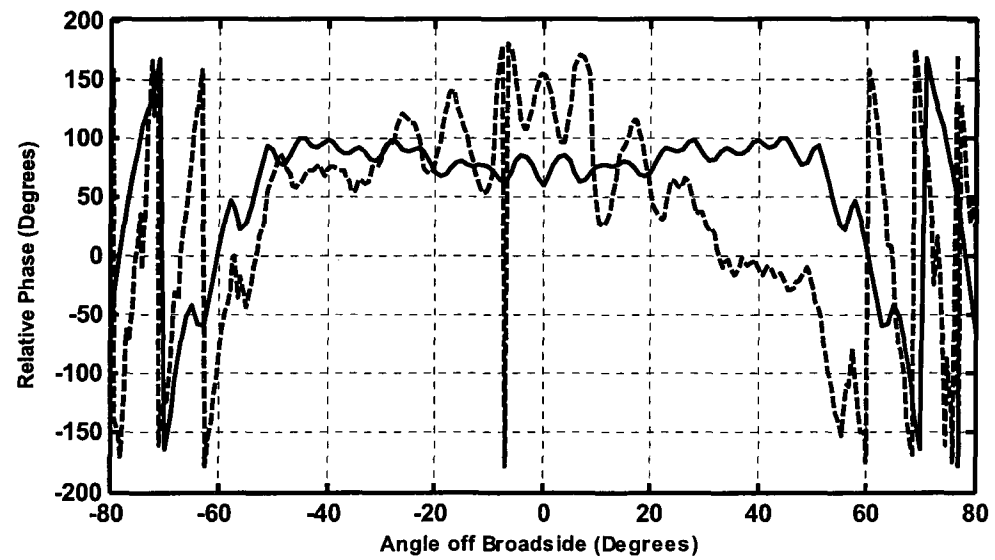

Figure.5.16- Complete measured phase pattern, showing the asymmetry (------), and computed (——) H-plane far-zone amplitude pattern of a hyperboloidal-type sub-reflectarray at 30 GHz with feed-horn#4 illuminating the sub-reflectarray. The edge taper is -7.5dB.

5.4 Concluding Remarks

In Section 5.2 the ellipsoidal sub-reflectarray phase design equation has been validated experimentally. The measured and computed patterns were very similar especially for the case when lower feed edge taper was used. The edge taper effect upon the amplitude and phase patterns was evident. Both the amplitude and phase patterns were improve for larger feed pattern taper as it reducing the ground plane edge diffraction effects. In Section 5.3 the hyperboloidal sub-reflectarray phase design equation was validated experimentally.

5.5 References for Chapter 5

[1] M. Arrebola, L. Haro and J.A. Encinar, "Analysis of dual-reflector antennas with a reflectarray as subreflector", *IEEE Transactions on Antenna and Propagation Magazine*, Vol. 50, pp. 39-51, December 2008.

[2] M.Arrebola, L. de Haro, J.A. Encinar and L.F. de la Fuente, "Contoured-beam Gregorian antenna with a reflectarray as subreflector", *Proc. 2nd European Conf. Antennas Propagat. (EuCAP'2007)*, pp.1-6, Nov.2007.

[3] W.V.T.Rusch, "Scattering from a hyperboloidal reflector in a cassegrainian feed system", *IEEE Transactions on Antenna and Propagation*, vol.11, no.4, pp.414-421, July 1963.

[4] J.Huang and J.A.Encinar, *Reflectarray Antennas*, New York: J. Wiley & Sons, 2008. pp.189.

Chapter 6

General Conclusions

The contributions of this thesis can be summarized as follows:

- The basic phase design equations for sub-reflectarrays that emulate the ellipsoidal and hyperboloidal subreflecters of the axially symmetric Cassegranian and Gregorian dual reflector antenna systems, respectively, were derived. These design equations have not been reported elsewhere in the literature. They have been validated both theoretically and experimentally using several examples of sub-reflectarrays which were designed using the said equations.

- An analysis of the radiation characteristics of sub-reflectarrays has been described. This appears to be the first time such a study of the far field amplitude and phase patterns of sub-reflectarrays has been given. It includes the examination of the effect of feed amplitude taper upon the sub-reflectarray radiation characteristics.

- A novel study of sub-reflectarray phase center location determination, and the focusing characteristics of ellipsoidal sub-reflectarrays, has been presented. This study showed that the ellipsoidal sub-reflectarray can not only function as a proper replacement for solid ellipsoidal subreflectors in the Gregorian dual-reflector antenna systems, but can also successfully replace it in applications that need a high field strength at a certain point (the one focal point) when a source is located at another (the other focal point).

- In order to perform the two-dimensional full-wave analysis a complete two-dimensional TE_Z moment method integral equation formulation, consisting of a magnetic line source that illuminates a structure consisting of conducting strips, dielectric material and conducting ground plane, has been described. Based on this formulation, it was possible to model a 2D sub-reflectarray's feed-horn, the sub-reflectarray proper (taking into account the finite size of the substrate and the groundplane), as well as the interaction between the feed-horn and the sub-reflectarray. It is a rigorous method, without approximation, that accounts for many effects whose inclusion in a similarly detailed 3D full-wave analysis would not be computationally feasible, even by present day computing standards. This full-wave 2D analysis supplemented the insights on the sub-reflectarray behaviour also obtained from measurements. It also provided information that is not easily obtainable form measurements.

- An extension of the approximate analysis of sub-reflectarrays that is based on an array analysis approach has been provided. Although not new, some refinements are provided, and the details do not appear to have been given elsewhere.

There are a number of issues whose investigation in the future would be useful in the design of sub-reflectarrays antennas. Firstly, a derivation of sub-reflecarray phase design expressions for offset dual-reflector antenna systems would enable us to benefit from all features of the offset configuration, especially the diminishing of the blockage effect. It is expected that the same principles and design methodology outlined in this thesis would be applicable for the offset case.

Furthermore, it is important to study the overall dual reflector far field performance with the sub-reflectarray as the subreflector. This would need feed-horns with much higher gains compared to what we used in this thesis in order to optimize the system performance, but the increased feed taper would allow even better sub-reflectarray pattern performance.

Finally, future work could enhance the bandwidth of the sub-reflectarrays through the use of broadband elements that have recently been described in the literature.

List of Figures

List of Tables

APPENDIX A

Coordinate Systems

The surface of the horn, dielectric and strips can be approximated by straight line segments. The j^{th} segment connects points $t_1(j)$ and $t_2(j)$ as shown in Figure A.1.

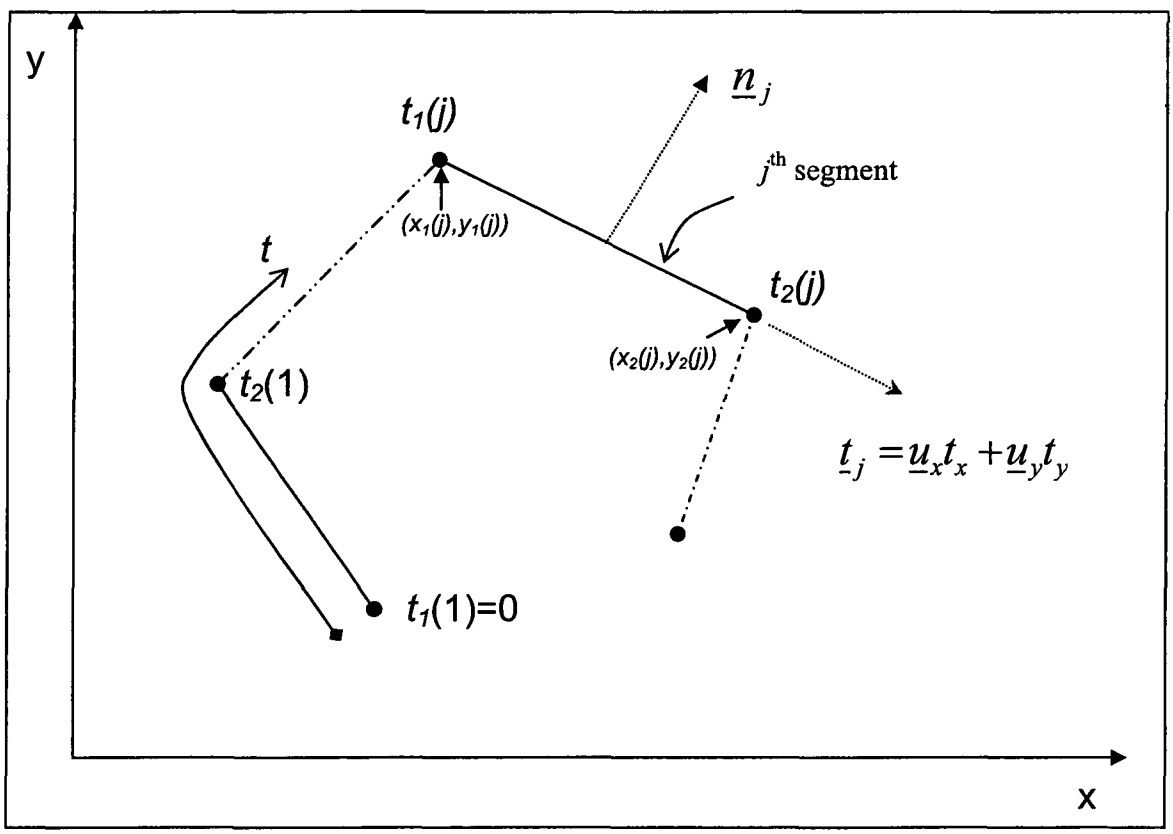

Figure A.1: Vector Coordinate System

Quantity t is the arc length along the contour starting from $t_1(1)$. The unit vector tangential to the j^{th} segment can be written as

$$\underline{t}_j = \frac{\underline{u}_x\{x_2(j)-x_1(j)\}+\underline{u}_y\{y_2(j)-y_1(j)\}}{\Delta C_j} \qquad \text{(A-1)}$$

with

$$\Delta C_j = \sqrt{[x_2(j) - x_1(j)]^2 + [y_2(j) - y_1(j)]^2} \tag{A-2}$$

Hence the normal to the j^{th} segment can be obtained from vector cross-multiplication shown in (A-3) and this result is used in deriving (3-40a) from (3-39).

$$\hat{n}_j = \hat{z} \times \underline{t}_j = \begin{vmatrix} \hat{x} & \hat{y} & \hat{z} \\ 0 & 0 & 1 \\ t_x & t_y & 0 \end{vmatrix} = -\hat{x} t_y + \hat{y} t_x \tag{A-3}$$

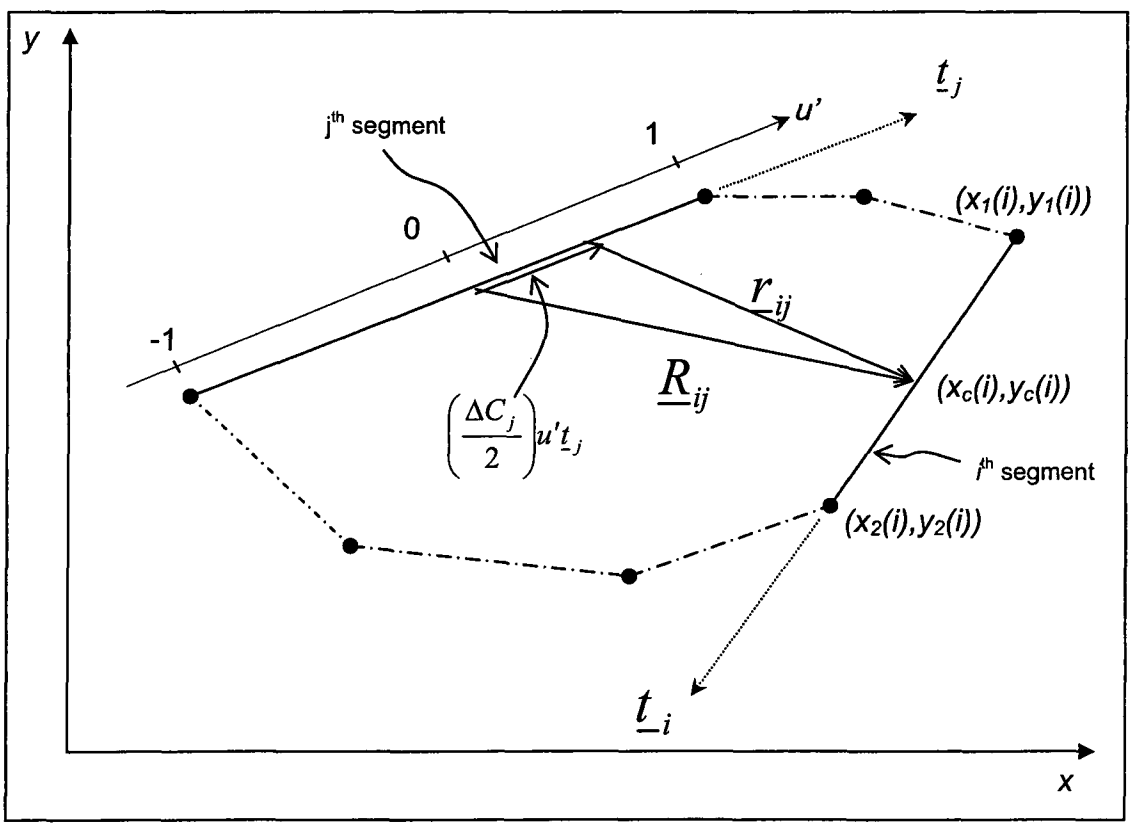

Figure A.2: Vector Coordinate System Showing Inter-Segment Vectors and Distances

From Figure A.2, the following equalities can be obtained

$$\left(\frac{\Delta C_j}{2}\right)u'\underline{t}_j + \overline{r}_{ij} = \overline{R}_{ij} \quad \Rightarrow \quad \overline{r}_{ij} = \overline{R}_{ij} - \left(\frac{\Delta C_j}{2}\right)u'\underline{t}_j \tag{A-4}$$

$$\overline{R}_{ij} = \hat{x}\left(x_c(j) - x_c(i)\right) + \hat{y}\left(y_c(j) - y_c(i)\right) \tag{A-5}$$

$$\left(\frac{\Delta C_j}{2}\right)\underline{t}_j = \frac{1}{2}\hat{x}\left\{x_2(j) - x_1(j)\right\} + \frac{1}{2}\hat{y}\left\{y_2(j) - y_1(j)\right\} \tag{A-6}$$

(A-5) and (A-6) into (A-4) results in

$$\overline{r}_{ij} = \hat{x}\left\{x_c(j) - x_c(i) - \frac{u'}{2}\left[x_2(j) - x_1(j)\right]\right\} + \hat{y}\left\{y_c(j) - y_c(i) - \frac{u'}{2}\left[y_2(j) - y_1(j)\right]\right\} \tag{A-7}$$

and thus

$$r_{ij} = \left|\overline{r}_{ij}\right| = \sqrt{a_x^2 + a_y^2} \tag{A-8a}$$

where

$$a_x = x_c(j) - x_c(i) - \frac{u'}{2}\left[x_2(j) - x_1(j)\right] \tag{A-8b}$$

$$a_y = y_c(j) - y_c(i) - \frac{u'}{2}\left[y_2(j) - y_1(j)\right] \tag{A-8c}$$

The expressions defined in this Appendix are used to evaluate the expressions (3-45a) through (3-49c).

APPENDIX B

Electric and Magnetic Fields Due to an Infinitely Long Magnetic Line Source

The electromagnetic fields of the magnetic line source located at point $\bar{\rho}_0 = (x_0, y_0)$, at any observation point $\bar{\rho} = (x, y)$, are

$$H_z(\bar{\rho}) = -\frac{\omega \varepsilon J_0}{4} H_0^{(2)}\left\{ k|\bar{\rho} - \bar{\rho}_0| \right\} \tag{B-1}$$

$$E_\phi(\bar{\rho}) = \frac{jkM_0}{4}\{\rho - \rho_0 \cos(\phi - \phi_0)\}\frac{H_1^{(2)}\left\{ k|\bar{\rho} - \bar{\rho}_0| \right\}}{|\bar{\rho} - \bar{\rho}_0|} \tag{B-2}$$

and

$$E_\rho(\bar{\rho}) = -\frac{jkM_0}{4}\rho_0 \sin(\phi - \phi_0)\frac{H_1^{(2)}\left\{ k|\bar{\rho} - \bar{\rho}_0| \right\}}{|\bar{\rho} - \bar{\rho}_0|} \tag{B-3}$$

with all other components being zero.

APPENDIX C

The Two-Dimensional Directivity

The two-dimensional directivity can be calculated in a manner similar to the three-dimensional case. The directivity at an angle ϕ is the ratio of the radiation intensity at that angle to the average radiation intensity over the interval 0 to 2π. Thus we have

$$D(\phi) = \frac{U(\phi)}{U_{avg}} \tag{C-1}$$

For this 2-D case, the radiation intensity can be related to the power density $S(\phi)$ by

$$U(\phi) = \rho S(\phi) \tag{C-2}$$

where $\bar{\rho} = x\hat{x} + y\hat{y}$. The Power density can be written in terms of the electric field as

$$S(\phi) = \frac{\eta_o}{2}\left|H_z(\rho,\phi)\right|^2 \tag{C-3}$$

The two dimensional electric field in the far-zone takes the form

$$H_z(\rho,\phi) \rightarrow \frac{e^{-jk\rho}}{\sqrt{\rho}} H_z(\phi) \tag{C-4}$$

Expressions (C-3) and (C-4) into (C-2) gives

$$U(\phi) = \frac{\eta_o}{2}\left|H_z(\phi)\right|^2 \tag{C-5}$$

Finally (C-5) into (C-1) gives

$$D(\phi) = \frac{\left|H_z(\phi)\right|^2}{\frac{1}{2\pi}\int_0^{2\pi}\left|H_z(\phi)\right|^2 d\phi} \tag{C-6}$$